

**Ministry of Higher Education and Scientific Research  
University of Baghdad  
Institute of Laser for Postgraduate Studies**



# **High Sensitivity Balloon-Like Thermometric Sensor Based on Bent Single Mode Fiber**

**A Thesis Submitted to the Institute of Laser for  
Postgraduate Studies, University of Baghdad in Partial  
Fulfillment of the Requirements for the Degree of Master of  
Science in Laser / Electronic and Communication  
Engineering**

**By**

**Dunia Ibrahim Abduljabbar Al-Janabi**

**B.Sc. Laser and optoelectronic Engineering – 2016**

**Supervisor**

**Prof. Dr. Abdul Hadi Al-Janabi**

**2020 AD**

**1442 AH**

بِسْمِ اللَّهِ الرَّحْمَنِ الرَّحِيمِ

"قَالُوا سُبْحَانَكَ لَا عِلْمَ لَنَا إِلَّا مَا عَلَّمْتَنَا إِنَّكَ أَنْتَ

الْعَلِيمُ الْحَكِيمُ" 

صدق الله العلي العظيم

سورة البقرة الآية (٣٢)

## **Certification**

I certify that this thesis was prepared under my supervision at the Institute of Laser for Postgraduate Studies, University of Baghdad, as a partial fulfillment of requirements for the degree of "Master of Science in Laser/ Electronic and Communication Engineering".

Signature:

Name: **Dr. Abdul Hadi Al-Janabi**

Title: **Professor**

Address: Institute of Laser for Postgraduate studies,  
University of Baghdad.

Date: / / 2020

(Supervisor)

In view of the available recommendation, I forward this thesis for debate by Examining Committee.

Signature:

Name: **Dr. Hanan Jaafar Taher**

Title: Head of the Scientific Committee.

Address: Institute of Laser for Postgraduate studies,  
University of Baghdad.

Date: / / 2020

## Examination Committee Certification

We certify that we have read this thesis " Efficient Humidity Sensor Based On An etched No-core Fiber Coated With CuO Nanoparticles" and as Examination Committee, we examined the student in its content and in our opinion, it is adequate with standards as a thesis for a degree of Master in science in Laser /Electronic and Communication Engineering.

**Signature:**

**Name:** Dr. Bassam Ghalib Rasheed  
**Title:** Professor.  
**Address:** Collge of engineering/ AL-Nahrain Unversity  
**Date:** / / 2020  
(Chairman)

**Signature:**

**Name:** Dr. Hanan Jaafar Taher  
**Title:** Assistant Professor.  
**Address:** Institute of Laser for  
Postgraduate Studies/  
University of Baghdad  
**Date:** / / 2020  
(Member)

**Signature:**

**Name:** Dr. Sarah Kadhim mohsin  
**Title:** Litruture.  
**Address:** Al- Turath University  
**Date:** / / 2020  
(Member)

**Signature:**

**Name:** Dr. Abdul Hadi Al-Janabi  
**Title:** Professor.  
**Address:** Institute of Laser for Postgraduate Studies,  
University of Baghdad.  
**Date:** / / 2020  
(Supervisor)

Approval by the Deanship of Institute of Laser for Postgradgate Studies, University of Baghdad.

**Signature:**

**Name:** Dr. Hussein A. Jawad  
**Title:** Dean.  
**Address:** Institute of Laser for Postgraduate Studies, University of Baghdad.  
**Date:** / / 2020

## الإهداء....

الى رمز الطيبة والصدق....الى من احمل اسمه بكل فخر....

الى من رحل من عالمنا وما زال دويُّ نصائحه يوجهني ..

أبي رحمه الله برحمته الواسعه

الى من قدمت سعادتي وراحتي على سعادتها..الى من كان دعائها سر نجاحي....

الى معنى الحب والحنان ..

امي الفاضله

الى أخواتي اللواتي يشاركنني الفرح والحزن على الدوام

الى مشرفي العزيز..الذي كان نوراً يضيء الظلمه التي كانت تقف احيانا في طريقي

الى من زرعوا التفاؤل في دربي وقدموا لي المساعدة والأفكار والمعلومات.

أساتذتي، أهلي وأصدقائي فلهم مني كل الشكر

الى كل من يحبني بصدق وإخلاص

إن إنهائي عملي لم يكن ليتم لولا دعمكم،أتمنى ان ينال رضاكم.....

ومن الله عز وجل التوفيق...

## ACKNOWLEDGEMENTS

First and foremost, I am grateful to the creator "ALLAH" for giving me the strength, enablement, knowledge and understanding required to complete this work.

I am heartily thankful to my supervisor, **Prof. Dr. Abdul Hadi Al-Janabi**, whose encouragement, invaluable guidance and kind support. His broad knowledge and clear thought inspired me; from the initial to the final level enabled me to develop and understand the project.

I would like to thank **Prof. Dr. Hussein A. Jawad**, the Dean of Institute of Laser for Postgraduate Studies. Special thanks to Instr. **Dr. Mahmoud S.Mahmoud**, the Deputy of Dean of Institute of Laser for Postgraduate Studies, I would like to thank Assist. **Prof. Dr. Mohamed K. Dhahir** , Head of the engineering and industrial application dept. for his support and also special sincere gratitude to all the staff and students of the institute of laser for postgraduate studies .

I would like to introduce a great thank to **Dr. Ansam Majid Salman**, for to Fraternal support and her continuous help and encouragement through this work. Special thanks to Assist. Prof. **Dr. Hassan Nasser Hashem**, for his great help in coating technique

My sincere thanks go to all my friends, especially my friend **Hussein, Baraa** for their help and support. Also, I wish to express my deepest love to my Family. Thanks for your endless Support for me when I feel frustrated during the study.

## ABSTRACT

Fiber Optic Sensors (FOS) have verified to be a potentially brilliant method for temperature monitoring owing to their plentiful benefits, including inviolability to electromagnetic interference, wide bandwidth, lightweight, compact size, durability, and that permits a vast numeral of sensors to function in the same structure. In this thesis, an innovative temperature sensor based on Mach-Zehnder interferometer is planned and experimentally proved. The sensing construction is shaped by bending a single mode fiber (SMF) into a balloon-like configuration. Six different fiber sections: fiber with original protective polymer coating, fiber with a stripped-off protective polymer coating, fiber with polyvinyl alcohol (PVA) coating showed the sensitivity of  $\sim -1.492 \text{ nm}/^\circ\text{C}$ , a fast response time of  $\sim 2.78 \text{ ms}$  and a good resolution of  $\sim 3 \times 10^{-4} \text{ }^\circ\text{C}$ , for the temperature range  $30 \text{ }^\circ\text{C}$ – $55^\circ\text{C}$ , and fiber based on gold nanoparticle (GNP) coating with different tuned GNP thicknesses ( $\sim 10, 20, \text{ and } 30 \text{ nm}$ ) were examined experimentally as temperature sensor. The proposed sensor coated by a  $\sim 20 \text{ nm}$  layer thickness of GNP showed the best performance with excellent sensitivity, fast rise time, and an excellent resolution of  $-2.56 \text{ nm}/^\circ\text{C}$ ,  $1.73 \text{ ms}$ , and  $1.82 \times 10^{-4} \text{ }^\circ\text{C}$ , respectively. Benefiting from its excellent advantages of simple configuration, easy fabrication, good thermo-optical properties of GNP and high mechanical strength, this high-sensitivity temperature sensor could be a competitive candidate for various temperatures monitoring processes such as human body, food industries, chemical analysis, detections of molecular analysis, and label-free biomedicine. To the best of our knowledge, this is the first time that the deposited of the GNP utilizing the magnetron sputtering technique on the SMF has been investigated in fabricating a macro-bent interferometer based temperature sensor.

## TABLE OF CONTENTS

Index	Title	Page
	Abstract	i
	List of Contents	ii
	List of Tables	v
	List of Figures	v
	List of symbols and Abbreviations	xi
<b>Chapter one</b>		
<b>Introduction and Basic Concept</b>		
1.1	General Introduction and Motivation	1
1.2	Optical fibers	3
1.3	Categorization of Optical Fibers Forms	4
1.3.1	Single-mode fiber (SMF)	5
1.3.2	Multi-mode fiber (MMF)	5
1.3.2.1	Step-index fiber (SIF)	6
1.3.2.2	Graded-index fiber (GIF)	6
1.4	Optical fiber sensors	6
1.5	Optical fiber bending loss	8
1.6	Interferometer fiber optic sensors	9
1.6.1	Fabry-Perot interferometer (FPI)	10

1.6.2	Mach-Zehnder interferometer (MZI)	11
1.6.2.1	Mach-Zehnder interferometer with core-mode mismatch	12
1.6.2.2	Mach-Zehnder interferometer with tapered fiber	13
1.6.2.3	Fiber Bragg Grating Based MZI	13
1.6.2.4	Core-Offset fiber MZI	14
1.6.2.5	Mach-Zehnder interferometer with bending fiber sections	15
1.7	Sensing Principles and Operation	16
1.8	Coating materials	17
1.8.1	Acrylate Polymer	18
1.8.2	Polyvinyl Alcohol (PVA)	19
1.8.3	Gold nanoparticle (Au-NP)	20
1.9	Coating Methods	21
1.9.1	Casting Method	22
1.9.2	Magnetron Sputtering Method	22
1.10	Temperature sensor for biomedical application	22
1.11	LITERATURE SURVEY	24
1.12	AIM OF WORK	26
<b>Chapter two Experimental Setup</b>		
2.1	Introduction	27
2.2	System Layout	28

2.2.1	Broadband source(B.B.S)	28
2.2.2	Single- Mode Fiber (Corning SMF-28)	29
2.2.3	Optical spectrum analyzer (OSA)	30
2.2.4	Temperature chamber and hot plate	31
2.3	Experimental Procedures of the Work	31
2.3.1	The balloon-like fiber structure	31
2.3.2	Study the influence of varying the bending diameter	32
2.3.3	Sample Preparation and characterization based-PVA coating	34
2.3.4	Sample Preparation, characterization and deposition of gold nanoparticles (GNP) coating	35
2.4	The Rise Time and resolution measurement	38
<b>Chapter three Results and Discussion</b>		
3.1	Introduction	40
3.2	Construction and Characterization of balloon-like SMF Sensor Probe	41
3.3	The Influence of balloon-like Fiber Based-Stripped-Off Protective Coating on the Temperature Sensitivity	44
3.4	The Influence of Polymer Coating on the Sensitivity of balloon-like Fiber Temperature Sensor	48
3.4.1	The balloon-like Fiber Sensor Based-Acrylate Polymer	48
3.4.2	The balloon-like Fiber Sensor Based-PVA-Coating	50
3.5	The Influence of the gold nanoparticle (GNP)-based fiber coating on the sensitivity of balloon-like fiber Sensor	54
3.6	The Rise Time and resolution of the temperature Sensor Based on a balloon-like fiber structure	62

3.7	Conclusion	64
3.8	Future Work	65
<b>References</b>		
References		63

### LIST OF TABALS

<b>Table</b>	<b>Title</b>	<b>Page</b>
Table (1-1)	Summary of the Published Works in OFTS	24
Table (2-1)	Optical specifications of Corning (SMF-28)	29
Table (3-1)	Sensor response of different fabricated structures	61
Table (3.2)	Rise time and resolution performance of the different fabricated sensor	64

### LIST OF FIGURES

<b>Figure</b>	<b>Title</b>	<b>Page</b>
---------------	--------------	-------------

1.1	conventional structure of optical fiber	4
1.2	total internal reflection within an optical fiber	4
1.3	various types of Optical fiber	5
1.4	the block diagram of categorization of optical fiber form	6
1.5	Categorization of optical fiber sensors: (a) Extrinsic. (b) Intrinsic	8
1.6	design of fiber optics sensors	8
1.7	Fabry-Perot interferometer categorized into (a) extrinsic (b) intrinsic	10
1.8	The diagram of MZI	12
1.9	core-mismatch MZI configuration the technique	12
1.10	A tapered fiber MZI configuration technique	13
1.11	A LPG MZI configuration technique	14
1.12	A core-offset fiber MZI configuration technique	14
2.1	structure of chapter two	27
2.2	Schematics diagram of temperature sensor based on balloon-like fiber structure	28
2.3	Photo-image of the optical spectrum analyzer (OSA)	30
2.4	Schematic of the balloon-like structure	31
2.5	photograph of (FSM-60S) fusion splicer	32

2.6	Transmission spectra of the macro-bent formation with different bending diameter (a): stripped-off the original protective polymer coating, (b) retain the original protective polymer coating, and (c) PVA-based fiber coating(d)GNP- based coatingwith10n thickness layer(e) GNP-based coatingwith20n thickness layer (f) GNP- based coatingwith30n thickness layer.	33
2.7	SEM images of (a) 200 nm, (b) 2 $\mu$ m and (c) 100 $\mu$ m scales.	35
2.8	The demonstration system of DC magnetron-sputtering.	36
2.9	SEM images at different scales (a) 100 $\mu$ m, and (b) 100 nm for (1) 10 nm, (2) 20 nm and (3) 30 nm gold thickness layer.	37
2.10	experimental setup for response time measurement.	39
3.1	structure of chapter three	41
3.2	Schematic diagram of experimental setup (a) SMF (b) balloon-like.	41
3.3	Initial Output Spectra of: (a) straight SMF, (b) stripped-off SMF, (c) SMF based acrylate polymer coating, (d) SMF based PVA coating	43

3.4	Initial Output Spectra of SMF based GNP coating with a layer thickness of (a) 10 nm, (b) 20 nm, and (c) 30 nm.	44
3.5	The transmission spectrum response for the balloon-like configuration with stripped-off the original protective polymer coating for temperature change: (a) 30-55 °C, (b) 55-30 °C, and (c) Linear fitting curves of Wavelength shifts versus temperature variation.	44
3.6	The transmission spectrum response for the balloon-like configuration with stripped-off the original protective polymer coating for temperature change: (a) 35-47 °C, (b) 47-35 °C and (c) linear fitting plots of the shifted dips versus temperature change in the function of wavelengths shift.	47
3.7	The transmission spectrum response for the balloon-like configuration with the original protective polymer coating with temperature change in the range (a) 30-55 °C, (b) 55-30 °C, and (c) Linear fitting curves of Wavelength shifts versus temperature variation	49
3.8	The transmission spectrum response of the	50

	balloon-like sensor configuration with the original protective polymer coating as the temperature is changed from (a) 35-47 °C, (b) 47-35 °C, and (c) linear fitting plots of the shifted dips against temperature change in the function of wavelengths shift.	
3.9	The transmission spectrum response of the balloon-like sensor configuration for PVA-based fiber coating as the temperature is changed from (a) 30-55 °C, (b) 55-30 °C, and (c) Linear fitting plots of the wavelength shift against temperature change.	52
3.10	The transmission spectrum response of the balloon-like sensor configuration for PVA-based fiber coating as the temperature is changed from (a) 35-47 °C, (b) 47-35 °C and (c) linear fitting plots of the shifted dips versus temperature change in the function of wavelengths shift.	53
3.11	The transmission spectrum response of the balloon-like sensor configuration with 10 nm thickness of the gold coating as the temperature is changed from (a) 30-55 °C, (b) 55-30 °C, and (c) linear fitting plots of the wavelength shift in the dips against	55

	temperature change.	
3.12	The transmission spectrum response of the balloon-like sensor configuration for 20 nm thickness of the gold coating as the temperature is changed from (a) 30-55 °C, (b) 55-30 °C, and (c) linear fitting plots of the wavelength shift in the dips against temperature change.	56
3.13	The transmission spectrum response of the balloon-like sensor configuration for 30 nm thickness of the gold coating as the temperature is changed from (a) 30-55 °C, (b) 55-30 °C, and (c) linear fitting plots of the wavelength shift in the dips against temperature change.	57
3.14	The transmission spectrum response of the balloon-like sensor configuration as the temperature is changed from (a) 35-47°C, (b) 47-35°C for 10 nm thickness of the gold coating, and (c) linear fitting plots of the wavelength shift in the dips against temperature change	58
3.15	The transmission spectrum response of the balloon-like sensor configuration as the temperature is changed from (a) 35-47°C, (b) 47-35°C for a 20 nm-thick gold coating,	59

	and (c) linear fitting plots of the wavelength of the shifted dips versus temperature.	
3.16	The transmission spectrum response of the balloon-like sensor configuration as the temperature is changed from (a) 35-47°C, (b) 47-35°C for a 30 nm-thick gold coating, and (c) linear fitting plots of the wavelength of the shifted dips versus temperature.	60
3.17	The response time measurement for the SMF with the (a) stripped-off coating and (b) polymer jacket retained.	62
3.18	The response time measurement for the polyvinyl alcohol (PVA)-based fiber coating.	63
3.19	The rise time measurement for (a) 10 nm gold coating thickness, (b) 20 nm gold coating thickness, and (c) 30 nm gold coating thickness.	63

## LIST OF SYMBOLS AND ABBREVIATIONS

FOS	Fiber optic sensors
MZI	Mach-Zehnder interferometer
Au	gold
TEC	thermal expansion coefficient
TOC	thermo-optic coefficient
<i>SMF</i>	single mode fiber
MMF	multimode fiber
SIF	Step index fiber

GIF	Graded index fiber
B.B.S	Broadband source
FPI	Fabry-Perot interferometer
FBG	fiber Bragg grating
MFDs	mode field diameters
LPG	long period grating
EMI	electromagnetic interferences
NPs	nanoparticles
GNP	gold nanoparticles
PVA	polyvinyl alcohol
OPD	optical path difference
EMR	electromagnetic mode resonance
COVID-19	coronavirus
OFTS	optical fiber temperature sensor
OSA	optical fiber temperature sensors
$I_{co}$	signal intensities of the core mode
$I_{cl}$	signal intensities of cladding mode
$\delta$	phase difference
$\Delta n_{eff}$	effective refractive index difference
$n_{co}$	effective refractive indices of the core
$n_{cl}$	effective refractive indices of the cladding
$l_{eff}$	effective bending length of the balloon-like structure
$\lambda$	wavelength of the light signal in free-space
$d$	The bending diameter
$l$	the overall length

RI	refractive index
MMI	Multi-mode interferences
SEM	scanning electron microscopy
$R^2$	linear regression coefficient

# *Chapter One*

## *Introduction and Basic Concepts*

## CHAPTER ONE

### 1.1 General introduction and motivation :

Temperature measurement and monitoring represent a key parameter in numerous potential applications in industry, structural health, food manufacturing, and so on [1–3]. Furthermore, temperature monitoring is directly related to the performance enhancement of numerous industrial and electronic processes while the operating temperature is limited to a specific scale [4]. Besides, the human body temperature, for instance, is a significant sign of health and disease like Malaria, Coronavirus, and so on [5,6]. Therefore, the quality and the performance of measurements such as a high-sensitivity, real-time response, biocompatibility, robust to weak signal, and the accuracy of temperature sensor devices without causing any damage to the host are necessary parameters to enhance safety and reliable monitoring [7,8]. Classical thermometers and other devices based on electrical or mechanical changes have been used for a long time to measure temperature. All the aforementioned devices are suffering from un-precise measurement and/or long response time [9]. Among different options to enhance the sensitivity and precise measurement is using fiber optics as an active sensing element. Through the development of human-friendly smart materials, the health monitoring systems utilizing fiber devices have attracted great attention as future technologies [10,11]. Various techniques have been developed based on Fiber optic sensors (FOS) for the detection of any chemical and physical parameters including temperature measurement [12,13]. In contrast with widely traditional sensors, occasionally these sensors need to work in harsh environments and are influenced by corrosive agents or the existence of electromagnetic interferences (EMI) [14]. To overcome these difficulties, the FOSs have significant advantages such as flexibility, relatively small size, simple structure, corrosion-resistance,

lightweight, high sensitivity, remote sensing capability of multi-parameter sensors into the same optical fiber, and are extremely resistant to electromagnetic interference [15]. In the field of optical fiber sensors, the interference phenomenon represented the fundamental principle to determine sensitivity. Much progress has been achieved in the last few decades of thermometric sensor-based-optical fiber including several sensor geometries such as Fabry-Perot interferometer [16], Michelson interferometer [17], Sagnac interferometer [18], and Mach-Zehnder interferometer (MZI) [19]. Optical fiber sensors based on MZI have enticed huge studies' attention and have been broadly utilized to monitor the health of smart biomedical and engineering systems [2,10,20,22]. Up to now, many shapes of fiber MZI structures have been established using photonic crystal fibers [23], along-period fiber gratings [24], tapered fiber-based configurations [25], microfiber based configuration [26], multicore fiber [27], and core-offset section [13]. Besides these configurations of complex technology and expensive fiber, a particular cost-effective MZI based on SMF was portrayed, such as a macro-bent structure based on SMF [28–30]. This configuration shows an excellent performance in the temperature sensing applications. The geometry of the sensing head identified as balloon-like possesses unique advantages as it offers low cost, simplicity of fabrication, and have excellent sensitivity, short response time, good resolution [31,32]. Recently, lots of attempts have been exerted to further improve the performance of temperature sensors, such as using a combination of interferometric structures (e.g. MZI) with resonance assisting material supports. Generally, pure polymer, conductive polymer, and polymer composited coating are good candidates for temperature sensor goals [33]. Also, to improve the sensing abilities, the optical fiber demand to be bounded by a greater refractive index (RI) nanomaterial with a great particular surface area and diverse active sites to sense efficiently the alteration in temperature of the environment. The sensing occurs as

the sensitive matter interacts with the evanescent wave and changes the transmitted output signal. In this consequence, the mixture of optical fibers and nanotechnologies mainly metallic nanoparticles (NPs) is a hot topic of interest in the scientific field of modern research, dealing with engineering and fabricated extremely sensitive temperature sensor structure. This is encouraged by the famous unique features of the metallic NPs such as great surface to volume ratio, optical, chemical, and electronic features that are diverse contrasted with those of bulk ones [34]. Among different metal NPs, gold nanoparticles (Au-NP) composite is promising for capacitive temperature sensor application.

The design and fabrication of the temperature sensor based on a balloon-like MZI system possess promising features with good performance. The basic operation of a fiber optic modal interferometer based on macro-bent MZI is associated with the interaction between the core mode and cladding modes. In this work, the influence of this structure has been examined in various cases under the conditions of i) stripped-off polymer coating, ii) acrylate polymer coating, iii) polyvinyl alcohol (PVA) polymer coating, iv) Au-NP coating.

## **1.2 Optical fibers:**

The optical fiber is a dielectric waveguide, flexible, transparent medium with various protective coatings as depicted in Fig. (1.1). It consists of two cylindrical rods generally made from plastic or glass with different doping. These fibers typically include a transparent core (has a diameter of about 5-100  $\mu\text{m}$ ) surrounded by a cladding of a slightly lower refractive index (most of the cladding has a diameter around 125-200  $\mu\text{m}$ ). The cladding is also covered with an additional plastic coating or buffer layer for environmental protection and mechanical support [35,36].

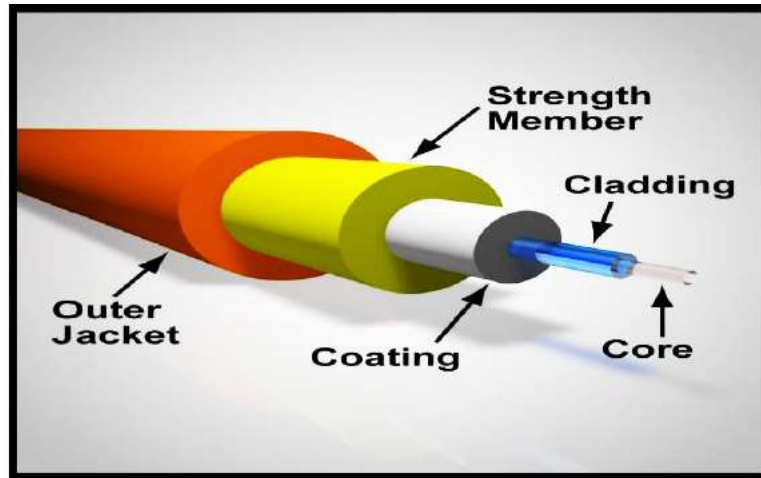


Fig. (1.1): conventional structure of optical fiber [37].

Through the features of immunity to electromagnetic field interference and low signal loss; optical fiber has been extensively utilized as a waveguide, to transmit light through the two ends of the fiber, the light propagates confined within the core by ‘total internal reflection’ phenomenon. According to Snell’s law, if the incident angle is greater than the critical angle the total internal reflection occurs [35,37], as shown in Fig. (1.2).

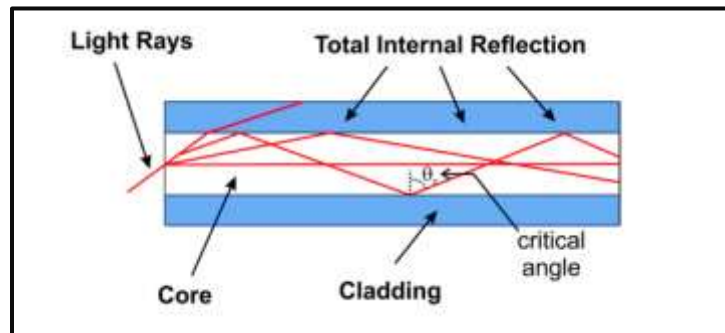


Fig. (1.2): total internal reflection within an optical fiber [37].

### 1.3 Categorization of optical fibers forms:

Optical fibers can be categorized into two groups, "SMF" and "MMF" as illustrated in Fig. (1.3). The categorization of optical fiber is obtainable in the block diagram depicted in Fig. (1.4).

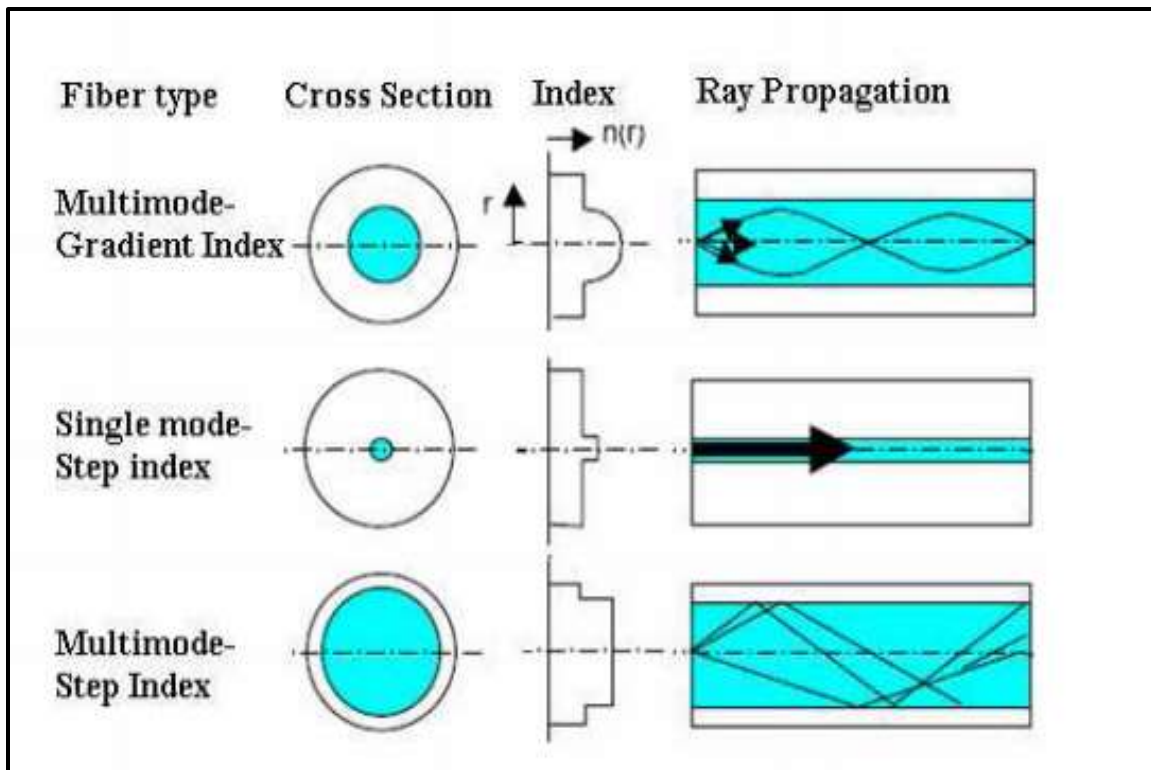


Fig. (1.3): Various types of optical fiber [37].

### 1.3.1 Single-mode fiber (SMF):

- Only support a single light ray (mode) propagates within it.
- The core radius is very small 4–6  $\mu\text{m}$ .
- Do not offer dispersion.
- Suffer from lower attenuation.
- The NA against a single-mode fiber is commonly lesser than for multimode fiber.
- Complicated to couple the light source.
- Requires Laser source. [38,39]

### 1.3. 2. Multi-mode fiber (MMF):

- Support many transverse light rays or (modes) propagates within it.
- The core radius is large 25–100 $\mu\text{m}$ .
- Offer dispersion which produces by many modes.

- Suffer from higher attenuation.
- The NA against a multi-mode fiber is commonly greater than for single-mode fiber.
- Uncomplicated to couple the light source.
- Permits the utilization of incoherent optical sources (like an LED). [38,39]

#### **1.3.2.1 Step-index fiber (SIF):**

The core refractive index stays constant and the core-cladding boundary is distinguished thru an abrupt variation in the refractive index. The propagation of light within the core of (SIF) in the zigzag pathway model [38,39].

#### **1.3.2.2 Graded-index fiber (GIF):**

There is gradual variation in the refractive index inside the core. The propagation of light within the core of (GIF) regularly diverge then converge all along with the optical fiber [38,39].

### **1.4 Optical fiber sensors:**

The technology of optical fiber sensors has extensive growth in the field of optoelectronic industries and optical fiber communication [40]. The utilization of optical fiber as detecting devices was established in many sensing applications for instance in medical sciences [41], natural configurations [42], biological group [43], analytical chemistry [44], environmental condition [45], besides additional physical parameters [46]. Since FOSs propose various magical advantages over electronic sensors for example it can simply be incorporated into structures owing to their relatively small size and cylindrical geometry, forming what is known as smart configurations. They are also purely dielectric, therefore they are suitable to utilized easily in hazardous zones, and are immune to electromagnetic interference. Further, they are robust, lightweight, and have wider

bandwidths besides to these advantages; enhancements the sensitivity and cost reduction have also significant interest in FOS within the latest decade [47].

Optical fiber sensors can be categorized into intrinsic (active) and extrinsic (passive) sensors according to the sensing location. Commonly, the extrinsic category employs an external optical device (light modulator) used for detecting, whilst intrinsic carries the sensing thru optical fiber itself [48], Fig. (1.5) shows the categorization of optical fiber sensors. FOS can be further classified as illustrated in Chart in Fig. (1.6), and as discussed below. They involve direct spectroscopy, evanescent wave, fiber grating, and interferometric sensors.

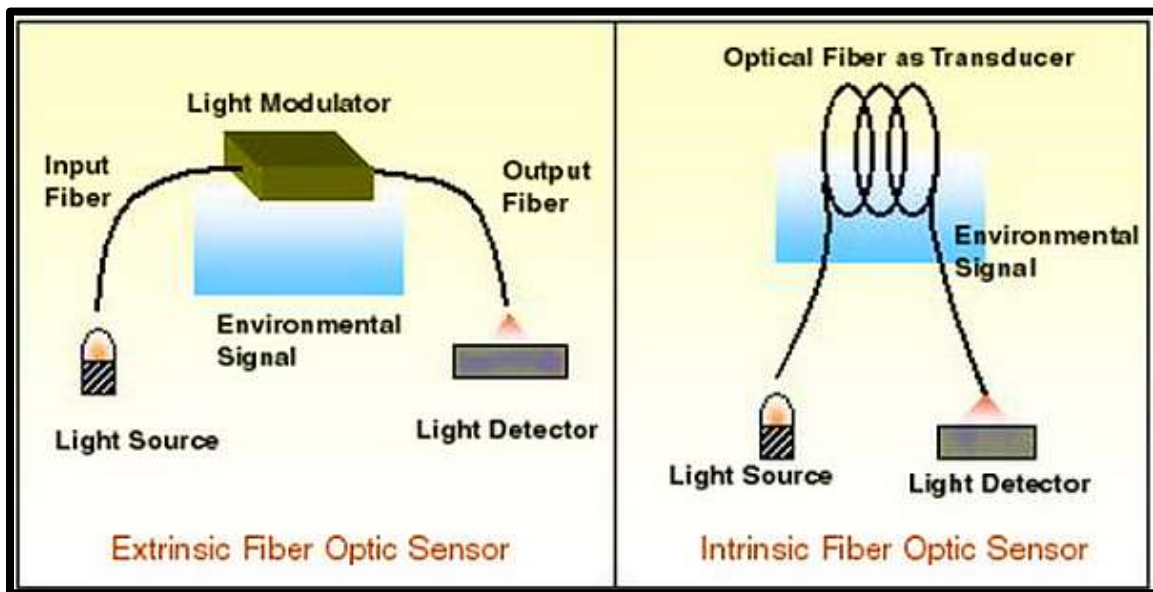


Fig. (1.5): Categorization of optical fiber sensors: (a) Extrinsic. (b) Intrinsic [37].

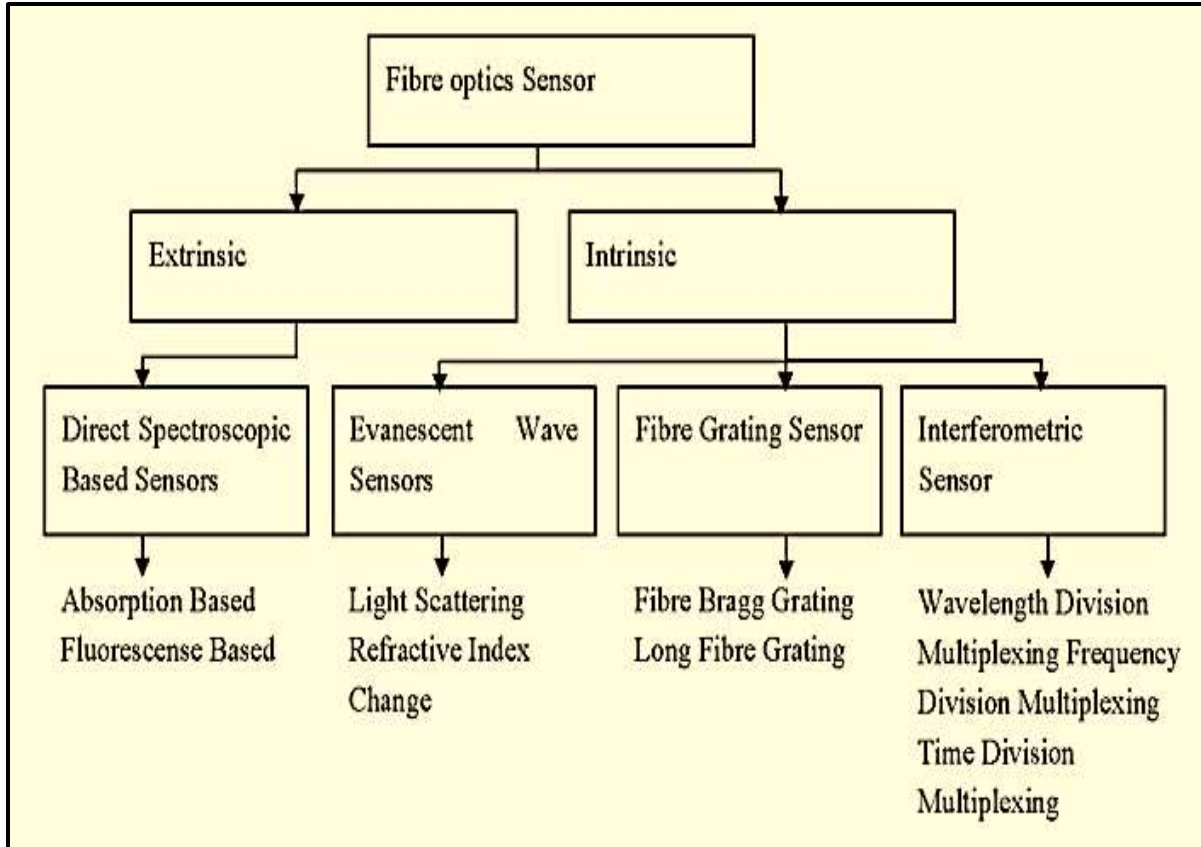


Fig. (1.6): Optical fiber sensor [49].

### 1.5 Optical fiber bending loss:

Optical fibers suffer radiation losses at curves on their paths. This is due to the energy in the evanescent field at the bend exceeding the velocity of light in the cladding. Bends are divided into two types: Macro bend loss which refers to losses generated in bends around mandrels of a specified diameter. Microscopic bends with radius of curvature approximating to the fiber radius mustn't be produced in the fiber cabling process. These so-called micro bends loss denotes to specified minimum scale "bends" in the fiber, often from pressure applied on the fiber itself [35].

### **1.6 Interferometer fiber optic sensors:**

The fiber interferometer is the key element participating in fiber communication, fiber laser, and fiber sensor. In the field of fiber communication, the fiber filter can be utilized for optical signal processing [50]. While the applying of a Fiber interferometer within a fiber laser cavity to tune and select the laser frequency has been utilized widely in recent years. They are thoroughly investigated in various detecting areas of physical parameters measurement including force [51], temperature [52], displacement [53] refractive index [54], etc. The interferometer is an optical device that produces an interference pattern across the superposition of two or more waves. In the case of the FOS domain, since the interferometers offer lots of temporal and spectral information as to their signal, the measurement can be quantitatively verified by many methods of sensing the changes in the wavelength, intensity, phase, bandwidth, frequency, and so on. With these sensing gauges, they can provide significant performance in a high-level of accuracy, large dynamic range, and superior sensitivity [55]. As the best candidate to implement miniaturized fiber optic in there exists four main kinds of interferometer configurations are recognized according to their different geometry, sensitivity, and operating principle. Generally, the Sagnac, Michelson and Mach-Zehnder interferometers work rely upon two-beam interference, while Fabry-Perot interferometer works on multi-beam interference principle. Among the numerous optical fiber configurations, we just discussed the FPI and MZI geometries since they are the most commonly studied and investigated for FOS evolution. Additionally, the recent trends of FOS advancement involved the development of an in-line interferometric sensor. Especially, the in-line interferometric sensor proposes great coupling qualifications, easy alignment, and high stability [55,56].

### 1.6.1 Fabry-Perot interferometer (FPI):

A Fabry-Perot interferometer (FPI) geometry consists of an optical cavity formed by two parallel mirrors located at certain spaced to each other [55]. Sometimes it is known as an etalon [57], in which the principal of an FPI is expressed in terms of multiple reflections. Among the mirrors introduce multiple beams that interfere with each other. Against the fiber optic cases, the FPI can be easily created by building up reflectors inside or outside of fibers [58].

The fiber FP interferometric sensors can be categorized into two types: extrinsic and intrinsic [59,60]. The extrinsic FP sensor employs two cleaved fiber segments physically separated but attached with an external housing material [61,62]. Despite the extrinsic one has been applied in many applications, but still have a limitation in the detecting cavity distance due to low coupling efficiency, packaging problem and difficult to align. On the other hand, the intrinsic FP sensor has a sensing element within the fiber itself and hence can overcome several of the difficulties of the extrinsic ones [55,63]. The local cavity of the intrinsic FPI can be designed by numerous techniques such as fiber Bragg gratings (FBGs) [64,65], micromachining [66,67], in-film deposition [68,69], and chemical etching [70,71]. But it still has some limitations such as complicated fabrication processes or high-cost equipment are required for cavity formation. The two categories of FPI are shown in Fig. (1.7).

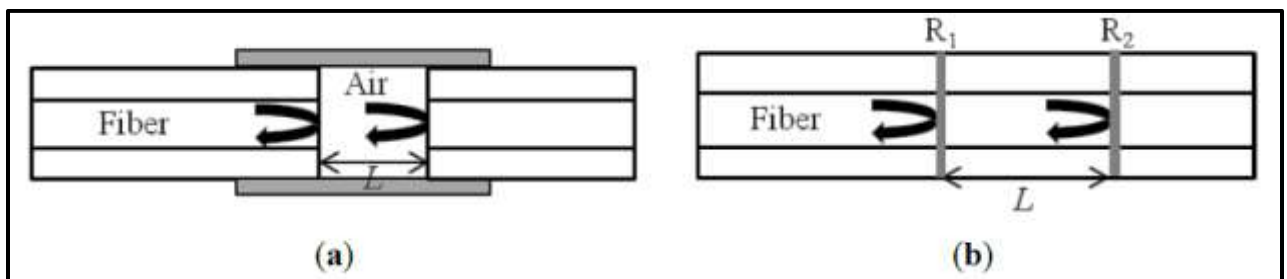


Fig. (1.7): Fabry-Perot interferometer categorized into (a) extrinsic (b) intrinsic [55].

### 1.6.2 Mach-Zehnder interferometer (MZI):

All-fiber Mach-Zehnder interferometer (MZIs) has received great attention and is widely utilized in various optic sensor applications due to its several advantages such as high sensitivity, design flexibility, compact size, and low-cost fabrication process [72]. Early MZIs had two separate arms, which are the reference arm and the sensing arm. Herein, light from the transmission fiber is split into two arms by a fiber 3-dB coupler and then light beams will be recoupled by using another fiber coupler, as demonstrated in Fig. (1.8). Therefore, an interference pattern forms according to the optical path difference (OPD) among the two arms will be created [73]. For detecting applications, the reference arm is coating with a protective layer to isolate it from external variation. Accordingly, just the sensing arm is exposed to the external variation like temperature, strain, refractive index, and others, which can be simply sensed thru analyzing the alteration in the interference signal [55,72,74]. Whilst, the reference arm remains isolated from variations. The OPD between the two arms happens as a result of varying lengths of one of the arms otherwise by insertion of a sample within the path of one of the beams (varying the optical path length through varying the refractive index). Besides, these double-arm fiber MZIs have several restrictions for instance complexity in the configuration creation, large size, and cost-effectiveness. An in-line fiber MZI depending on core-cladding mode coupling has been utilized to overcome the aforementioned drawbacks [50]. Herein, the two light arms are within the same optical fiber. The OPD between the core and the cladding modes is creating because of the relative alteration in the refractive index among core and cladding. The incident light beam will propagate across the same physical fiber length but within various optical path length owing to modal dispersion; the core mode beam has a greater effective index than the cladding mode beam [55]. There are numerous structures commonly utilized to form in-line

fiber MZIs, i.e. Core-misalignment, taper, fiber Bragg grating (FBG), core-offset, which explain in the next sub-sections.

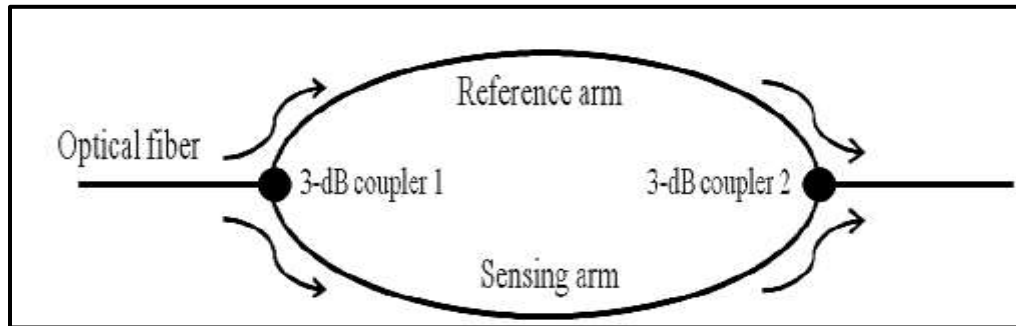


Fig. (1.8): The diagram of MZI [55].

### 1.6.2.1. Mach-Zehnder interferometer with core-mode mismatch:

Core-mode misalignment between two fiber segments can also affect a portion of core mode light coupled into cladding modes. Through this technique, the beam inside the optical fiber is to utilize fibers having various core sizes or various mode field diameters (MFDs) as demonstrated in Fig. (1.9). In this design, the fabrication method is simply verified by splicing an MMF with two short sections of SMF (SMF-MMF-SMF MZI structure) [75]. The MMF has a greater core size besides standard SMFs. However, the variance in MFDs among the fundamental core mode of the SMF in addition to MMF leads to the splitter fraction of the fundamental core mode from SMF and excitation of the first limited modes supported in MMF. These modes will be joint again in the second spliced locations.

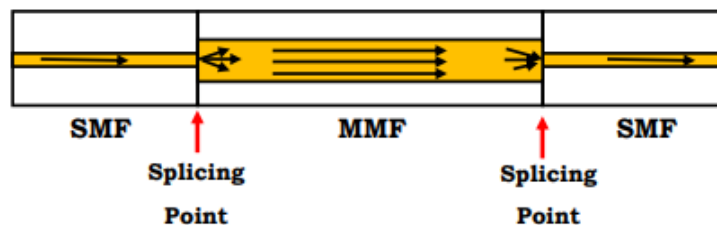


Fig. (1.9): core-mismatch MZI configuration [55].

### 1.6.2.2. Mach-Zehnder interferometer with tapered fiber:

A different strategy for exposing the evanescent field to an outer sensitive coating is fiber tapering. Tapered MZI structure can be formed by stretching the fiber whilst it is heated over a localized region or using some chemical liquids to etch the fiber. It is an efficient technique to convert a relatively greater ratio of energy in the fundamental mode toward the high-order cladding modes within optical fiber [76]. As light travels through the tapered fiber section where the diameter of the tapered fiber is only some microns, the original fiber core comes to be very small that it has a noteworthy effect any more. Hence, the energy loss of the fundamental mode would be combined with the high order cladding modes. An effective in-line tapered MZI can be constructed by tapering a fiber at two-point all along with the fiber as illustrated in Fig. (1.10) [77]. This technique is costly and uncomplicated but fragile mechanically largely at the tapering zone. This kind of interferometer is extensively utilized in detecting applications, mainly in temperature as well as refractive index sensors because it has extremely sensitive to external interruption [76].

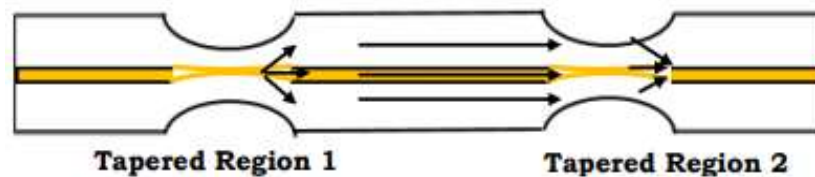


Fig. (1.10): A tapered fiber MZI configuration technique [55].

### 1.6.2.3 Fiber Bragg Grating Based MZI:

This form of in-line fiber MZI has a couple of fiber Bragg grating (FBGs) in which a fraction of the light beam directed as a fundamental mode in the core of the optical fiber is altered to cladding modes thru the initial FBG, at this point the core and the cladding modes are excited, after that the core and cladding modes are recoupled once again to the fundamental mode (core modes) thru the second

FBG [78]. Generally, there are double types of this interferometer, short period FBG with many sections submicron enough period and long-period grating (LPG) including period ranging around  $100\ \mu\text{m}$  to  $1\ \text{mm}$ . The configuration of an LPG-MZI is illustrated in Fig. (1.11). This interferometer is favored in RI detecting usages. The most important point of this interferometer is functioning in limited bandwidth of wavelength since the phase-matching phenomenon of fiber gratings as well as the LPG should be the same to have supreme performance.

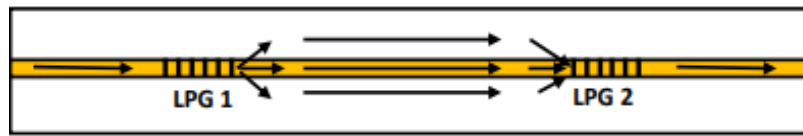


Fig. (1.11): A LPG MZI configuration technique [55].

#### 1.6.2.4 Core-Offset fiber MZI:

The core-offset MZI configuration is designed by fusion splicing two sections of fibers with a pre-set lateral offset value i.e. commonly several micrometers. Owing to this calculated offset, the interference will happen among the core mode and the cladding mode. Just as Fig. (1.12) shows a portion of the light beam guided into the lead-in fiber in the form of core mode, a part of the light beam guided across the fiber in the form of core mode; will be split into double paths. The first section describes the modes still directed inside the core and the core mode give-up a certain amount of its energy to stimulate the cladding modes. Core-offset MZI has been utilized as an optical attenuator in the field of optical communication systems [79]. On the other hand, the structure is easy to break and fragile [51].



Fig. (1.12): A core-offset fiber MZI configuration technique [55].

### **1.6.2.5 Mach-Zehnder interferometer with bending fiber sections:**

Most of the above-mentioned techniques are based on utilizing a linear active sensing section. But, an additional method for splitting the light beam in an optical fiber by using macro-bent fibers as optical detecting elements has also been proposed to improve the sensitivity and the resolution of the fiber sensors. Recently, lots of configurations based on bent fibers are utilized as optical sensing configurations such as a u-shaped, c-shaped, s-like, cascading multiple ring bent fibers [80] and balloon-like bending optical fiber configuration. Over the last few years, these bent fiber sensing configurations have been employed to measure many sensing parameters including temperature, refractive index, force, and displacement [81–83]. Also, many proposed works depend on the combination of a macro-bent SMF structure with incorporating an LPG or FBG have been formed [30,84]. The balloon-like based bending fiber sensors being able to sweep a large environment with good measurement repeatability, simplicity, compactness, low cost and can be designed by various types of fibers. This structure can be fabricated by bending a section of optical fiber into the balloon-like shape utilizing a segment of a capillary tube and adjusting the radius of curvature by several millimeters. When the light reaches the balloon-shaped section, a fraction of the light be free from the core mode and penetrates the cladding as the light propagates within the balloon-like bending segment. Then, the cladding modes will have recoupled back to the core mode, accordingly, an MZI modal interferometer can be efficiently formed between the cladding modes and the remaining core mode owing to the differences in effective refractive indices RIs of the core and cladding modes. As well as the optical path differences experienced through the light signals propagating in the core and the cladding modes [52]. In this thesis, MZI based on balloon-like fiber was proposed and

constructed experimentally, the principle of operation of these MZIs interferometers will be clarified in detail in the next section.

### **1.7 Sensing Principles and Operation:**

The balloon-like fiber structure comprises a section of SMF and a capillary tube to support twisting the SMF into a balloon-like shape. With a suitable bending radius, a modal interferometer that relies on the MZI principle can be formed. As the light signal passes across the bent section, the MZI starts functioning where a fraction of the light will be free from the core boundary and transmitted into the cladding. This light will couple back again into the fiber core at the waist of the bend. The optical path length difference between the cladding modes and the core modes will form the modal interference. This phenomenon would occur between the cladding modes and the residual core modes owing to the change in their effective refractive indices. Generally, a part of the light packet escapes into the cladding, but some of the light signals also escape into the coating layer, which excites coating modes. These exciting coating modes are transmitted within the SMF coating, as well as reach the coating/air boundary, and a part of this signal is recoupled back to the core of the fiber. On the other hand, the bent fiber will increase the penetration depth of the evanescent field which leads to a significant enhancement in the sensitivity as soon as the configuration is utilized to measure specific chemical/physical phenomena [37,33]. Moreover, the dimensions besides the refractive index of the fiber core and the cladding, in addition to the coating modes, are extremely sensitive to the measurement of various physical quantities such as temperature. Due to The thermal expansion coefficients (TEC), intrinsic thermo-optic effects coefficients (TOC), photo-elastic properties of the silica fiber, the refractive index of the fiber core, the core diameter, and the length of the fiber are all temperature-dependent. Hence, the spectral shift of the transmitted spectrum

through the fiber alters along with the surrounding temperature. The resolution of the related wavelength shift produced by temperature changes can be expressed as:

$$\frac{\Delta\lambda}{\lambda} = (\alpha + \varepsilon)\Delta T \quad (1.1)$$

Where  $\alpha$  and  $\varepsilon$  are the TEC and the TOC of the fiber, respectively.  $\lambda$  is the wavelength of light.

Accordingly, the modes propagated in the fiber vary with varying temperatures, resulting in a change in the output spectrum which induces a wavelength shift as detected in the spectral response of the fiber sensor [37]. In the case of a standard two-mode shaped MZI modal interferometer, the transmitted intensity is given by [33]:

$$I_{out} = I_{co} + I_{cl} + 2\sqrt{I_{co}I_{cl}} \cos \delta \quad (1.2)$$

Where  $I_{co}$  and  $I_{cl}$  are the signal intensities of the core mode and cladding mode, respectively.  $\delta$  is the phase difference between the core and cladding modes and can be expressed as [33]:

$$\delta = \frac{2\pi\Delta n_{eff}l_{eff}}{\lambda} \quad (1.3)$$

Where  $\Delta n_{eff}$  is the effective refractive index difference, which is given as:  $\Delta n_{eff} = n_{co} - n_{cl}$ , where  $n_{co}$  and  $n_{cl}$  are the (RIs) of the fundamental modes of the core and cladding, respectively.  $l_{eff}$  is the effective bending length of the balloon-like structure,  $\lambda$  is the wavelength of the light signal in free-space. When the phase difference fulfills the condition of  $\delta = (2m + 1)\pi$ ,  $m = 0, 1, 2 \dots$ , an interference dip would happen at certain wavelengths.

$$\lambda \text{ dip} = \frac{2\pi\Delta n_{eff}l_{eff}}{2m + 1} \quad (1.4)$$

## 1.8 Coating materials:

Optical fiber sensors have drawn considerable attention for their broad range of potential applications including environmental assessment [45], biochemical

analysis [10], and in the chemical industry [86]. Despite these advantages, they still have limited sensitivity. Therefore, fiber sensor-based electromagnetic mode resonance configurations (EMR) have for some time been regarded as a feasible solution to addressing and improving the sensitivity issue, response time as well as detection limits of fiber sensors [87]. For EMR creation, the fiber sensors necessitate a thin film deposited on an optical waveguide. Thin film-deposited optical waveguides have been a principal contributor to the optimization and improvement of sensor performance using various innovative materials and deposition techniques [88]. Tuning of the thin film features via their manufacture allows excellent sensor performance to be attained in terms of sensitivity [88]. Accordingly, numerous materials have already been utilized to obtain EMR-based fiber sensors that include polymers [89], metals nanomaterials [90], metals oxide nanomaterials [45], and diamond-like carbon [91]. Many thin-film features must be taken into consideration, especially the permittivity and film thickness. Besides, several materials may vary in their features terms of in temperature, humidity, or the existence of specific gases, which effectively determines their range of application [87]. The next sub-sections explain in detail the materials used in this research and their properties.

### **1.8.1 Acrylate Polymer:**

Recently, acrylate polymers play an important function as optical adhesives utilized in the covering and construction of optical communication units [92]. These polymers type offer advantages in terms of physical features, cost-effectiveness, and flexibility to mass production. Also, acrylate polymers possess a broad refractive index range (1.40 –1.70) with high transparency of  $\sim 90\%$ , efficient thermal expansion coefficients (TECs), excellent thermo-optic coefficients (TOCs) ( $\sim \pm 10^{-4}$ ), and good thermal conductivity ( $0.155 \text{ W m}^{-1} \text{ K}^{-1}$ ) [92,93]. Generally, this type of polymer has been used among light passing

segments for the goal of reducing the reflection losses in bundles [92]. On the other side, this polymeric type is particularly sensitive to environmental status, including temperature and humidity [94]. In general, the refractive indices of various optical polymers have been studied and were found to decrease at a rate of  $-10^{-4}/^{\circ}\text{C}$  [95]. In addition to the refractive index, these are other significant factors that are distinguished to be changed by the influence of environmental states, such as hardness and thermal expansion coefficient. In the case of the acrylate polymers based-optical fibers, these variations in temperature and humidity would influence the signal behavior. This is due to the change in the RI of both the optical and the polymer material [92].

### **1.8.2 Polyvinyl Alcohol (PVA):**

PVA is a translucent and water-soluble polymer broadly used in many fields of application owing to physical /mechanical properties such as good chemical resistance, solubility with water, dielectric strength, and adequate storage capacity, efficient thermal expansion coefficients (TECs), excellent thermo-optic coefficients (TOCs) ( $\sim\pm 10^{-4}$ ), extreme flexibility, cost-effective, fabrication easiness, non-toxic, besides their optical inquiry [96–98]. Also, PVA possesses tunable RI and swelling features [97]. Moreover, the PVA has a large thermal conductivity ( $0.28 \text{ W m}^{-1} \text{ K}^{-1}$ ) and melting point  $\sim 200^{\circ}\text{C}$  [98], which can transfer the heat from the surrounding environment to the coating substrate more efficiently. Accordingly, it can be used for coatings, adhesives, binding industries, plastics, and optoelectronic because of its impact on physical investigations and its ability to form films [96]. PVA chemical formula and density is  $(\text{C}_2\text{H}_4\text{O})_x$  and  $1.19 \text{ g/cm}^3$ , respectively. Also, it is considered to be biocompatible, thermally stable, and hydrophilic which available in white powder form with varying grades

and solubility properties [99]. It has limited absorption in the visible domain with highly transparent in the infrared region [96,98].

### **1.8.3 Gold nanoparticle (Au-NP):**

The evolution and development of nanotechnology lead the innovation towards high-speed electronics, high-efficiency catalysts, and sensors [100]. Nanotechnology is described as materials whose external or remote dimensions are measured on a scale in the range of (1-100) nm. Also, nanotechnology has facilitated the researchers to modify the physical properties like roughness, thickness, surface area, electrical, bandgap, and additional properties as well as a RI to build a smart superior sensor [101,102]. This is motivated by the well-known unique properties of the metallic NPs, such as high surface to volume ratio, optical, chemical, and electronic properties that are different compared with those of bulk materials [103]. In the advancement of the sensing device, FOS utilizing nanomaterial has gained a lot of interest in research work and application owing to their specific features that vary from bulk materials. Such sensors could show good selectivity, faster reversibility, and higher sensitivity [61,104]. Among the nanosized metallic materials, gold nanoparticles (Au-NPs) as a sensitive coating have been widely used for optical sensing applications owing to their very good optical properties [105]. Au-NPs have a large surface-to-volume ratio, their localized surface plasmon resonance (LSPR) phenomenon, wide absorption band, chemically stable, fast response time, and more negative Fermi potentials due to the quantum confinement effect. Also, Au-NP widespread utilized for temperature sensing applications due to its advantages in terms of non-toxic, good sensitivity, good thermo-optic coefficient, excellent thermal expansion coefficient [106–109]. As the RI of Au-NPS is higher than silica optical fiber, then the guiding light will couple into Au-NPs waveguides [34]. Controlling the thickness of the coating on a

nanometer scale is an important feature for the sensors based on the interaction of the evanescent field with the coating because the coating thickness should be always below the penetration depth of the evanescent wave [110]. The evanescent wave absorbance is a high reliance on the concentrations of the analyte if other parameters remain constant. In References [111], it is found that the refractive index (RI) of the coating layer experienced by the mode interacting with the coating depends on the thickness of the coating layer and the sensor sensitivity and response time can be optimized by controlling the coating layer thickness.

Additionally, one of the most well-known unique optical features of Au-NPs is their localized surface Plasmon resonance (LSPR) phenomenon [133,134]. Once noble metals, such as gold, are exposed to light, a resonant interaction between electron-charged oscillations close to the surface of the metal and the electromagnetic field of the light generates propagating surface Plasmons. This unique physical property changes extremely when the size of metal becomes nanoscale relative to the bulk material, causing a confined and non-propagating localized surface plasmon around the nanoparticle thru a specific frequency identified as the LSPR [134,135]. In the certain case of Au-NPs, the LSPR yields exceptionally great absorption coefficients and scattering properties in the visible to near-infrared (NIR) wavelength range [135,136]. These spectral features of GNPs are independent of shape, size, and the local dielectric environment [137].

### **1.9 Coating Methods:**

Thanks to various innovative techniques that have been formed for the deposition on or at the optical fiber surface to purpose a novel sensing FOS. Various techniques are widely adopted for FOS development due to simplicity, and reproducibility. Many techniques have been applied for prepared and deposited nanoparticles onto the target substrate such as thermal

evaporation [62], chemical vapor deposition [112], and sputtering [113]. The next sub-sections explain in detail the methods used in this research.

### **1.9.1 Casting Method:**

The Drop-cast technique is simple and straightforward. Drip a coating solution onto a fiber surface or deposited the fiber section on the coating solution and let it dry to make a thin layer. This technique was utilized in many research [103,114]. The thickness of the thin layer can be controlled depending on the concentration of the solution and the number of times this process is repeated. The process can also be repeated until the desired thickness is achieved.

### **1.9.2 Magnetron Sputtering Method:**

One of the best techniques for depositing thin material layers is magnetron-sputtering, which has several benefits for the preparation of bulk silica-supported gold nanoparticles. Since no solutions are demanded to prepare the catalysts as well as no thermal treatment or activation is required to obtain an active catalyst [115]. This technique has a high deposition rate which causes a high bonding strength between the coating material and the substrate, where the thickness and the uniformity of the coatings can be precisely controlled through the accurately selected deposition parameters [110].

---

## **1.10 Temperature sensor for biomedical application:**

Temperature monitoring could be a potential tool for different diseases which can play a vital function in public health in terms of the outbreaks and limits [5,6]. The current epidemic of 2020 new coronavirus (COVID-19) has concerned global consideration owing to its massive and rapid transmission capacity and almost an elevated death rate [116,117]. The reported symptoms of COVID-19 patients are fever, dry cough, and tiredness [118,119], where the vast majority of the patients

suffer from fever before endorsement with it mostly being the first indication. The currently available measuring devices like a non-contact infrared thermometer and infrared tympanic thermometers widely used in such circumstances must respond fast for comprehensive monitoring and permits a quicker triage [120,121]. Moreover, indirect touches with infected persons may rise the danger of cross-infection [122]. On the other side, the last era witnessed development in a field of minimally invasive techniques based on thermal treatments such as Laser ablation, High Intensity Focused Ultrasound ablation, Radiofrequency ablation, Microwave ablation, and Cryo-ablation which have acquired extensive distinguishing in the area of tumor removal [10,123]. These methods generate a localized temperature rise or reduction to remove the tumor that sometimes might result in a physical injury or even permanent harm to patients [124,125]. Additionally, it worth is known that the blood flow in the tumor cells is not as appropriate as the healthy tissue; therefore the tumor cells have a slower rate of heat distribution [126]. Consequently, by heating the tumor cell for a specific time, infected cells can be ablated while the nearby healthy tissue stays intact [127,128]. A precise temperature measurement of tissue may be mainly helpful to enhance treatment results because it can be utilized as an obvious end-point to realize comprehensive tumor ablation and reduce reappearance as well as regulating delivered energy settings through therapy. Namely, the real-time response of body temperature is necessitated to confirm that the tumor tissue is heated precisely and equivalently to a critical kill temperature [2,10]. In particular configurations, the biomedical sensor based on body temperature must fulfill certain requirements such as non-toxicity sensing medium, cleaning and sterilize easiness as well as the sensor must be insensitive to other physical parameters excluding temperature [2,21,22,129]. Amongst the numerous thermometric methods utilized in this field, all-optical fiber-based temperature sensors are an attractive thermometric method that can

offer non-hurtful and ultrasensitive response characterization in the range of sub-to several milli-seconds level [7,8,130].

### 1.11 LITERATURE SURVEY:

Many research groups around the world have investigated different schemes that exploit the structure of the optical fiber temperature sensor (OFTS) technologies, so the macro-bending structure played an important role in recent years. A survey for the temperature sensor summarizes the most important published work related to the macro-bending sensor in Table (1-1).

**Table (1-1): Summary of the Published Works in OFTS**

<u>Year</u>	<u>Author</u>	<u>Structure and range of temperature</u>	<u>Coating</u>	<u>Sensitivity</u> pm/°C	<u>Ref.</u>
2010	Q. Wu et al.	SMF-bent MMF-SMF structure, in temperature, ranged from 20-80°C	acrylate coating of the MMF fiber	31.97	[131]
2015	Wei Peng et al.	Two semicircular bendings, in temperature, ranged from 16-36 °C	the protective coating is stripped off	-260	[80]
2015	Yaofei Chen et al.	Balloon-like interferometer based on a bent of coating-stripped SMF with FBG's pigtail, in temperature, ranged from 25.4-95.4 °C	the protective coating is stripped off	10.3	[132]
2015	M. Y. Mohd Noor, et al.	A segment of MMF bending into balloon-like, in temperature ranged from 27-31°C.	acrylate coating of the MMF fiber	-2060	[29]

2016	QUN HAN et al.	A macro bent fiber Bragg grating (FBG) structure, in temperature, ranged from 20-93°C.	the protective coating is stripped off	31.7	[30]
2017	Shiyang Xiao et al.	Balloon-like interferometer based on a bent of coating-stripped SMF, in temperature, ranged from 10-70 °C.	the protective coating is stripped	91.8	[51]
2018	Ke Tian et al.	Balloon-like interferometer based on a bent standard uncoated SMF configuration with LPG, in temperature, ranged from 20-45 °C.	the protective coating is stripped off	42.9	[84]
2018	Ke Tian et al.	Balloon-like interferometer based on a bent standard un-stripped SMF, in temperature, ranged from 20.7-31.7 °C.	retains its original protective polymer coating.	-2465	[28]
2019	Yue Wu et al.	Balloon-like interferometer based on a bent standard uncoated SMF configuration with FBG. in temperature ranged from 20-70 °C.	the protective coating is stripped off	105	[133]
2019	Lilong Zhao et al.	Balloon-like interferometer based on a bent standard uncoated SMF configuration, in temperature, ranged 40-90 °C.	the protective coating is stripped off	22.9	[52]
2019	I Yuliant i et al.	(MZI) consist of two coupled polymer optical fibers using two couplers, in temperature ranged from 40-80 °C.	the protective coating is stripped off	082.2	[134]

**1.12 AIM OF WORK:**

In the present work, we intend to take the following steps:

1. Fabricate and implement the balloon-like fiber structure as a temperature sensor.
2. study effects of Stripped-off the original protective coating, retained the original fiber jacket, coating by polyvinyl alcohol (PVA), and with gold NPs coating layer on the active segment of the sensor parameters.
3. Enhance the sensing performance by coating the sensing head with PVA and GNP.

## *Chapter Two*

### *Experimental Methodology*

## CHAPTER TWO

### Experimental Methodology

#### 2.1 Introduction:

Optical fiber sensors have attracted special attention in a broad range of potential applications including environmental assessment, biochemical analysis, and in the chemical industry. Among several sensors structures comprising the sensor setup, all-fiber interferometers based sensors have been proposed and demonstrated to monitor various parameters. In this chapter, temperature modal interferometer sensors based on macro-bending fiber structure have been designed and constructed. The working principle of the macro-bending interferometer and the factors sensitive to change in temperature has been elaborated. This sensor configuration comprises of a standard SMF that bent with a specific bent diameter with the assist of a section of a capillary tube. The two ends of the SMF were confined inside the capillary tube. The interference takes place between the core mode and cladding modes stimulated by the bent SMF. The experiments were carried out utilizing an optimal bending radius. Also, to enhance the temperature detection performance, the active sensing area of the fiber structure was coated with PVA and GNP. The structure of chapter two is presented in Fig. (2.1).

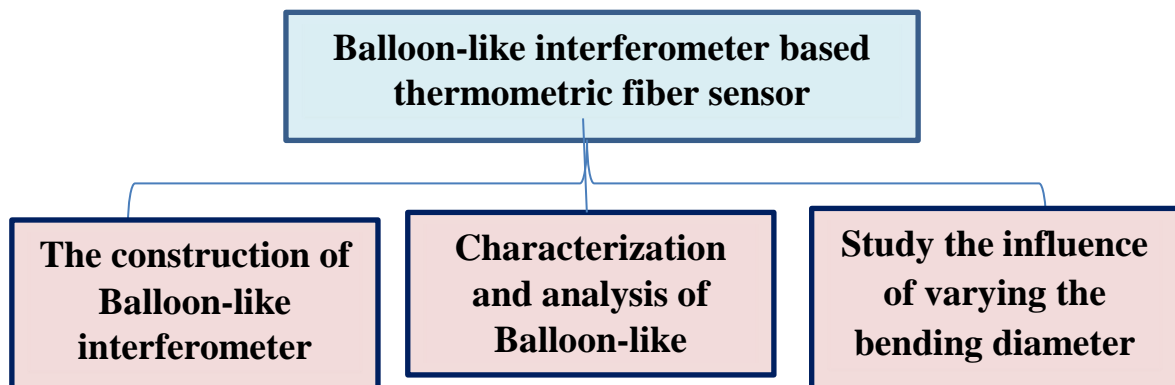


Fig. (2.1): structure of chapter two.

## 2.2 System Layout:

The system layout of the fiber optic temperature sensor based on the balloon-like structure is shown in Fig. (2.2). All information of this system, methods, and fabrications will be described comprehensively in the following sub-sections.

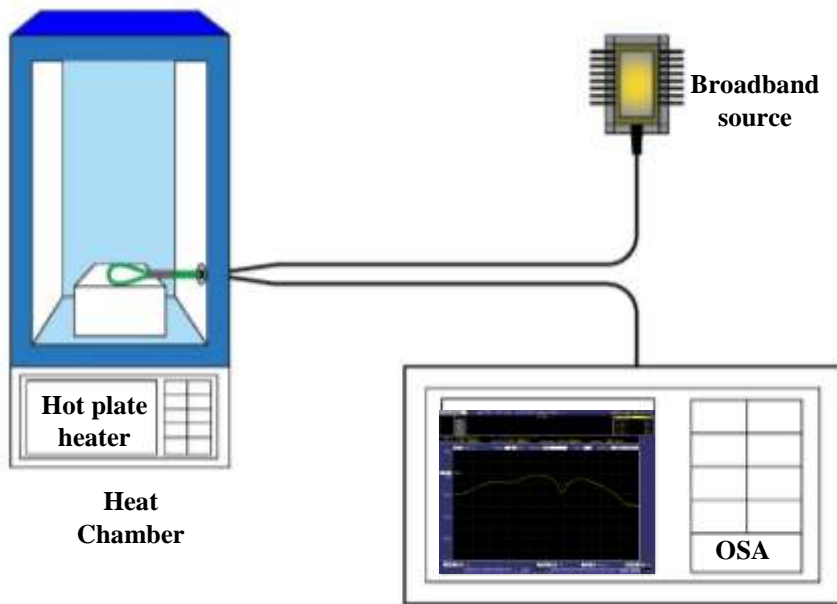


Fig. (2.2): Schematics diagram of temperature sensor based on balloon-like fiber structure.

### 2.2.1 Broadband Source (BBS):

In our work, a butterfly-packaged Super-Luminescent Diodes (Thorlabs SLD1550s-A1) with 1450-1650 nm emission range has been used as a broadband light source (BBS). This source has an output spectral profile near-Gaussian with a low-ripple. This device comprises of a current controller, IC chip with a 14-pin butterfly package (of dimensions 15 mm×22 mm×8 mm), combined with a thermoelectric cooler and a thermistor to confirm the stability of the output light. The IC chip is mounted on the thermoelectric cooler through a sub-mount (heat sink) with high thermal conductivity to waste the heat created from this chip as efficiently as feasible. Also, this device contains an optical coupling arrangement to couple the light beam to

the optical fiber, which its output connect with a SMF pigtail of ~ 1m length, ended with a 2.0 mm fine knob FC/APC adapter. [Appendices A, B, and C].

### 2.2.2 Single-Mode Fiber (Corning SMF-28):

A standard telecommunications SMF (Corning SMF-28) is the fiber used in this experiment. The Corning SMF-28 is manufactured to carry the highest capacity of information, and its operation lies in the 1310 nm and 1550 nm wavelength region possesses the lowest dispersion property. The Corning SMF-28 has standardized geometric properties occupations with low attenuation and excellent reliability to provide high performance. The optical specifications of Corning SMF-28 are presented in Table (2.1)

**Table (2.1): Optical specifications of Corning (SMF-28) [Appendix D].**

<b>Fiber attenuation</b>	
Wavelength (nm)	Maximum value (dB/km)
1310	0.33-0.35
1550	0.19-0.20
1625	0.20-0.23
<b>Mode-Field Diameter (MFD)</b>	
Wavelength (nm)	MFD ( $\mu\text{m}$ )
1310	$9.2 \pm 0.4$
1550	$10.4 \pm 0.5$
<b>Dispersion</b>	
Wavelength (nm)	Dispersion value [(ps/(nm*km))]
1550	$\leq 18.0$
1625	$\leq 22.0$

### 2.2.3 Optical Spectrum Analyzer (OSA):

An Optical spectrum analyzer (OSA) is a precision device utilized to display and measure the alteration of power of the optical source over a specified wavelength span. The OSA traces display wavelength in the horizontal scale and power on the vertical scale. The optical spectrum analyzer OSA (YOKOKAWA, Ando AQ6370) is utilized to monitor the variation in the interference spectra of the sensor with temperature variation in this experiment. Fig. (2.3) illustrates the image of OSA utilized in the experiment. Characteristics of this device are:

- Wavelength range: 600nm to 1700nm
- Wavelength accuracy:  $\pm 0.01$ nm
- Wavelength resolution: 0.02nm
- Dynamic range: 78dB typ.
- Level range: +20dBm to -90dBm
- Fast measurement: 0.2 sec. (100nm span)
- Applicable to single-mode and multimode fibers



Fig. (2.3): Photo-image of the optical spectrum analyzer (OSA).

## 2.2.4 Temperature Chamber and Hot Plate:

A sealed cylindrical-shaped chamber made from Pyrex glass was used to carry out the experiment. The chamber contains three orifices where two of them were used to support the fiber structure inside the chamber. While the third orifices were used for the thermocouple in order to measure the temperature inside the chamber. A separate digital hot plate temperature controller with a heating power of 600 W and a maximum temperature of 350 C° (SH-4C digital magnetic stirrer hot plate) was used for monitoring the temperature inside the chamber.

## 2.3 Experimental Procedures of the Work:

The experimental procedure follows many steps to fabricate the balloon-like fiber structure based on MZI. It will explain as follows:

### 2.3.1 The macro-bent fiber structure:

The schematic diagram of the balloon-like structure is shown in Fig. (2.4).

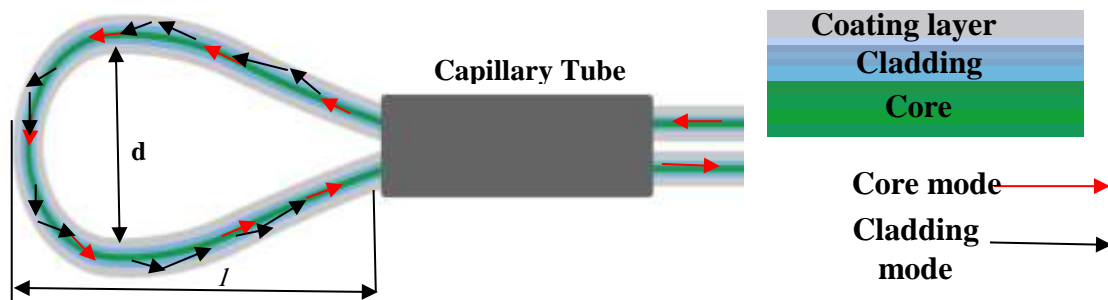


Fig. (2.4): Schematic of the balloon-like structure.

The balloon-like structure was fabricated by bent a piece of bare SMF-28 into a balloon shape by injecting both sides of this fiber through a glass capillary tube of length 1.3 cm and an internal diameter of 800  $\mu\text{m}$ . The bending diameter and the overall length of the balloon-like structure section are termed as  $d$  and  $l_{eff}$ , respectively. One end of the bent structure was connected to the OSA while the other part was connected to the B.B.S.

### 2.3.1.1 Fusion splicing

splicer from Fujikura (FSM-60S) has been utilized in the experiments for splicing. Fig. (2.5) shows a photograph of (FSM-60S) fusion splicer (Fujikura Company).



Fig. (2.5): photograph of (FSM-60S) fusion splicer

### 2.3.2 Study the Influence of Varying the Bending diameter:

In this study, the influence of various bend diameters has been investigated experimentally. After collecting information from the OSA, the optimal bending diameter was selected. When the bending diameter is 1.5 cm or more, no resonance interference pattern occurs within the wavelength range since hardly any light is coupled into the SMF cladding and/or coating modes. As the bending radius decreases, more signals will leakage into the fiber cladding modes and recouples back to interfere with the residual core mode. From Fig. 2.6(a-c) it can be observed that as the bending diameter decreases to values between 1.3-1.2 cm, no recognized interference dip was noticed again, which may be owing to the high loss caused by the variance in optical path lengths of the SMF core and cladding. Furthermore, at 1 cm bend diameter, there is an obvious interference dip that was noticed with a

reasonably large extinction ratio (more than 18 dB). But then, if the bending diameter reduces further, an excess of light signals will escape into the cladding and also leak out of the fiber causing in a weak Modal interference and substantial loss so the intensity of the output signal reduces significantly.

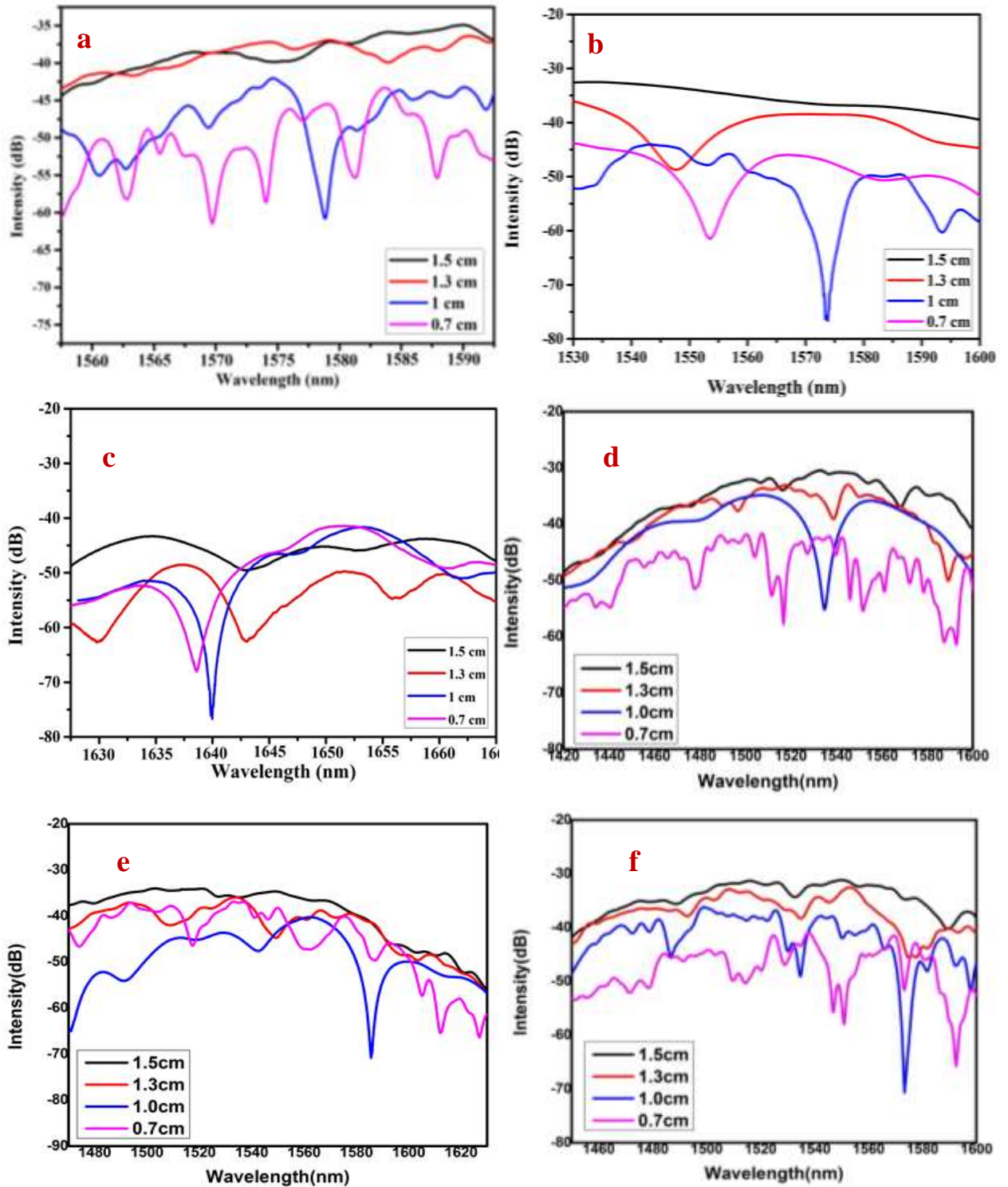


Fig. (2.6): Transmission spectra of the macro-bent formation with different bending diameter (a): stripped-off the original protective polymer coating, (b) retain the original protective polymer coating (c) PVA-based fiber coating and (d) GNP-based coating with 10 nm thickness layer (e) GNP-based coating with 20 nm thickness layer (f) GNP-based coating with 30 nm thickness layer.

From the above, the optimum bending diameter of 1 cm was selected to form the balloon-shaped structure due to its resonance fringe has a high depth and narrow bandwidth. Also, it can be noticed that without an original protective coating, the glass fiber in the cable is easily broken.

### **2.3.3 Sample Preparation and characterization based-PVA coating:**

After choosing the optimal bending diameter to form a macro-bent structure sensor, SMF encapsulated by a layer of a polymeric material (Polyvinyl alcohol "PVA") using slow evaporation of solvent (dip-coating) technique. The depositing process started with the preparation of the PVA solution. Initially, a 0.5 mg/ml PVA aqueous solution was prepared by dissolving a specific quantity of PVA into deionized water and stirring by using a magnetic stirrer at 90 °C for one hour until solute was completely dissolved and the solution becomes good homogenous. After that, the PVA solution was cooled down at room temperature before utilize; which exhibits a viscous semblance at room temperature. Moreover, the protective coating of SMF was stripped-off, then deposited with the PVA polymer layer by immersing the stripped-off fiber in the polymer aqueous solution, the encapsulated SMF left to dry for one day before employing it.

The morphology of the PVA layer was characterized by utilizing scanning electron microscopy (SEM), as illustrated in Fig. (2.7).

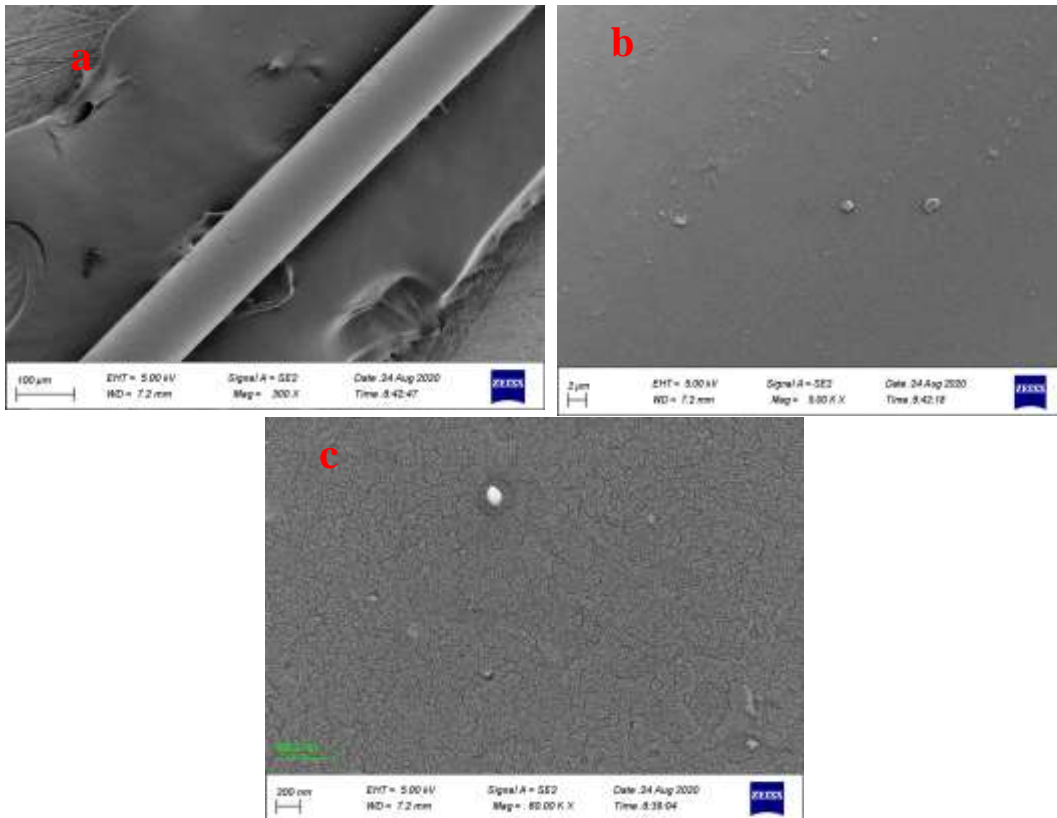


Fig. (2.7): SEM images of (a) 100  $\mu\text{m}$ , (b) 2  $\mu\text{m}$  and (c) 200 nm scales.

### 2.3.4 Sample Preparation and characterization by gold nanoparticles (GNP) coating:

Gold nanoparticles (GNP) coating was applied to SMF in macro-bent fiber section to enhance the sensitivity of an optical fiber temperature sensor. Three different specimens of SMF were prepared by coating the active sensing area with GNP of 10, 20, and 30 nm thickness above the original protective polymer coating utilizing the magnetron-sputtering processes (Quorum-Q 150 RS DC sputtering device). The fabrication technique of the SMF-based GNP is explained as follows. Firstly, the SMF with a length of ~ 14 cm was put into the vacuum chamber of an in-line magnetron sputter deposition instrument. The chamber is supplied with a load-lock system and diffusion pumps with DC power suppliers and also provided with a standard stage in which the SMF segment could behold. The gold target with a

thickness of 0.1 mm, a diameter of 57 mm, and a purity of 99.99% was utilized to sputter-deposit GNP thin films upon the SMF. Sputtering was achieved at a vacuum degree of  $\sim 1 \times 10^{-2}$  mbar in a pure Ar buffer gas which the ionized Ar was excited to bombard the gold target. The stimulated gold plasma plume was then deposited onto the SMF with an effective length of about 1.5 cm gradually. Through the depositing method, the SMF section was rotated with a speed rate of  $\sim 20$  r/min to guarantee the uniformity of thin gold layers all over the effective length of SMF at a stable discharge. Three SMFs specimens with a coating thickness of  $\sim 10$ , 20, and 30 nm were achieved by changing the deposition time of 150, 300, and 450 s, respectively; The deposition rate of the coating layer was 4 nm/min. Fig. (2.8) illustrates the demonstration system of DC magnetron-sputtering.

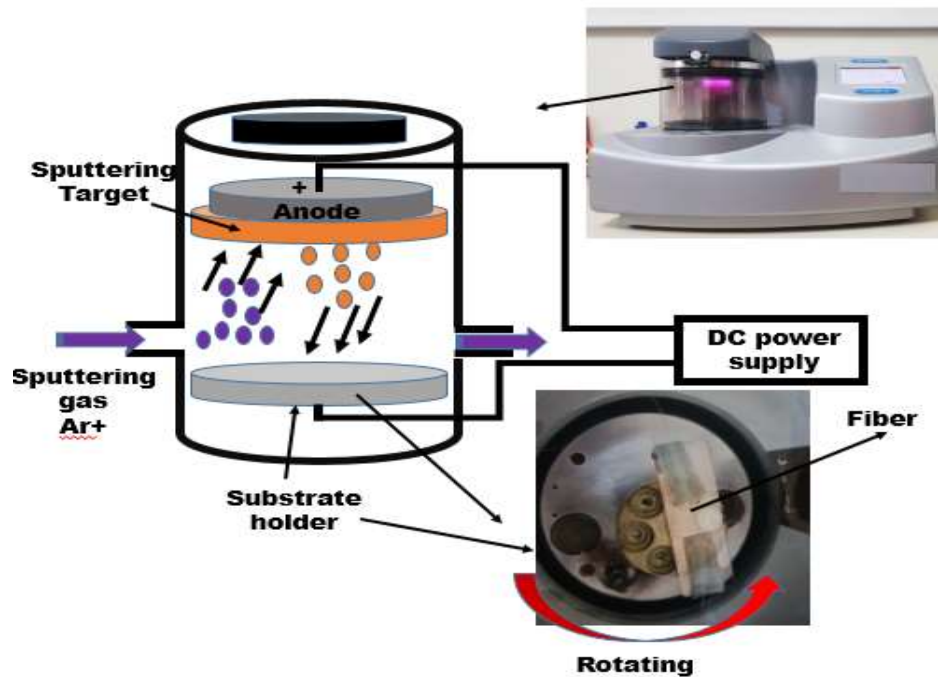


Fig. (2.8): The demonstration system of DC magnetron-sputtering.

Fig. (2.9) displays the cross-sections of the prepared Sample encapsulated by gold nanoparticles, which were imaged via the (SEM). From

this figure, it can be seen that a uniform and compact layer of GNP was certainly formed upon the all effective length of SMF.

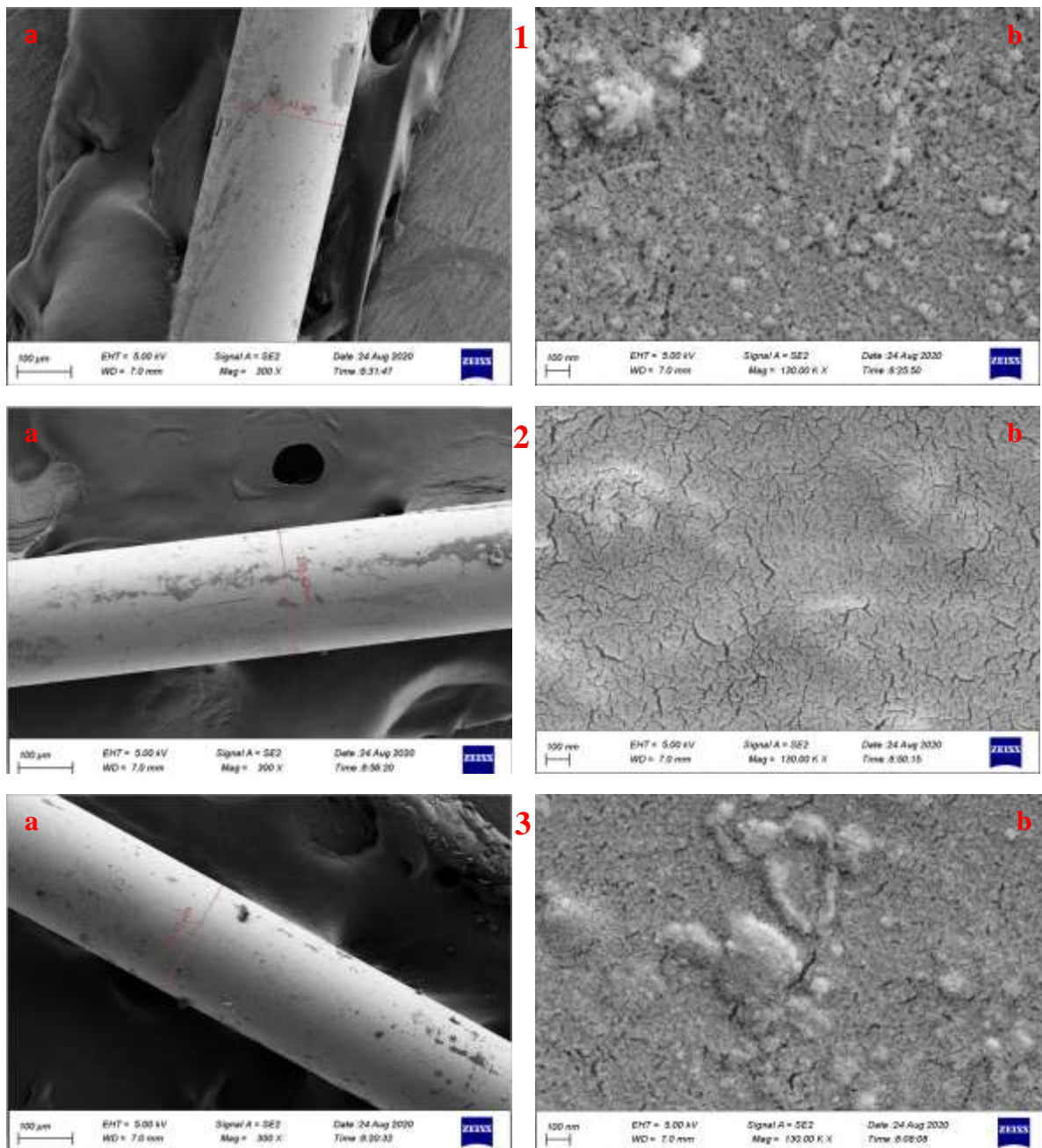


Fig.(2.9): SEM images at different scales (a) 100 μm, and (b) 100 nm for (1) 10 nm, (2) 20 nm and (3) 30 nm gold thickness layer

## 2.5 The Rise Time and resolution measurements:

The rise/response/recovery times are vital gauge to determine the performance of the sensor. The time demanded for the sensor to switched 90% of the maximum output power level through the temperature variation is the rise or recovery time [18]. In order to investigate the rise time of all fabricated sensors towards the temperature variation, each sensor was subjected to a sudden and quick change of the temperature and then the optical signal has been monitored using a photodetector. Six configuration states of a macro-bent fiber structure with 1 cm bending diameter have been examined:

- I. stripped-off
- II. with an original protective coating
- III. based-PVA coating
- IV. GNP coating with 10nm thickness layer
- V. GNP coating with 20nm thickness layer
- VI. GNP coating with 30nm thickness layer

Temperature resolution, well-defined as the minimum detectable temperature changes; There are many methods to estimate the resolution, in this work, the following formula:  $R = \frac{\sigma}{S.I_0}$

Where  $R$  is the resolution, where  $\sigma$  represents the intensity resolution of the optical power meter,  $S$  is the sensitivity,  $I_0$  intensity of dip in dB

To obtain the response time, an experimental setup (fig. (2.10)) was built, which consists of a broadband source, a photodiode detector (Gentec TPM300CE, with response time of < 1ms), and 1 GHz oscilloscope (Tektronix MDO3102).

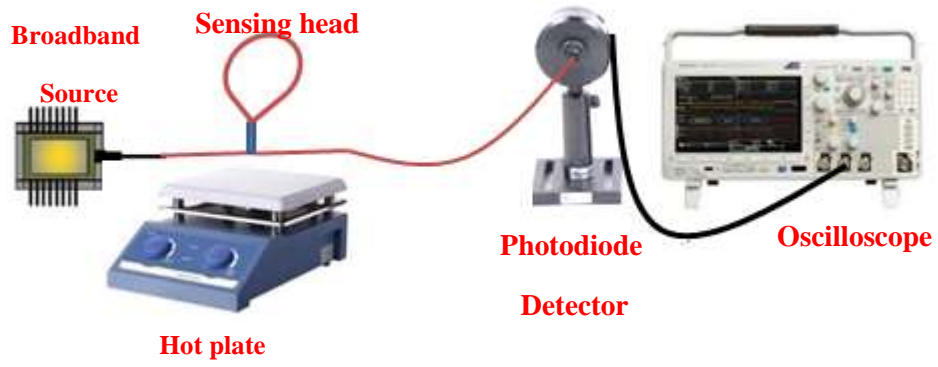


Fig.(2.10): experimental setup for response time measurement.

## *Chapter Three*

### *Results and Discussion*

## Chapter three

### Results of balloon-like interferometer thermometric sensor

#### **3.1 Introduction:**

For low-temperature sensing, a novel fiber bent techniques have been proposed and fabricated as a highly sensitive sensor. In this chapter, the characteristics of the fabricated sensor probes with temperature variations are investigated experimentally. The proposed sensors were characterized in terms of transmission spectra using a broadband source (Thorlabs SLD1550S-A1) with a wavelength range of 1450-1650 nm as shown in the following sections. The experiments were carried out under the 0.02 nm resolution of the optical spectrum analyzer (OSA, Yokogawa AQ6370). The measurements of temperature were demonstrated by monitoring the shift that occurs for the transmitted spectrum. The response of the balloon-like fiber structure was observed for different temperature ranges and the influence of the coated sections of an SMF was studied and recorded.

All the results are taken under scientific laboratory conditions (at stable room temperature and humidity). The employment of the safety requirements was committed during the experiments. The structure of chapter three is presented in Fig. (3.1).

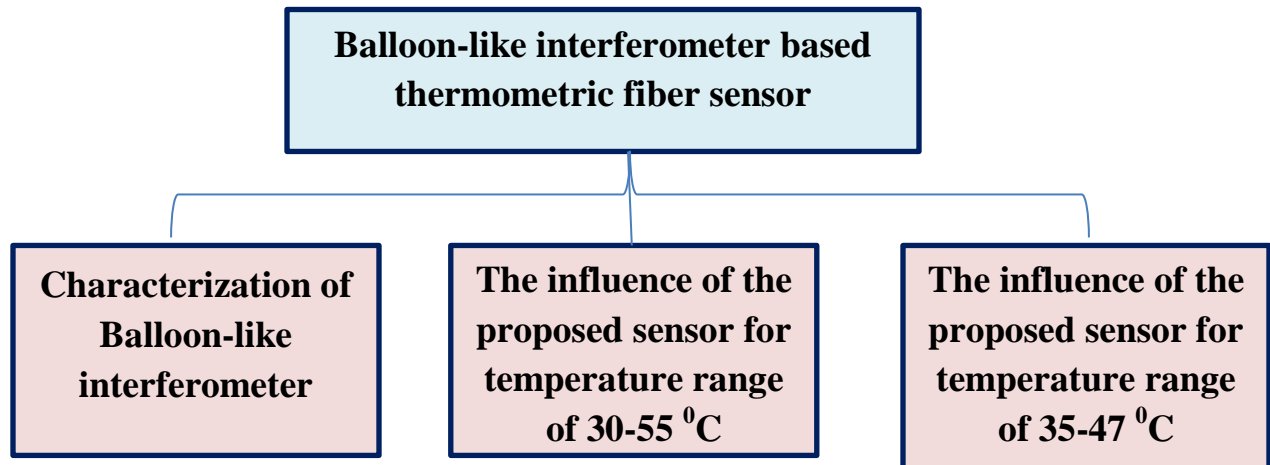


Fig. (3.1): structure of chapter three.

### 3.2. Construction and Characterization of balloon-like SMF Sensor Probe:

SMF with 14 cm was utilized in our experiment. Firstly, the transmission spectrum stability of the broadband source (BBS) through this straight fiber length (Fig. (3.2a)) was checked and recorded directly on OSA to guarantee later accurate measurements, as shown in Fig. (3.3).

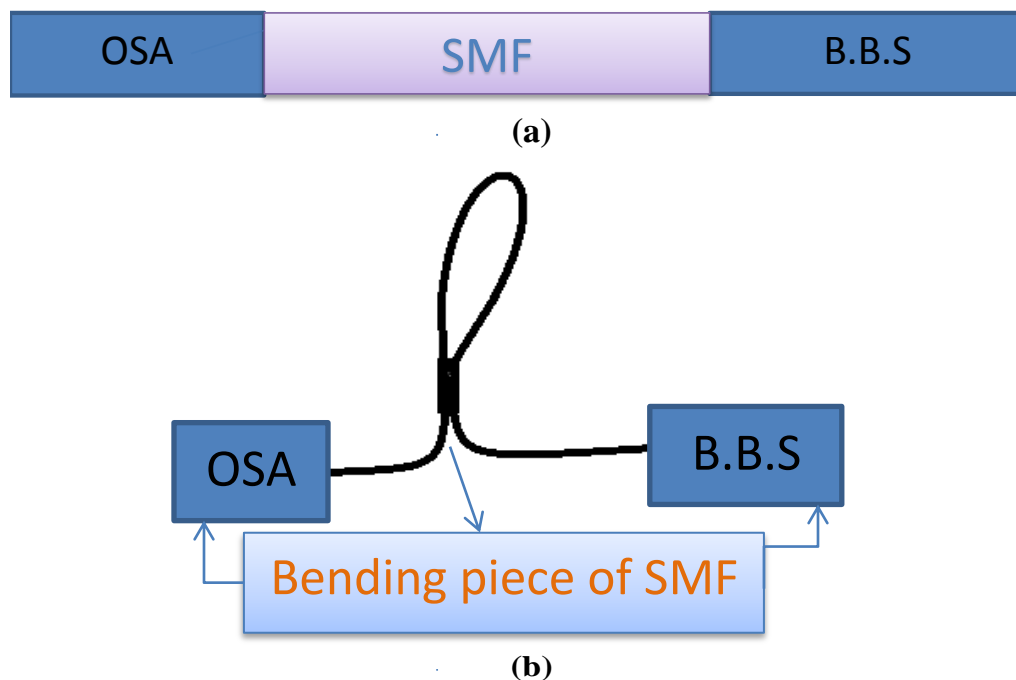


Fig. (3.2): schematic diagram of experimental setup (a) SMF (b) balloon-like.

Then the same fiber was bent with various bending diameters (Fig. (3.2b)) and the transmitted spectrum of these structures was checked using the OSA to study the effect of balloon-like fiber structure. The highest transmission extinction ratio dip obtained was with a 5mm bending radius which is the optimal bent radius. Herein, the assembled fiber sensors based on a segment of 14 cm of SMF and bend with a radius of 5 mm have been used in the present research. Fig. (3.2b) shows the schematic diagram of this experimental setup. BBS was connected to the lead-in of the SMF, while the lead-out of the SMF was coupled to the OSA. Figs (3.3b-c)-(3.4a-c) were carried out with a macro-bending structure. Six structures were studied in this work. Firstly, the protective coating of SMF was stripped-off at the waist of bending with an active sensing length of 1.5 cm, to expose the light field of cladding modes to the natural environment. Then, the balloon-like configuration was assembled utilizing SMF bent configuration based-acrylate polymer coating layer (acrylate polymer is the original protective polymer coating of the SMF is retained). In the next step, the stripped-off SMF encapsulated with PVA thin layer was bent to shape a macro-bent configuration sensor. Finally, SMF encapsulated with three different thicknesses of gold nanoparticles. The extinction ratio of the interference dip of these mentioned structures were of~18.76, 25.344, 24.471, 18.55, 25.947, and 26.699 dB, respectively. These structures at an appropriate radius with 5 mm can be worked as a band-pass filter where some wavelengths were filtered out due to the modal interferometer effect.

Modal interferometer phenomena occurred due to the optical path difference; the modes of SMF core are spitted and then recoupled with cladding modes at the bending segment region. The following sections describe the influence of the balloon-like sensor structure without/with coating in a temperature range of 30-55 °C.

Generally, the bend loss is equivalent to the intensity modulation, which is easily influenced by the light source and the outside environment and consequently limited the sensor resolution. Therefore, as the temperature changes/ increases, then the signal intensity also changes/ decrease. For this response, it can be thought that some modes are wasted away as the fabric of the bent SMF is heated. In this consequent, the assembled sensors also were tested with a limited temperature range between 35-47 °C in the step of 2 °C. This range is very useful in medical and food saving/processing applications.

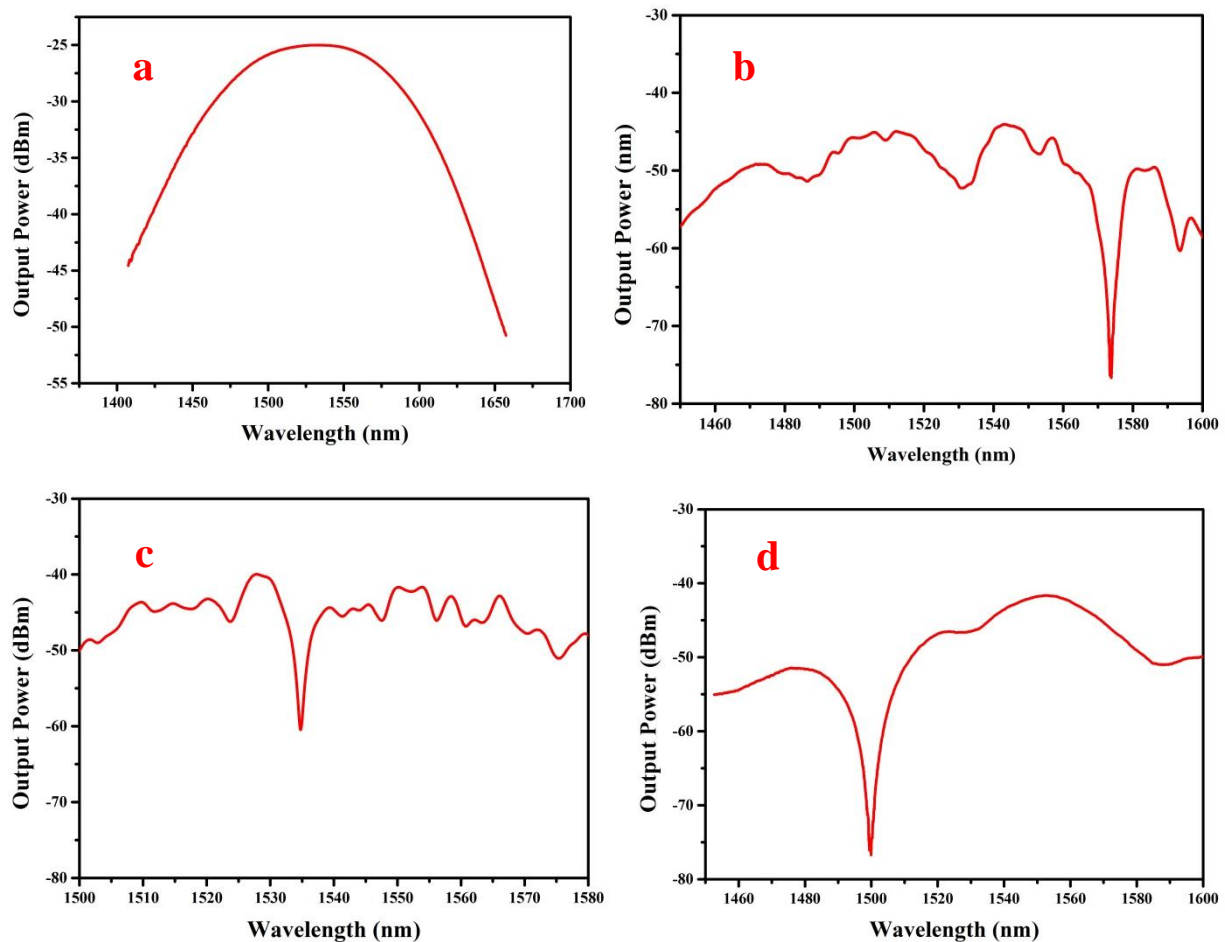


Fig.(3.3): Initial output spectra of: (a) straight SMF, (b) stripped-off SMF, (c) SMF based acrylate polymer coating and, (d) SMF based PVA coating.

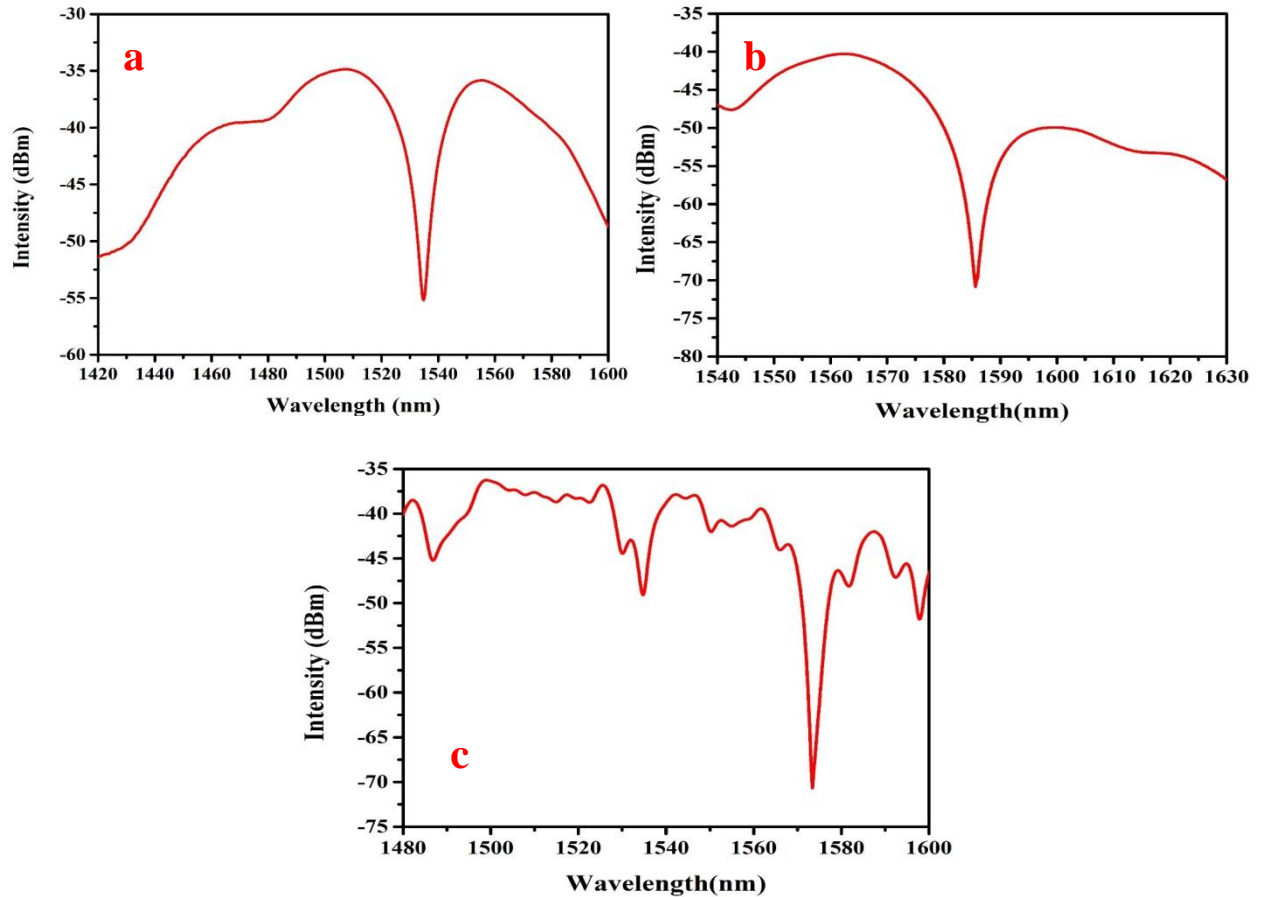


Fig. (3.4): Initial Output Spectra of SMF based GNP coating with a layer thickness of (a) 10 nm, (b) 20 nm, and (c) 30 nm.

### 3.3 The Influence of balloon-like Fiber Based-Stripped-Off Protective Coating on the Temperature Sensitivity:

The balloon-like fiber sensing structure based on stripped-off SMF was first examined. The temperature sensitivity of the assembled fiber sensor was investigated by placing the sensor head of the structure in contact with the surface of the hot plate. The temperature was varied slowly from 30°C to 55°C in steps of 5°C using a temperature-controlled chamber. The transmission spectra response of

the proposed sensor is shown in Fig. (3.5); which the exciting evanescent waves interact with the surrounding temperature and cause the change in the output spectrum. The measured sensitivity is  $-0.7606 \text{ nm}/^{\circ}\text{C}$ . From Fig. (3.5c), the characteristics wavelength shift exhibits a high linear regression coefficient value ( $R^2$ ) of 0.96623. It offers good repeatability in spite of a very small differences between the results for the temperature increasing and decreasing. Also, from Fig (3.5), it can be observed that as the surrounding temperature increases, the dip wavelengths show blue-shift. In order to analyse the repeatability of this sensor, a reverse measurement cycle was carried out in which the temperature was allowed to decrease from  $55^{\circ}\text{C}$  back to  $30^{\circ}\text{C}$ .

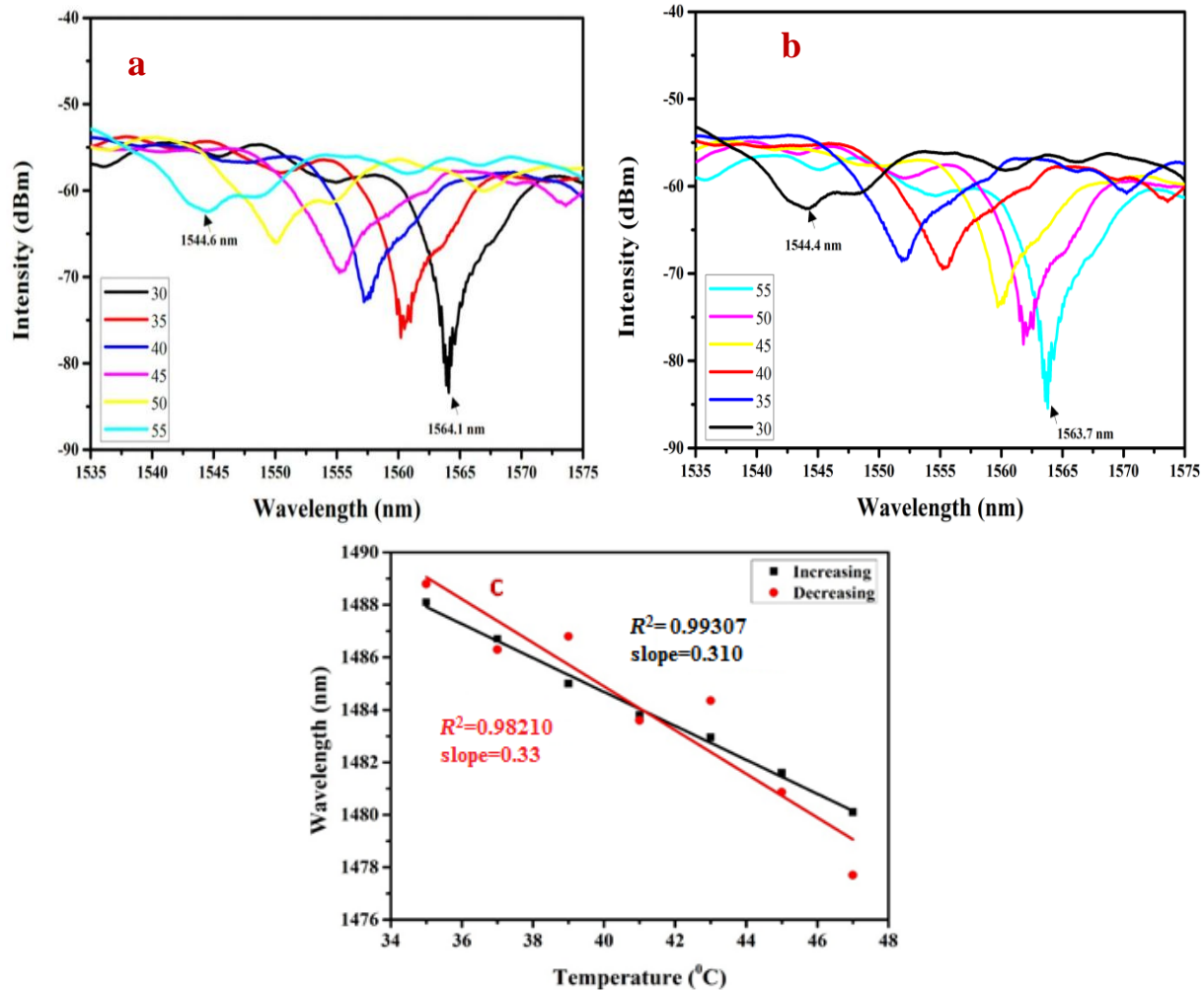


Fig. (3.5): The transmission spectrum response for the balloon-like configuration with stripped-off the original protective polymer coating for temperature change: (a) 30-55 °C, (b) 55-30 °C, and (c) Linear fitting curves of Wavelength shifts versus temperature variation.

Also, the responses of the interferometer against temperature were recorded every 2°C from 35°C to 47°C, and then reversely, as shown in Fig. (3.6). Herein, it can be found that the interferometer possesses a temperature sensitivity of about -0.310nm/°C with a high linear regression coefficient value ( $R^2$ ) is 0.99307. In order

to analyse the repeatability of this sensor, a reverse measurement cycle was carried out in which the temperature was allowed to decrease from 47 °C back to 35 °C.

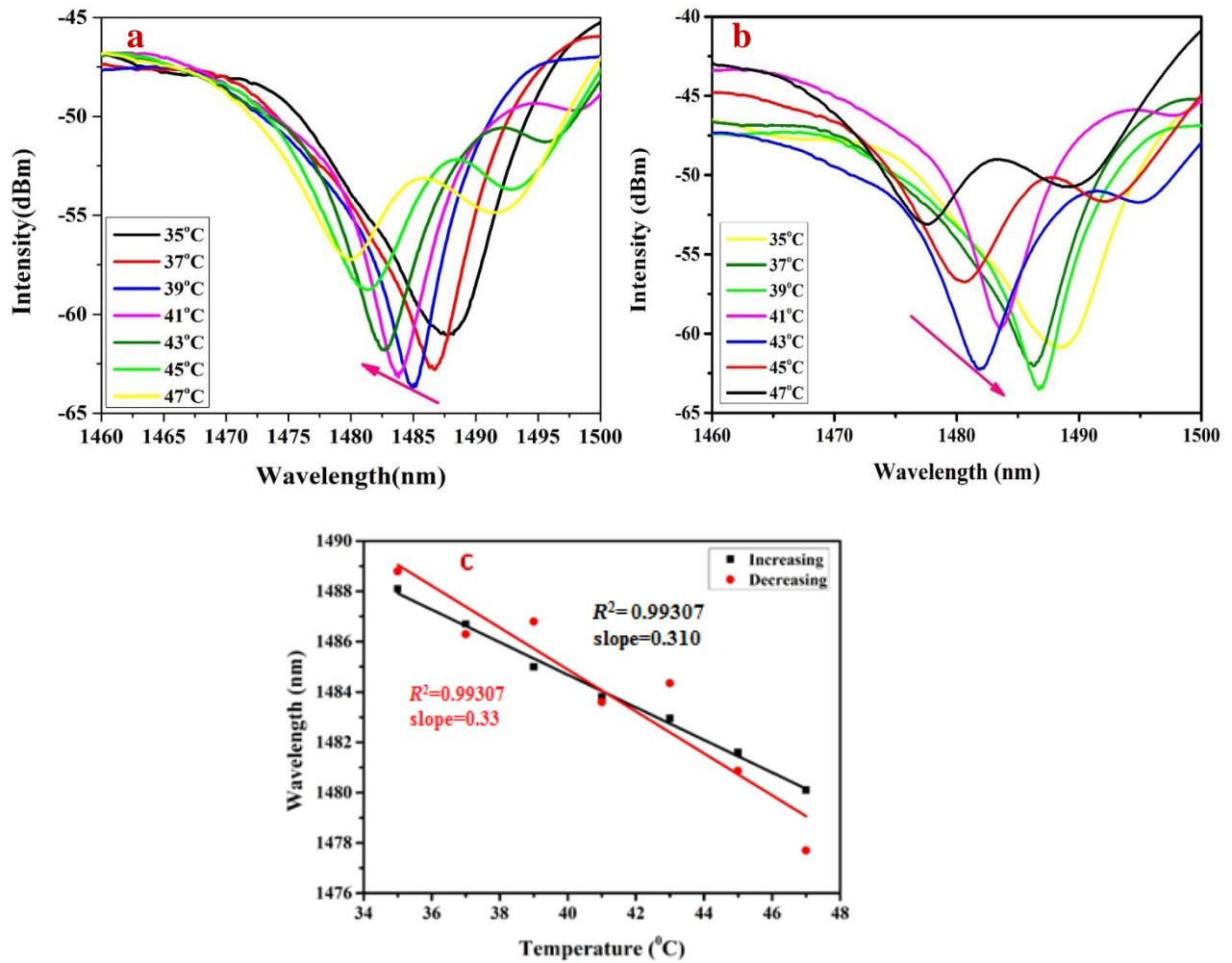


Fig. (3.6): The transmission spectrum response for the balloon-like configuration with stripped-off the original protective polymer coating for temperature change: (a) 35-47 °C, (b) 47-35 °C and (c) linear fitting plots of the shifted dips versus temperature change in the function of wavelengths shift.

### 3.4 The Influence of Polymer Coating on the Sensitivity of balloon-like Fiber Temperature Sensor:

#### 3.4.1 The balloon-like Fiber Sensor Based-Acrylate Polymer:

Another active sensing segment of an SMF with retained original polymer jacket was utilized as a bent structure. This original polymer jacket can improve the resonance, which permits the evanescent field to associate with the outer medium. The transmission spectra response of the proposed sensor is shown in Fig. (3.7); the corresponding dip wavelength exhibits blue-shifts with  $\sim 33.3$  nm as a function of temperature changes. Also, the signal intensities of the output spectra decreased when the surrounding temperature increases. The evaluated sensitivity of the SMF with the polymer jacket retained is  $\sim -1.2857$  nm/°C. This sensor exhibits a good linear regression coefficient ( $R^2$ ) of  $\sim 0.97582$ . In order to analyse the repeatability of this sensor, a reverse measurement cycle was carried out in which the temperature was allowed to decrease from 55 °C back to 30 °C.

Then, the response of the SMF balloon-like sensor with retained the original protective polymer coating in a temperature range between 35°C-47 °C in a step of 2°C was examined. The transmission spectrum evolution was recorded and the result is depicted in Fig. (3.8). The dip wavelength shows a blue shift with the temperature decreasing. The sensor exhibits a sensitivity of  $\sim 0.6339$ nm/°C and a good linear regression coefficient value ( $R^2$ ) is 0.9971. In order to analyse the repeatability of this sensor, a reverse measurement cycle was carried out in which the temperature was allowed to decrease from 47 °C back to 35 °C.

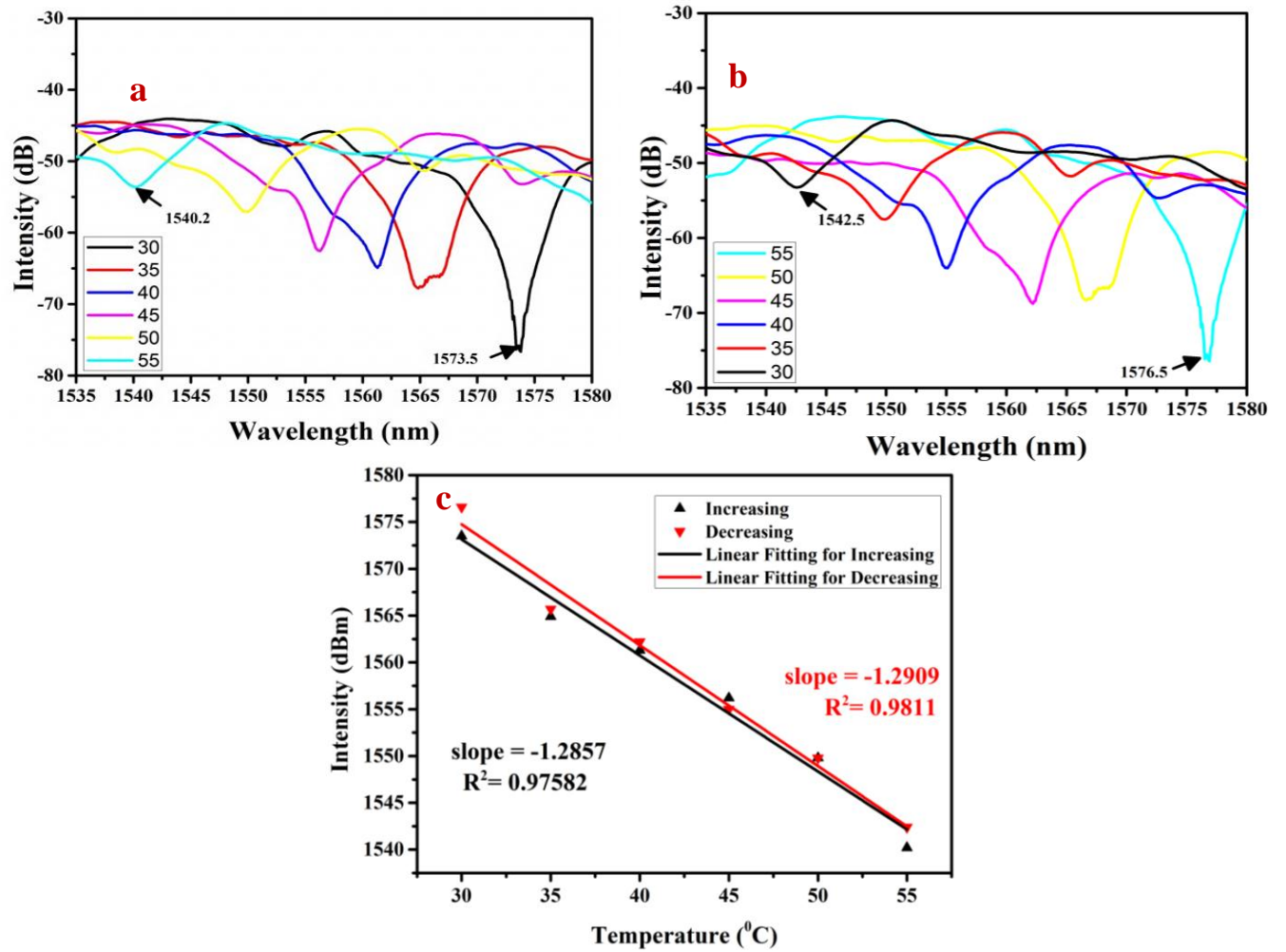


Fig. ( 3.7): The transmission spectrum response for the balloon-like configuration with the original protective polymer coating with temperature change in the range (a) 30-55 °C, (b) 55-30 °C, and (c) Linear fitting curves of Wavelength shifts versus temperature variation.

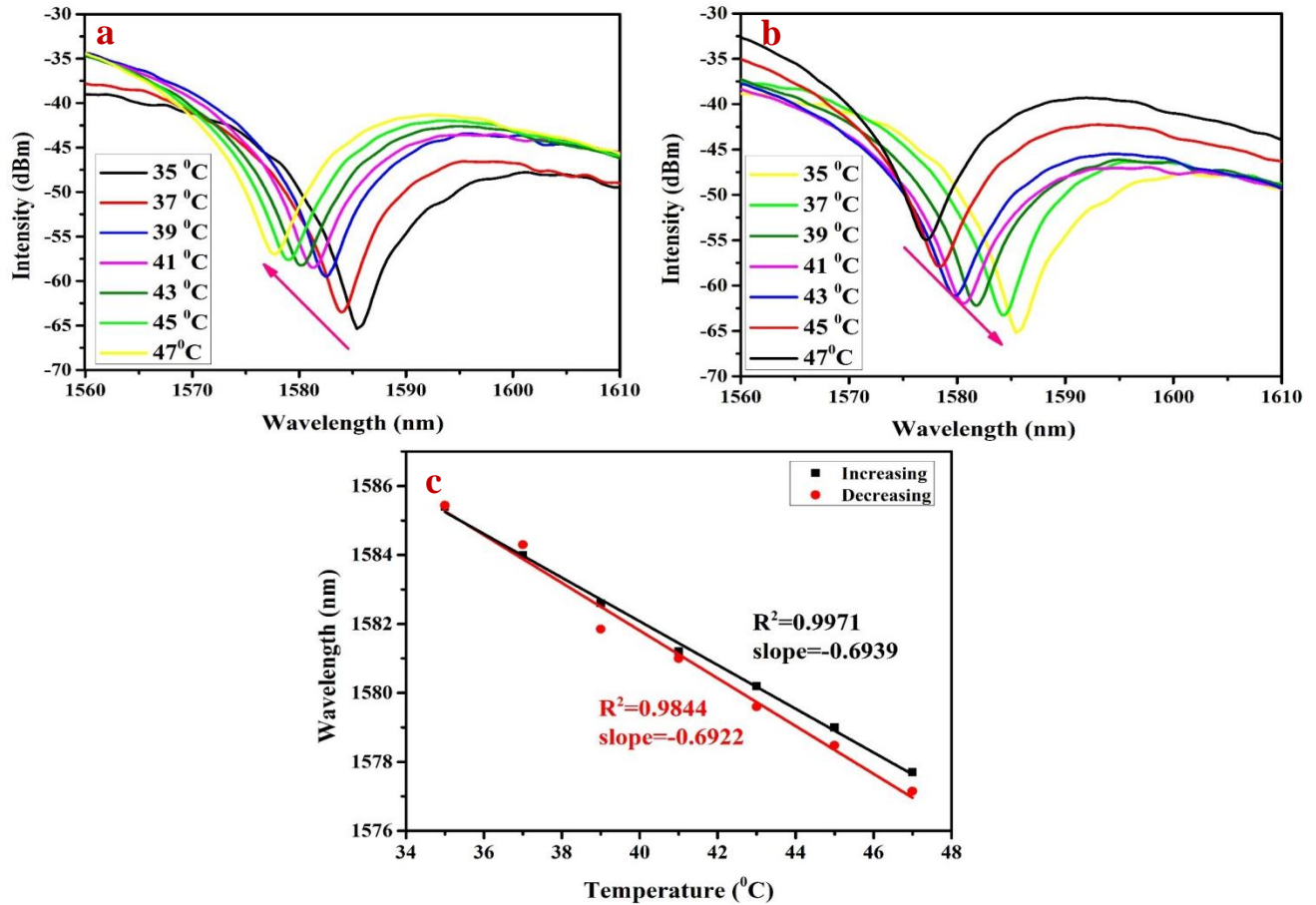


Fig. (3.8): The transmission spectrum response of the balloon-like sensor configuration with the original protective polymer coating as the temperature is changed from (a) 35-47 °C, (b) 47-35 °C, and (c) linear fitting plots of the shifted dips against temperature change in the function of wavelengths shift.

### 3.4.2 The balloon-like Fiber Sensor Based on-PVA-Coating:

To confirm the enhanced temperature sensing performance caused by the polymer coating of optical fibers. The active sensing segment of stripped-off fiber was coated with PVA. The transmission spectrum evolution was recorded and the result is depicted in Fig. (3.9). From this figure, it can be seen that the sensor structure with PVA coating shows the larger wavelength shift (dip wavelength exhibits a blue shift of about 37.3 nm) than that of the acrylate polymer coating

and exhibits good temperature sensitivity of about  $-1.4837 \text{ nm}/^\circ\text{C}$ . This due to that PVA material exhibits a greater thermal conductivity ( $0.28 \text{ W m}^{-1} \text{ K}^{-1}$ ) than the acrylate polymer ( $0.155 \text{ W m}^{-1} \text{ K}^{-1}$ ) [83,84]. Consequently, this leads to a more enhanced temperature transfer from the surrounding environment to the core layer. Furthermore, PVA is highly transparent in the infrared (IR) region and has a TOC that is around two orders of magnitude higher than that of fused silica ( $\sim 10^{-6}$ ) [85]. Fig. (3.9c) presents that the linear regression coefficient value ( $R^2$ ) is 0.9979. These results indicate that the balloon-like sensor based on PVA coating have a good temperature sensing characteristic. In order to analyse the repeatability of this sensor, a reverse measurement cycle was carried out in which the temperature was allowed to decrease from  $55 \text{ }^\circ\text{C}$  back to  $30 \text{ }^\circ\text{C}$ .

Also, the evaluation of the temperature measurement was carried out in a temperature range of  $35\text{-}47 \text{ }^\circ\text{C}$  with a step of  $2^\circ\text{C}$ . Fig. (3.10) shows the transmission spectral response and the linear fitting plots of the shifts in the dips versus temperature for the PVA-coated balloon-like structure. The proposed temperature sensor exhibits good sensitivity of  $\sim -1.60179 \text{ nm}/^\circ\text{C}$  and good linear regression coefficients ( $R^2$ ) of 0.98541.

The occurrence of the blue shift of these proposed sensors might be attributed to the higher RIs of the resonance coating material, as well the RIs of both the cladding and the core of the SMF being reduced owing to the negative TOC, which is of about  $-10^{-4} \text{ K}^{-1}$  [87,88,89].

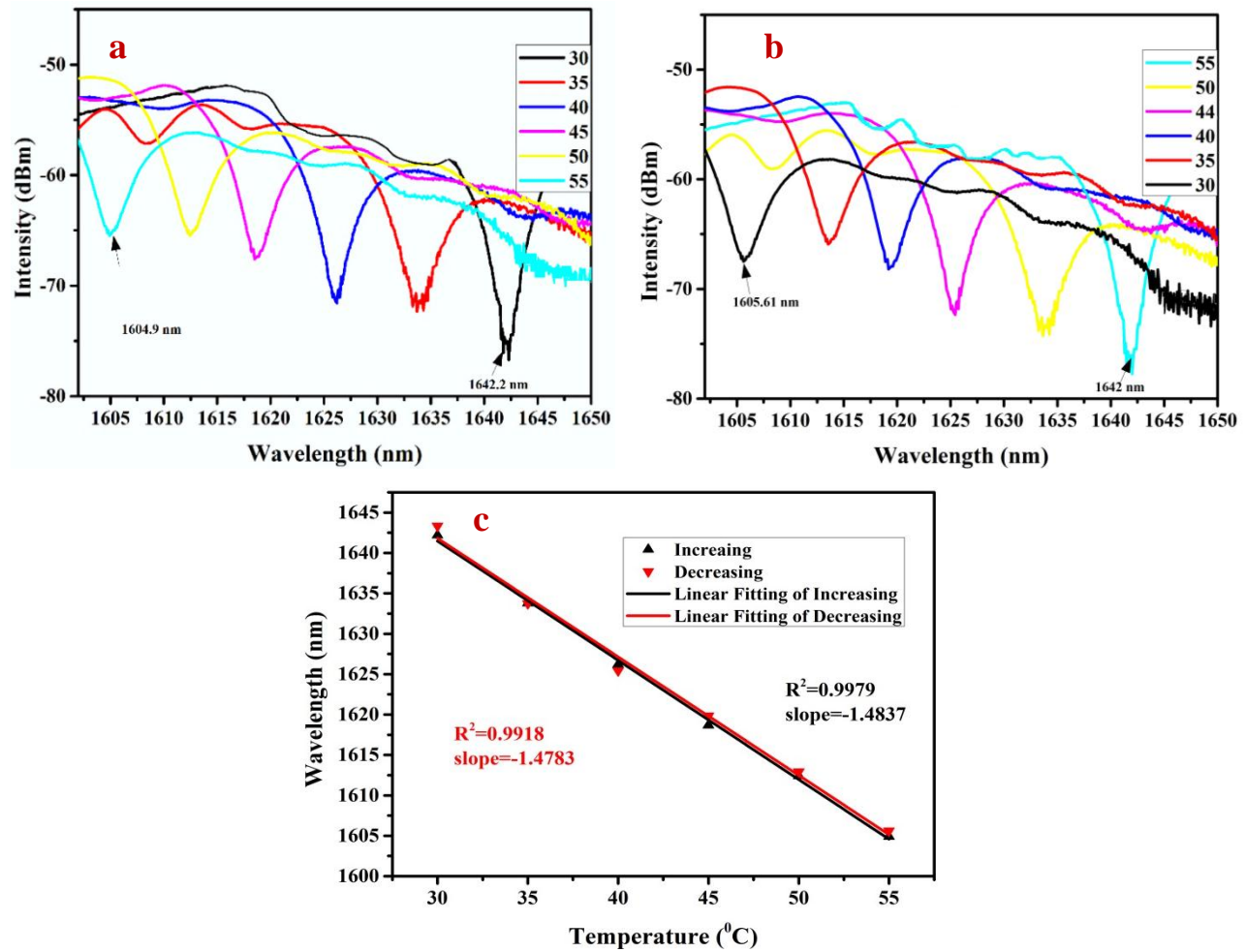


Fig. (3.9): The transmission spectrum response of the balloon-like sensor configuration for PVA-based fiber coating as the temperature is changed from (a) 30-55 °C, (b) 55-30 °C, and (c) Linear fitting plots of the wavelength shift against temperature change.

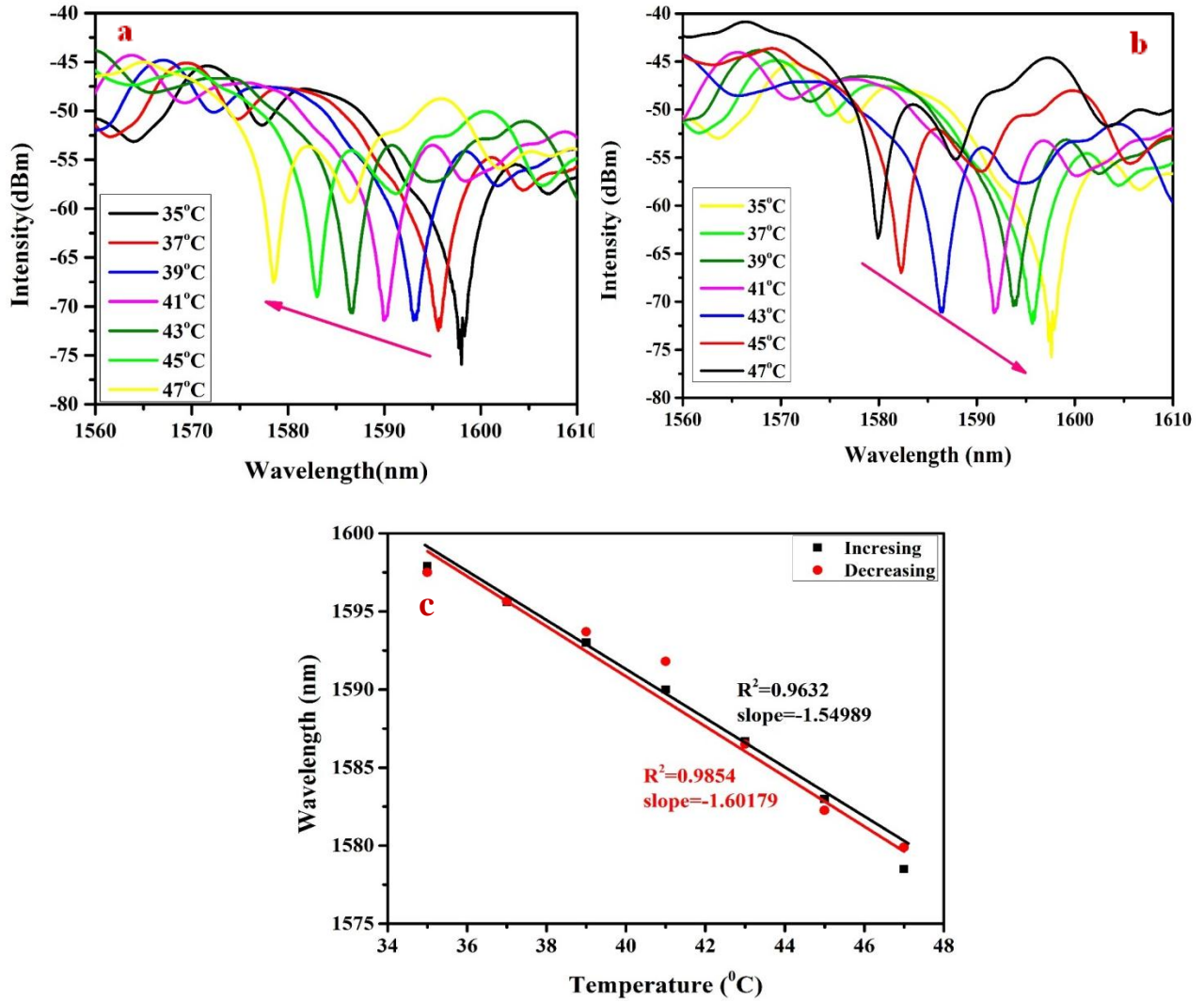


Fig. (3.10): The transmission spectrum response of the balloon-like sensor configuration for PVA-based fiber coating as the temperature is changed from (a) 35-47  $^{\circ}$ C, (b) 47-35  $^{\circ}$ C and (c) linear fitting plots of the shifted dips versus temperature change in the function of wavelengths shift.

### **3.5 The Influence of the gold nanoparticle (GNP)-based fiber coating on the sensitivity of balloon-like fiber Sensor:**

Three different samples of SMF were coated with GNP with thicknesses of 10, 20 and 30 nm over the original protective polymer coating and then their temperature response was examined over a temperature range of 30-55 °C in steps of 5 °C. The transmission spectra evolution was recorded and the results are depicted in Fig. (3.11 a-b), Fig. (3.12 a-b) and Fig. (3.13 a-b), for balloon-like sensor-based 10 nm, 20 nm and 30 nm gold layer thickness, respectively. These configurations show good temperature sensitivity and high linear regression coefficients. In order to analyse the repeatability of this sensor, a reverse measurement cycle was carried out in which the temperature was allowed to decrease from 55 °C back to 30 °C.

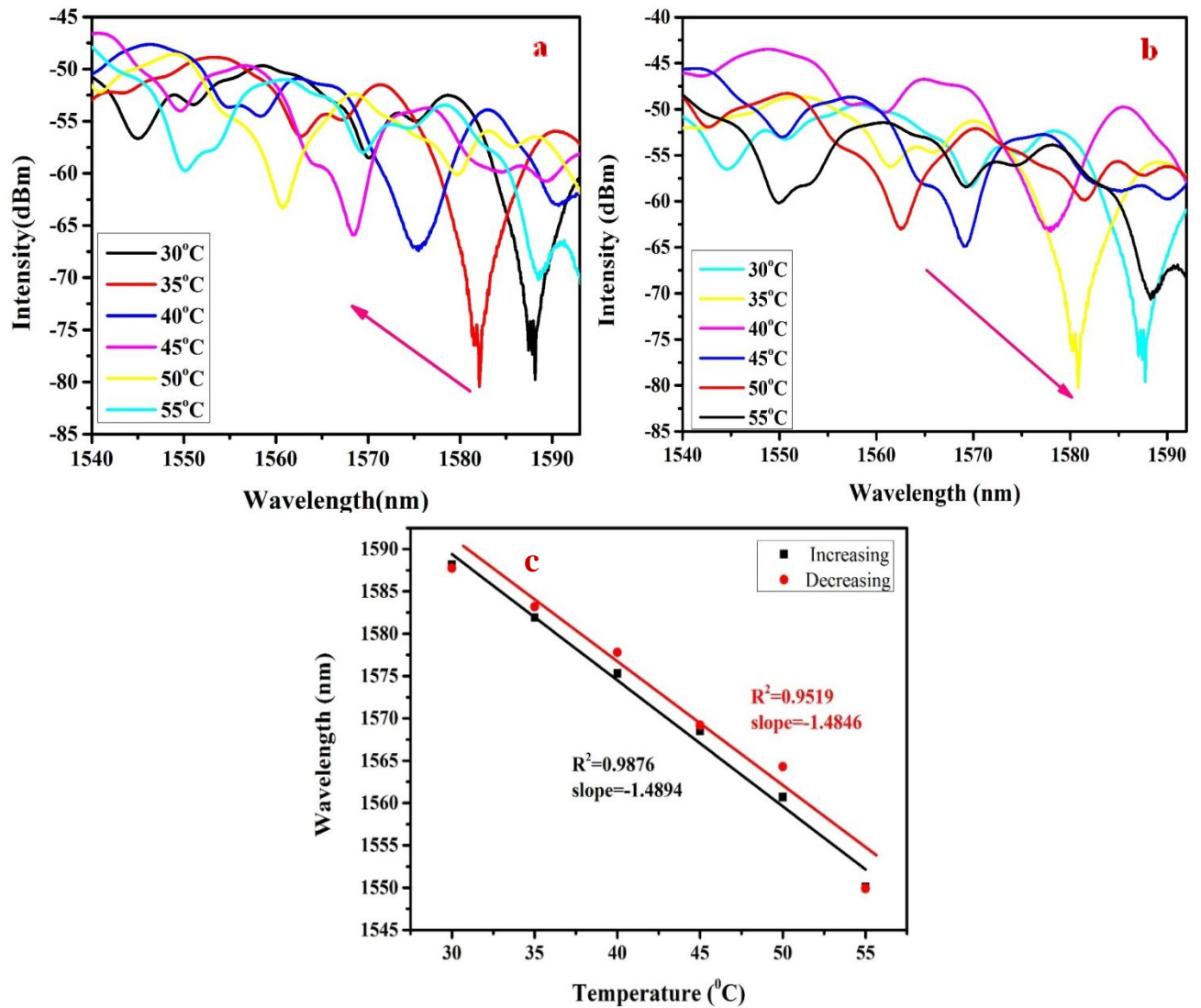


Fig. (3.11): The transmission spectrum response of the balloon-like sensor configuration with 10 nm thickness of the gold coating as the temperature is changed from (a) 30-55 °C, (b) 55-30 °C, and (c) linear fitting plots of the wavelength shift in the dips against temperature change.

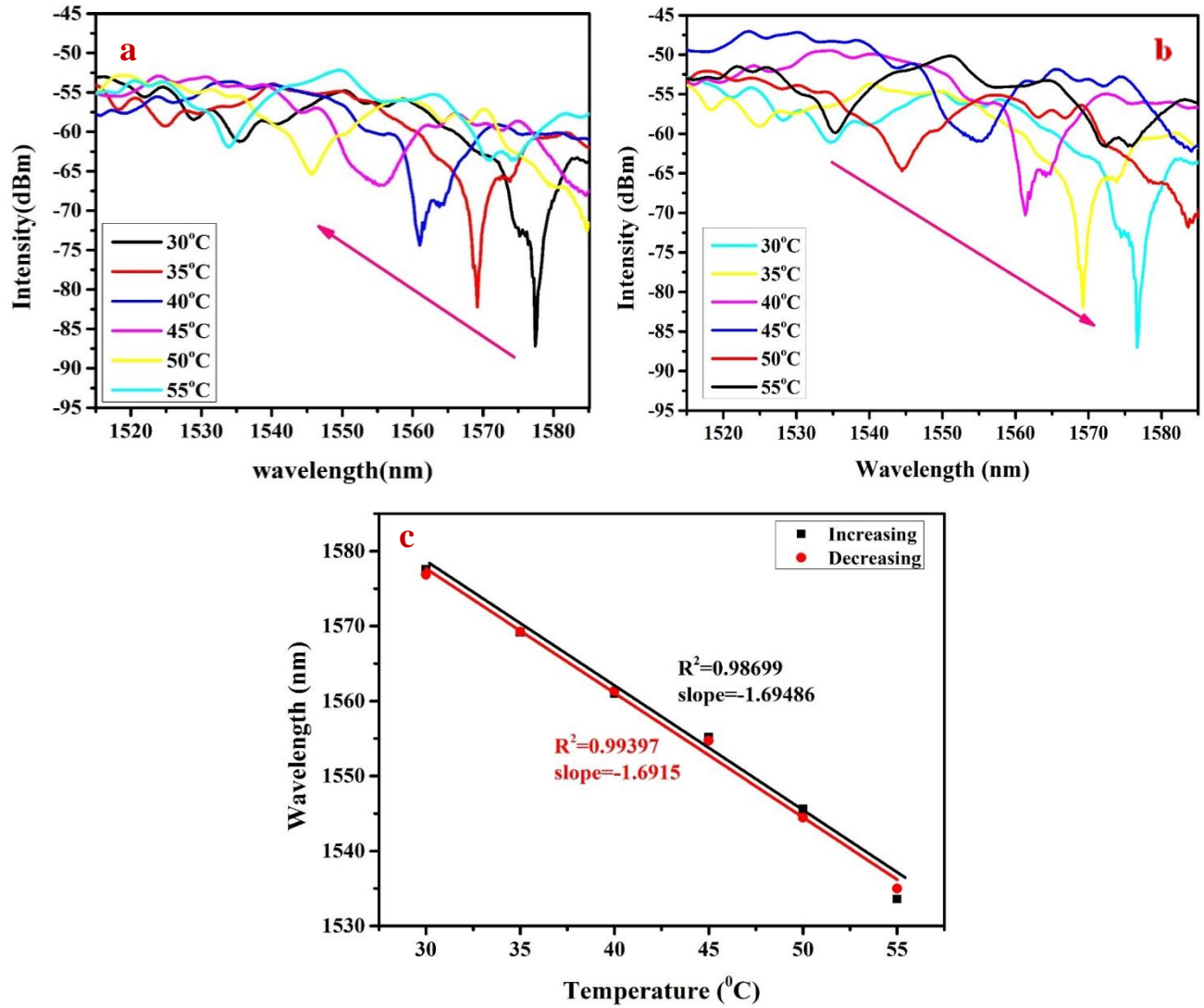


Fig. (3.12): The transmission spectrum response of the balloon-like sensor configuration for 20 nm thickness of the gold coating as the temperature is changed from (a) 30-55 °C, (b) 55-30 °C, and (c) linear fitting plots of the wavelength shift in the dips against temperature change.

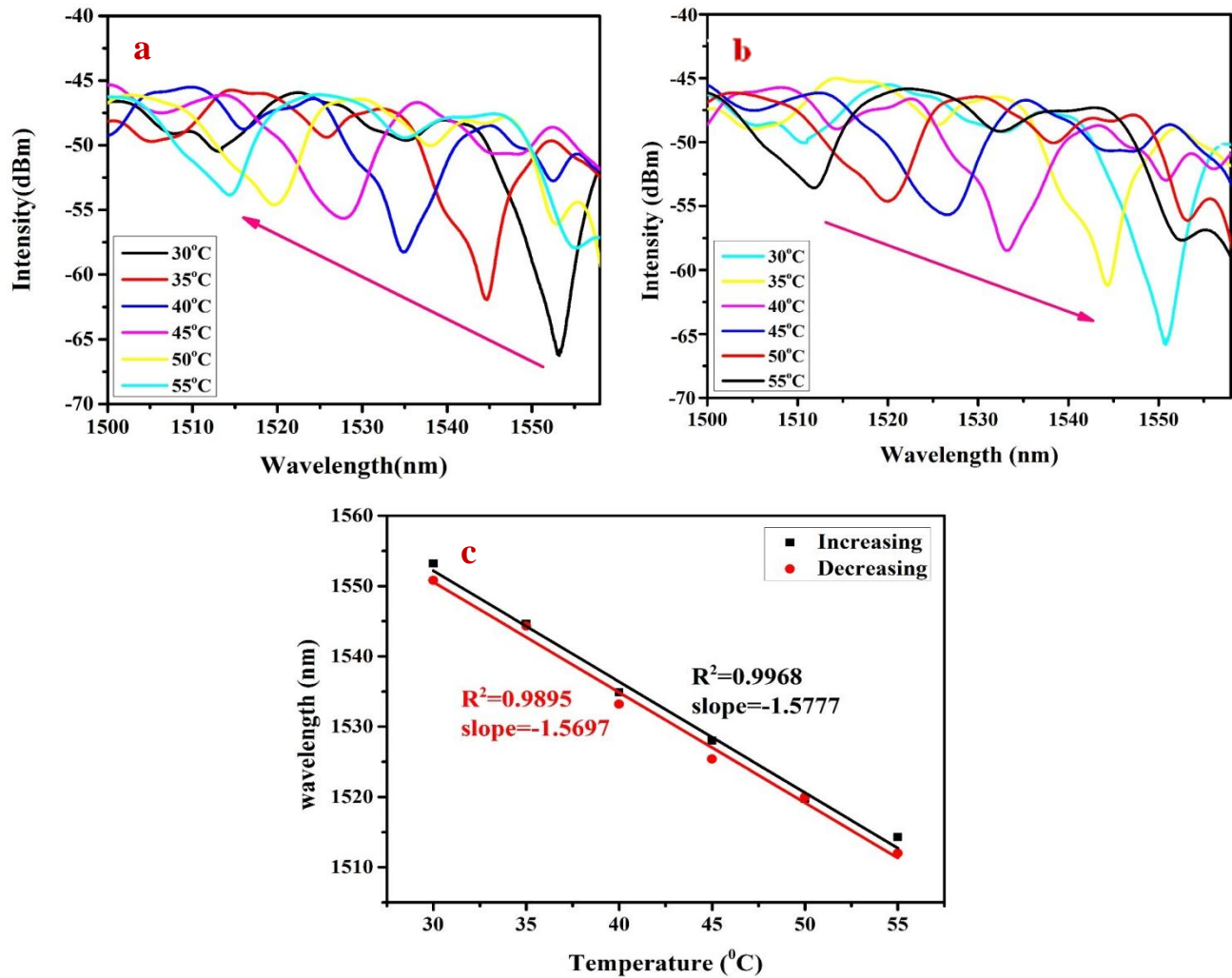


Fig. (3.13): The transmission spectrum response of the balloon-like sensor configuration for 30 nm thickness of the gold coating as the temperature is changed from (a) 30-55 °C, (b) 55-30 °C, and (c) linear fitting plots of the wavelength shift in the dips against temperature change.

From these results, it can be observed that the sensor structure with a thickness of 20 nm shows the larger wavelength shift than the other samples. The results for the different GNP layer thicknesses are given in Table (3.1).

For a comprehensive study of sensing performance, the different fiber sensor structures based on gold coating were examined in a temperature range of 35-47 °C with increasing steps of 2 °C. The transmission spectra evolutions against

temperature variation were recorded and the results are depicted in Fig. (3.17), Fig. (3.18) and Fig. (3.19 ). The temperature sensitivity and linear fitting plot for the different GNP thin layer thicknesses are presented in Table (3.1). The highest temperature sensitivity of the proposed structure was for the SMF coating with GNPs with a thickness of 20 nm, which was  $-2.56 \text{ nm}^\circ\text{C}$ .

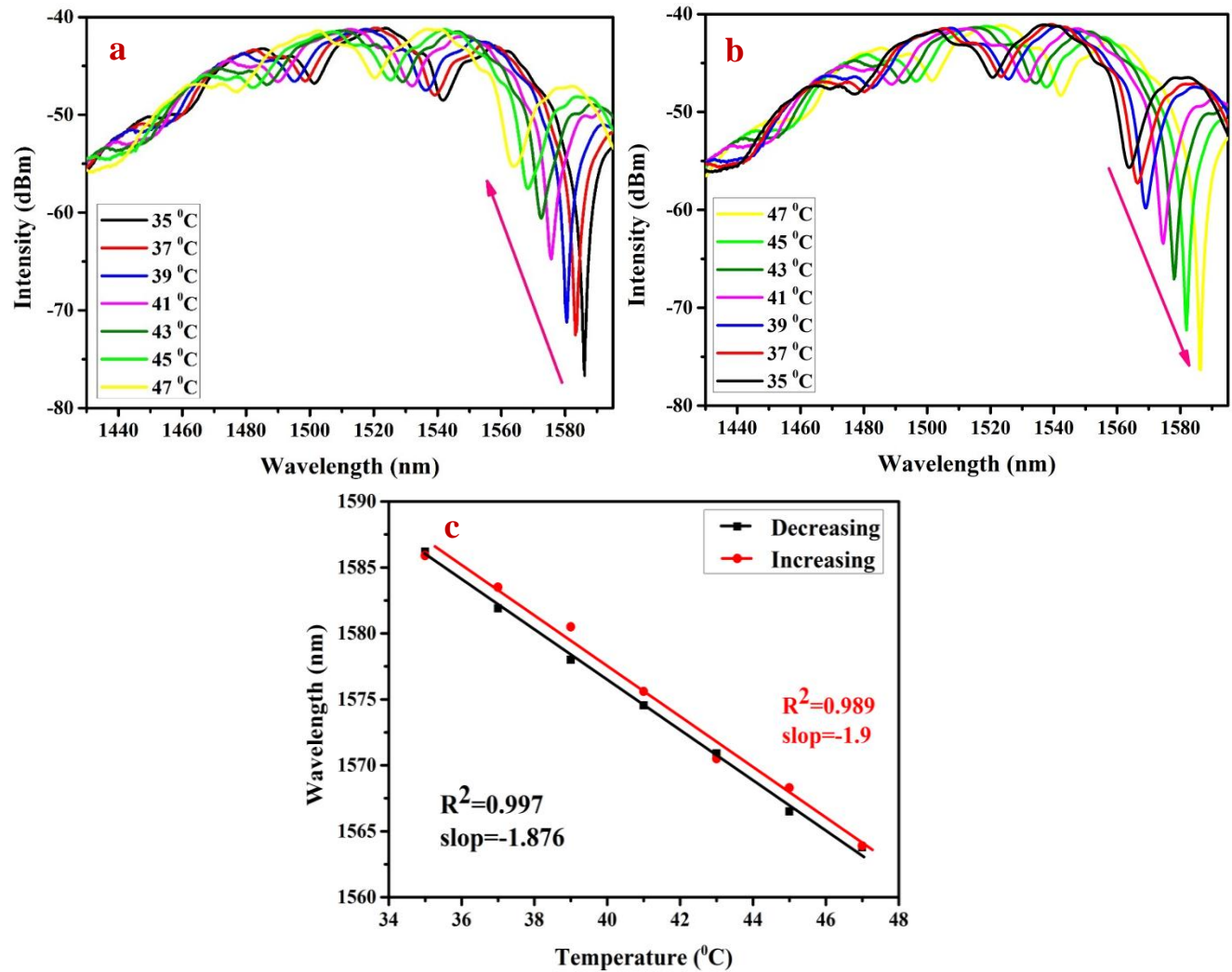


Fig. (3.14): The transmission spectrum response of the balloon-like sensor configuration as the temperature is changed from (a) 35-47°C, (b) 47-35°C for 10 nm thickness of the gold coating, and (c) linear fitting plots of the wavelength shift in the dips against temperature change.

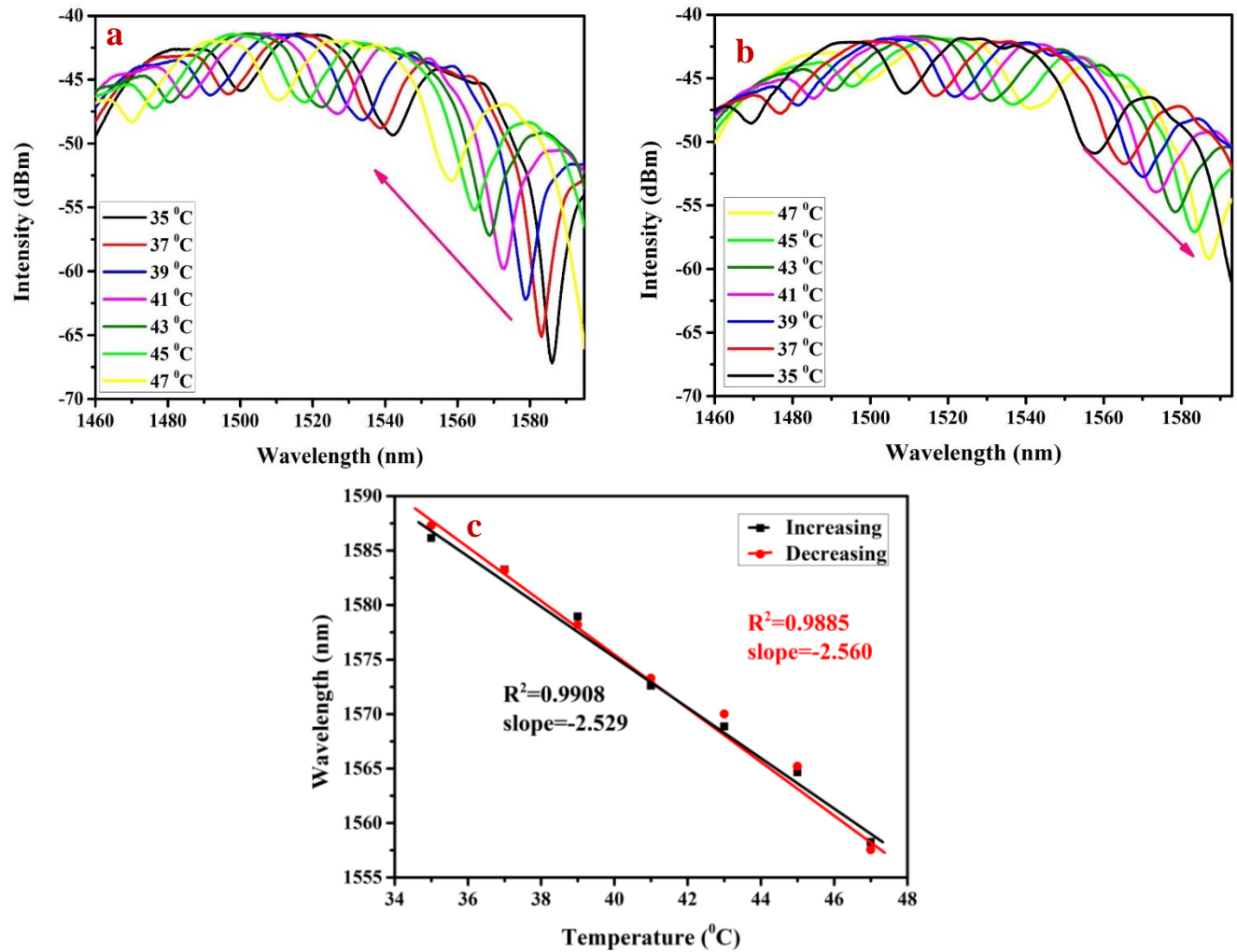


Fig. (3.15): The transmission spectrum response of the balloon-like sensor configuration as the temperature is changed from (a) 35-47°C, (b) 47-35°C for a 20 nm-thick gold coating, and (c) linear fitting plots of the wavelength of the shifted dips versus temperature.

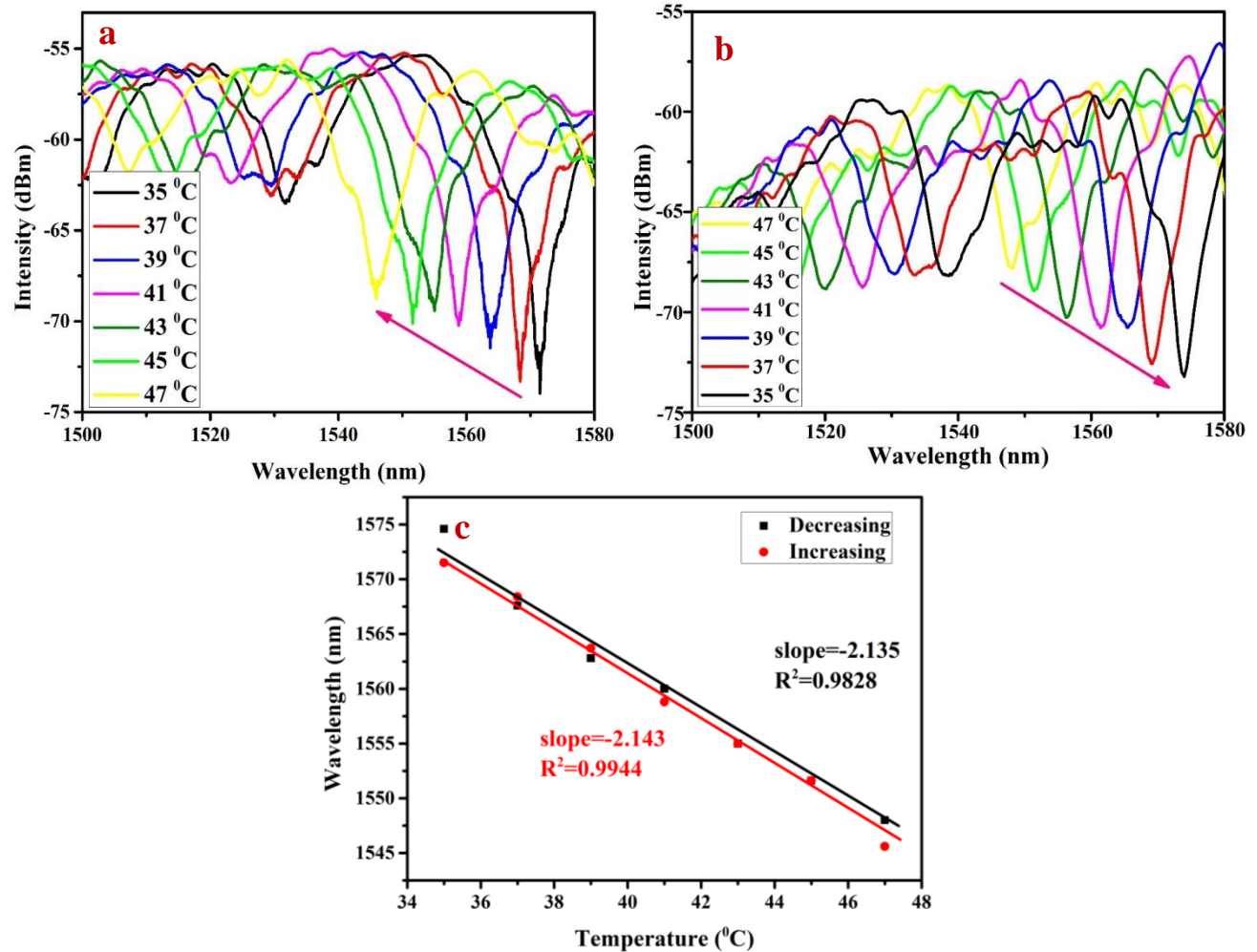


Fig. (3.16): The transmission spectrum response of the balloon-like sensor configuration as the temperature is changed from (a) 35-47°C, (b) 47-35°C for a 30 nm-thick gold coating, and (c) linear fitting plots of the wavelength of the shifted dips versus temperature.

It can observe that the wavelength dip exhibits a blue shift as the surrounding temperature increases. This might be attributed to the higher refractive indices of the resonance coating material. As well the refractive index of gold nanoparticles being reduced owing to the negative TOC, which is of  $\sim -10^{-4} \text{ K}^{-1}$  [95-97].

These results denoted that the temperature sensitivity has been enhanced by encapsulating the balloon-like SMF with the 20 nm GNP thin-layer thickness, where this optimal value maximized the effects of the evanescent fields and

consequently improved sensitivity by more than fourfold. The good thermo-optical coefficient and thermal expansion coefficient of the metallic nanoparticles, including GNP (GNPs have a high intrinsic thermal conductivity of  $\sim 310$  W/(m·K) leading to the remarkable enhancement in sensitivity [34].

Finally, sensitivity and linearity are not the only evaluation criteria. The reversibility is also an important factor of investigation and consideration when evaluating a sensor performance. It can be seen that the resonant dip of the balloon-like structure with GNP coating SMF presents good reversibility for temperature sensing on account of the very small changes in the results between for the temperature increase and decrease cases.

**Table (3.1). Sensor response of different fabricated structures.**

Sensor Structure	Sensitivity (nm/°C) at a temperature range of (30-55)°C	R <sup>2</sup> at a temperature range of (30-55)°C	Sensitivity (nm/°C) at a temperature range of (35-47) °C	R <sup>2</sup> at a temperature range of (35-47)°C
Stripped off SMF	-0.7606	0.96623	-0.310	0.9971
retained original polymer coating	-1.2857	0.97582	0.6473	0.99307
based-PVA coating	-1.4783	0.9918	-1.60179	0.98541
10 nm gold coating	-1.48943	0.98761	-1.876	0.997
20 nm gold coating	-1.6915	0.98699	-2.529	0.9908
30 nm gold coating	-1.5777	0.99206	-2.143	0.9944

### 3.6 The Rise Time and resolution of the temperature Sensor Based on a balloon-like fiber structure:

Rise time is the time needed for the signal to rise from a certain low value 10% to high-level value 90% of the signal maximum. In order to investigate the rise time of all fabricated sensors towards the temperature variation, each sensor was subjected to a sudden and quick change of the temperature. Then, the optical signal was monitored using a photodiode detector (Gentec TPM300CE) connected with a 1GHz oscilloscope (Tektronix MDO3102). Fig. (3.20 a-c) and Fig. (3.21 a-c) show the response characteristics of all fabricated sensors. The estimated rise time is presented in Table (3.2). The rise time of the proposed sensor is considerably ultrafast than that in previously published works [90] . This fast rise time might be attributed due to the high thermal diffusivity of the silica of the SMF, the high thermal conductivity of the gold coating, as well the small size of the sensor head.

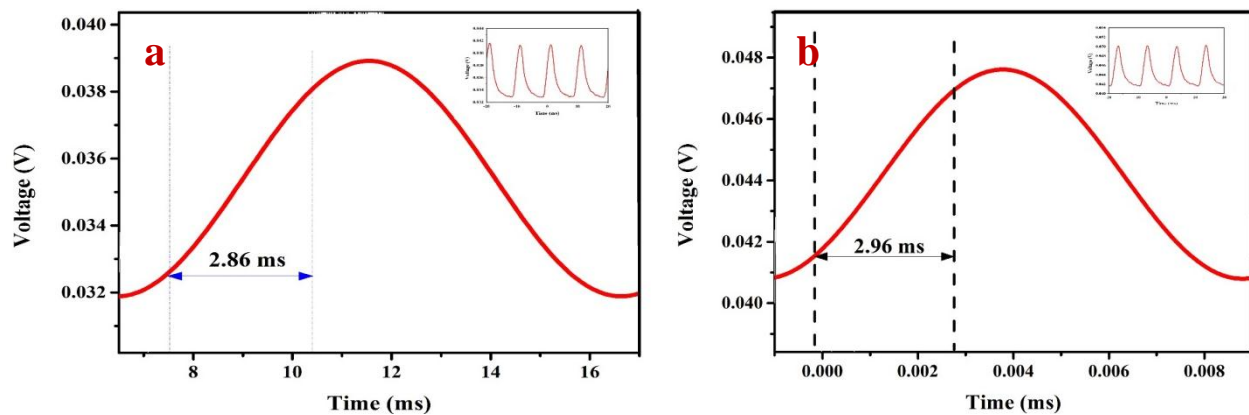


Fig. (3.17): The response time measurement for the SMF with the (a) stripped-off coating and (b) polymer jacket retained.

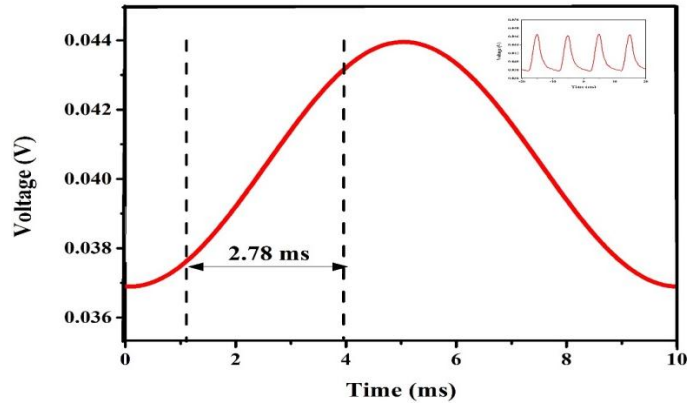


Fig. (3.18): The response time measurement for the polyvinyl alcohol (PVA)-based fiber coating.

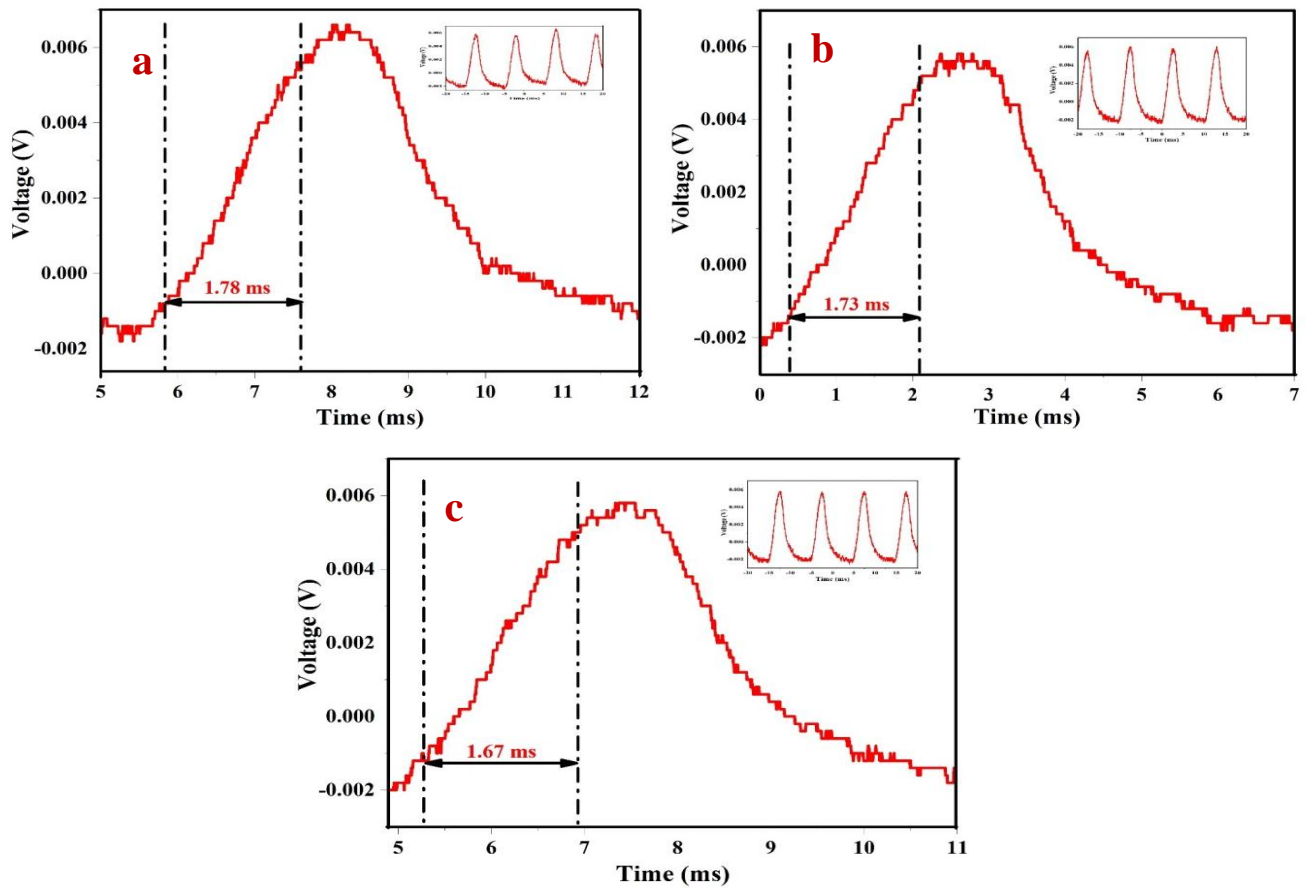


Fig. (3.19): The rise time measurement for the proposed with (a) 10 nm gold coating thickness, (b) 20 nm gold coating thickness, and (c) 30 nm gold coating thickness.

**Table (3.2). Rise time and resolution performance of the different fabricated sensors.**

<b>Sensor Structure</b>	<b>Rise time (ms)</b>	<b>Resolution (°C)</b>
<b>Stripped off SMF</b>	2.96	-
<b>a retained original polymer coating</b>	2.86	-
<b>based-PVA coating</b>	2.78	$3 \times 10^{-4}$
<b>10 nm gold coating</b>	1.78	
<b>20 nm gold coating</b>	1.73	$7.59 \times 10^{-3}$
<b>30 nm gold coating</b>	1.67	

### 3.7 Conclusions:

In this work, an all-fiber optic sensor based on a Mach-Zehnder interferometer for thermometric measurements has been demonstrated experimentally. The sensor structure was formed through bending a standard SMF into a balloon-like shape. The radius of the balloon-like was optimized to 5 mm. A novel structure offering a high-sensitivity temperature sensor based on a balloon-like SMF configuration with a stripped-off, a retained polymer jacket, PVA polymer based-coating fiber and encapsulated with GNP has been fabricated and demonstrated. Interesting techniques for enhancing the sensitivity were carried out

by combining balloon-like configuration with a polymer coating layer and a metallic nanomaterial coating, which allows for an increase in sensor sensitivity by many orders of magnitudes. The influence of the GNP coating thickness in terms of tuning the sensor sensitivity has been studied. The measured sensitivity after the deposition of the GNP upon the active sensing segments was much greater than that of the uncoated fibre by about fourfold. The structure comprised of a bent SMF encapsulated within a 20 nm GNP coating showed the highest sensitivity of about  $-2.65 \text{ nm}/^\circ\text{C}$ . To the best of authors' knowledge, this is the highest sensitivity obtained for such temperature structures. With the benefits of excellent sensitivity, cost-effective manufacture, simple configuration, good measurement repeatability, short response time, and good resolution with suitable biocompatibility, make the designed temperature sensor appropriate for temperature detection in the fields of chemical, molecular, and biological analysis. This fiber temperature sensor exhibits particular promise as a candidate for a precision thermometric device.

### 3.8 Future Work

1. Studying the effect of adding more thickness layers of PVA.
2. Try a different type of polymer coating.
3. Examining the proposed sensor performance with different metal oxide nanoparticles as sensitive material.
4. Using balloon-like MZI based gold coating with fiber laser system as a tunable filter.

## **PUBLICATIONS**

**1. Dunia I Al-Janabi, A. Hadi Al-janabi and Ansam Salman “ HIGH SENSITIVITY BALLOON-LIKE THERMOMETRIC SENSOR BASED ON BENT SINGLE MODE FIBER” Measurement Science and Technology journal , IOP science,19-May-2020 (Accepted)**

**9-Sep-2020 (Published)**

**2. Dunia I Al-Janabi, A. Hadi Al-janabi and Ansam Salman “ ALL FIBRE, HIGHLY SENSITIVE SENSOR BASED ON GOLD NANOPARTICLE-COATED MACRO-BENT SINGLE MODE FIBRE FOR HUMAN TEMPERATURE MONITORING ” Nanophotonics journal**

**22-Oct-2020 (Accepted)**

# *References*

## **References:**

- [1] C. S. PING, "MULTIMODE-INTERFERENCE BASED OPTICAL FIBER SENSOR FOR STRUCTURAL HEALTH MONITORING," uM university (2019).
- [2] S. Wang, R. Lv, Y. Zhao, and J. Qian, "A Mach-Zehnder interferometer-based High Sensitivity Temperature sensor for human body monitoring," *Optical Fiber Technology* **45**, 93–97 (2018).
- [3] I. Garcia, J. Zubia, G. Durana, G. Aldabaldetrekua, M. A. Illarramendi, and J. Villatoro, "Optical fiber sensors for aircraft structural health monitoring," *Sensors* **15**, 15494–15519 (2015).
- [4] P. Mohammadazari, "Application of Capacitive Temperature Sensors for Food Processing Applications," Bachelor of Science A Thesis Submitted in Partial Fulfillment of the Requirements for the Degree of Master of Science in the field of Mechanical Engin (2018).
- [5] P. Wolkoff, "Indoor air humidity, air quality, and health – An overview," *International Journal of Hygiene and Environmental Health* **221**, 376–390 (2018).
- [6] M. Wang, A. Jiang, L. Gong, L. Luo, W. Guo, C. Li, J. Zheng, C. Li, B. Yang, and J. Zeng, "Temperature significant change COVID-19 Transmission in 429 cities," medRxiv (2020).
- [7] D. Zhang, J. Wang, Y. Wang, and X. Dai, "A fast response temperature sensor based on fiber Bragg grating," *Measurement Science and Technology* **25**, 75105 (2014).
- [8] D. Niu, D. Zhang, L. Wang, T. Lian, M. Jiang, X. Sun, Z. Li, and X. Wang, "High-resolution and fast-response optical waveguide temperature sensor using asymmetric Mach-Zehnder interferometer structure," *Sensors and Actuators A: Physical* **299**, 111615 (2019).

- [9] Y. Bao, Y. Huang, M. S. Hoehler, and G. Chen, "Review of fiber optic sensors for structural fire engineering," *Sensors* **19**, 877(2019).
- [10] E. Schena, D. Tosi, P. Saccomandi, E. Lewis, and T. Kim, "Fiber optic sensors for temperature monitoring during thermal treatments: an overview," *Sensors* **16**, 1144 (2016).
- [11] J. M. Lopez-Higuera, L. R. Cobo, A. Q. Incera, and A. Cobo, "Fiber optic sensors in structural health monitoring," *Journal of lightwave technology* **29**, 587–608 (2011).
- [12] D. Kowal, W. Urbanczyk, and P. Mergo, "Twin-Core Fiber-Based Mach Zehnder Interferometer for Simultaneous Measurement of Strain and Temperature," *Sensors* **18**, 915 (2018).
- [13] Q. Yao, H. Meng, W. Wang, H. Xue, R. Xiong, B. Huang, C. Tan, and X. Huang, "Simultaneous measurement of refractive index and temperature based on a core-offset Mach–Zehnder interferometer combined with a fiber Bragg grating," *Sensors and Actuators A: Physical* **209**, 73–77 (2014).
- [14] F. Urban, J. Kadlec, R. Vlach, and R. Kuchta, "Design of a pressure sensor based on optical fiber Bragg grating lateral deformation," *Sensors* **10**, 11212–11225 (2010).
- [15] E. Udd and W. B. Spillman Jr, *Fiber Optic Sensors: An Introduction for Engineers and Scientists* (John Wiley & Sons, 2011).
- [16] L. Li, D. Zhang, X. Wen, and S. Peng, "FFPI-FBG hybrid sensor to measure the thermal expansion and thermo-optical coefficient of a silica-based fiber at cryogenic temperatures," *Chinese Optics Letters* **13**, 100601 (2015).
- [17] L. Xu, L. Jiang, S. Wang, B. Li, and Y. Lu, "High-temperature sensor based on an abrupt-taper Michelson interferometer in single mode fiber," *Applied Optics* **52**, 2038–2041 (2013).
- [18] X. Dong, H. Y. Tam, and P. Shum, "Temperature-insensitive strain

sensor with polarization-maintaining photonic crystal fiber based Sagnac interferometer," *Applied Physics Letters* **90**, 151113 (2007).

[19] Y. Lu, C. Shen, C. Zhong, D. Chen, X. Dong, and J. Cai, "Refractive index and temperature sensor based on double-pass MZ interferometer with an FBG," *IEEE Photonics Technology Letters* **26**, 1124–1127 (2014).

[20] W. A. Khaleel and A. H. M. Al-Janabi, "High-sensitivity sucrose erbium-doped fiber ring laser sensor," *Optical Engineering* **56**, 1–7 (2017).

[21] Y. Qian, Y. Zhao, Q. Wu, and Y. Yang, "Review of salinity measurement technology based on optical fiber sensor," *Sensors and Actuators B: Chemical* **260**, 86–105 (2018).

[22] Y. Zhao, Q. Wu, and Y. Zhang, "Theoretical analysis of high sensitive seawater temperature and salinity measurement based on C-type micro-structured fiber," *Sensors and Actuators B: Chemical* **258**, 822–828 (2018).

[23] Y. Geng, X. Li, X. Tan, Y. Deng, and X. Hong, "Compact and ultrasensitive temperature sensor with a fully liquid-filled photonic crystal fiber Mach–Zehnder interferometer," *IEEE Sensors Journal* **14**, 167–170 (2013).

[24] S. K. Abi Kaed Bey, T. Sun, and K. T. V Grattan, "Optimization of a long-period grating-based Mach–Zehnder interferometer for temperature measurement," *Optics Communications* **272**, 15–21 (2007).

[25] P. Lu, L. Men, K. Sooley, and Q. Chen, "Tapered fiber Mach–Zehnder interferometer for simultaneous measurement of refractive index and temperature," *Applied Physics Letters* **94**, 131110 (2009).

[26] X. Zeng, Y. Wu, C. Hou, J. Bai, and G. Yang, "A temperature sensor based on optical microfiber knot resonator," *Optics Communications* **282**, 3817–3819 (2009).

- [27] J. E. Antonio-Lopez, Z. S. Eznaveh, P. LiKamWa, A. Schulzgen, and R. Amezcua-Correa, "Multicore fiber sensor for hightemperature applications up to 1000°C," *Optics Letters* **39**,4309–4312 (2014).
- [28] K. Tian, G. Farrell, E. Lewis, X. Wang, H. Liang, and P. Wang, "A high sensitivity temperature sensor based on balloon-shaped bent SMF structure with its original polymer coating," *Measurement Science and Technology* **29**, 85104 (2018).
- [29] M. Y. M. Noor, A. I. Azmi, A. S. Abdullah, A. S. M. Supa'at, N.M. Kassim, M. H. Ibrahim, and N. H. Ngajikin, "High Sensitivity of Balloon-Like Bent MMI Fiber Low-Temperature Sensor," *IEEE Photonics Technology Letters* **27**, 1989–1992 (2015).
- [30] T. Liu, Y. Chen, Q. Han, F. Liu, and Y. Yao, "Sensor based on macrobent fiber Bragg grating structure for simultaneous measurement of refractive index and temperature," *Applied Optics* **55**, 791–795 (2016).
- [31] D. I. A.-J. and A. S. and A. H. Al-Janabi, "High sensitivity balloonlike thermometric sensor based on bent single mode fiber," *Measurement Science and Technology* (2020).
- [32] X. Liu, Y. Zhao, R. Lv, and Q. Wang, "High Sensitivity Balloon-Like Interferometer for Refractive Index and Temperature Measurement," *IEEE Photonics Technology Letters* **28**, 1485–1488 (2016).
- [33] Y. Wang, A. Liu, Y. Han, and T. Li, "Sensors based on conductive polymers and their composites: a review," *Polymer International* **n/a**, (2019).
- [34] S. Yu, H. Zhang, C. Chen, J. Zhang, and P. Li, "Preparation and mechanism investigation of highly sensitive humidity sensor based on two-dimensional porous Gold/Graphite carbon nitride nanoflake," *Sensors and Actuators B: Chemical* **307**, 127679(2020).
- [35] J. Senior, *Optical Fiber Communications* (n.d.).

- [36] G. P. Agrawal, *Fiber-Optic Communication Systems* (John Wiley & Sons, 2012), Vol. 222.
- [37] K. Fidanboylyu, "Fiber optic sensors and their applications," (2015).
38. S. Kwan, "Principles of optical fibers," Partial Fulfillment of Course Requirement for MatE **115**, (2002).
- [39] L. C. L. Chin, W. M. Whelan, and I. A. Vitkin, "Optical fiber sensors for biomedical applications," in *Optical-Thermal Response of Laser-Irradiated Tissue* (Springer, 2010), pp. 661–712.
- [40] N. H. Yusof, H. A. Razak, H. Arof, and S. W. Harun, "Performance comparison of high temperature sensor based on non-adiabatic silica microfiber and single mode-multimode-single mode fiber structure," *Microwave and Optical Technology Letters* **61**, 431–435 (2019).
- [41] G. Leo, N. Aeby, and D. Inaudi, "Medical apparatus system having optical fiber load sensing capability," (2011).
- [42] A. D. Kersey, "Optical fiber sensors for permanent downwell monitoring applications in the oil and gas industry," *IEICE transactions on electronics* **83**, 400–404 (2000).
- [43] Y. Zhao, X. Li, X. Zhou, and Y. Zhang, "Review on the grapheme based optical fiber chemical and biological sensors," *Sensors and Actuators B: Chemical* **231**, 324–340 (2016).
- [44] O. S. Wolfbeis, "Fluorescence optical sensors in analytical chemistry," *TrAC Trends in Analytical Chemistry* **4**, 184–188 (1985).
- [45] H. Alsweefe, S. K. Al-Hayali, and A. H. M. Al-Janabi, "Efficient humidity sensor based on an etched no-core fiber coated with copper oxide nanoparticles," *Journal of Nanophotonics* **12**, 1–12(2018).
- [46] E. Pinet, "Fabry-Perot fiber-optic sensors for physical parameters measurement in challenging conditions," *Journal of sensors* **2009**,(2009).

- [47] H. S. Efendioglu, T. Yildirim, and K. Fidanboyly, "Prediction of force measurements of a microbend sensor based on an artificial neural network," *Sensors* **9**, 7167–7176 (2009).
- [48] S. Series, *OPTICAL FIBER SENSOR TECHNOLOGY Volume2* (n.d.), Vol. 2.
- [49] S. S. Chong, A. R. Aziz, and S. W. Harun, "Fibre optic sensors for selected wastewater characteristics," *Sensors* **13**, 8640–8668 (2013).
- [50] A. R. Bahrapour, S. Tofighi, M. Bathaee, and F. Farman, "Optical fiber interferometers and their applications," *Interferometry- Research and Applications in Science and Technology* **1**, 3–30(2012).
- [51] Y. Wu, S. Xiao, Y. Xu, Y. Shen, Y. Jiang, W. Jin, Y. Yang, and S.Jian, "Highly sensitive force sensor based on balloon-like interferometer," *Optics & Laser Technology* **103**, 17–21 (2018).
- [52] L. Zhao, B. Liu, Y. Wu, T. Sun, Y. Mao, and T. Nan, "Measurement of refractive index and temperature using balloonshaped Mach-Zehnder interferometer," *Optik* **188**, 115–119 (2019).
- [53] K. Tian, G. Farrell, X. Wang, E. Lewis, and P. Wang, "Highly sensitive displacement sensor based on composite interference established within a balloon-shaped bent multimode fiber structure," *Applied Optics* **57**, 9662–9668 (2018).
- [54] Saif A. Mohammed and Abdul H. Al-Janabi, "All Fiber Chemical Liquids Refractive Index Sensor Based on Multimode Interference," **17**, 33–39 (2018).
- [55] B. H. Lee, Y. H. Kim, K. S. Park, J. B. Eom, M. J. Kim, B. S. Rho, and H. Y. Choi, "Interferometric fiber optic sensors," *sensors* **12**, 2467–2486 (2012).
- [56] D. Pawar, C. N. Rao, R. K. Choubey, and S. N. Kale, "Mach-Zehnder interferometric photonic crystal fiber for low acoustic frequency detections," *Applied Physics Letters* **108**, 41912 (2016).

- [57] J. S. Sirkis, D. D. Brennan, M. A. Putman, T. A. Berkoff, A. D. Kersey, and E. J. Friebele, "In-line fiber etalon for strain measurement," *Optics letters* **18**, 1973–1975 (1993).
- [58] F. L. Pedrotti, L. S. Pedrotti, and L. M. Pedrotti, "Introduction to Optics: Pearson International Edition," (2007).
- [59] W.-H. Tsai and C.-J. Lin, "A novel structure for the intrinsic Fabry-Perot fiber-optic temperature sensor," *Journal of Lightwave Technology* **19**, 682–686 (2001).
- [60] S.-H. Kim, J.-J. Lee, D.-C. Lee, and I.-B. Kwon, "A study on the development of transmission-type extrinsic Fabry-Perot interferometric optical fiber sensor," *Journal of lightwave technology* **17**, 1869–1874 (1999).
- [61] M. E. Franke, T. J. Koplín, and U. Simon, "reviews Metal and Metal Oxide Nanoparticles in Chemiresistors : Does the Nanoscale Matter ?," 36–50 (n.d.).
- [62] C. W. Hollars and R. C. Dunn, "Evaluation of thermal evaporation conditions used in coating aluminum on near-field fiber-optic probes," *Review of scientific instruments* **69**, 1747–1752 (1998).
- [63] M. Islam, M. M. Ali, M.-H. Lai, K.-S. Lim, and H. Ahmad, "Chronology of Fabry-Perot interferometer fiber-optic sensors and their applications: a review," *Sensors* **14**, 7451–7488 (2014).
- [64] X. Wan and H. F. Taylor, "Intrinsic fiber Fabry-Perot temperature sensor with fiber Bragg grating mirrors," *Optics letters* **27**, 1388–1390 (2002).
- [65] Z. Wang, F. Shen, L. Song, X. Wang, and A. Wang, "Multiplexed fiber Fabry-Perot interferometer sensors based on ultrashort Bragg gratings," *IEEE Photonics Technology Letters* **19**, 622–624 (2007).
- [66] Z. Ran, Y. Rao, J. Zhang, Z. Liu, and B. Xu, "A miniature fiberoptic refractive-index sensor based on laser-machined Fabry-Perot interferometer tip," *Journal of Lightwave Technology* **27**, 5426–5429 (2009).

- [67] T. Wei, Y. Han, H.-L. Tsai, and H. Xiao, "Miniaturized fiber inline Fabry-Perot interferometer fabricated with a femtosecond laser," *Optics letters* **33**, 536–538 (2008).
- [68] J.-R. Zhao, X.-G. Huang, W.-X. He, and J.-H. Chen, "High-resolution and temperature-insensitive fiber optic refractive index sensor based on Fresnel reflection modulated by Fabry–Perot interference," *Journal of lightwave technology* **28**, 2799–2803(2010).
- [69] P. Morris, A. Hurrell, A. Shaw, E. Zhang, and P. Beard, "A Fabry–Perot fiber-optic ultrasonic hydrophone for the simultaneous measurement of temperature and acoustic pressure," *The Journal of the Acoustical Society of America* **125**, 3611–3622 (2009).
- [70] Y. Zhang, X. Chen, Y. Wang, K. L. Cooper, and A. Wang, "Microgap multicavity Fabry–Perot biosensor," *Journal of lightwave technology* **25**, 1797–1804 (2007).
- [71] V. R. Machavaram, R. A. Badcock, and G. F. Fernando, "Fabrication of intrinsic fibre Fabry–Perot sensors in silica fibres using hydrofluoric acid etching," *Sensors and Actuators A: Physical* **138**, 248–260 (2007).
- [72] H. Y. Choi, M. J. Kim, and B. H. Lee, "All-fiber Mach-Zehnder type interferometers formed in photonic crystal fiber," *Optics Express* **15**, 5711–5720 (2007).
- [73] L. Li, L. Xia, Z. Xie, and D. Liu, "All-fiber Mach-Zehnder interferometers for sensing applications," *Optics express* **20**, 11109–11120 (2012).
- [74] S. YIN, "Paul B. RUFFIN a Francis TS YU," *Fiber optic sensors*. 2nd ed. Boca Raton, FL: CRC Press, c2008, xiii (n.d.).
- [75] M. Z. Interferometer, Q. Rong, X. Qiao, R. Wang, H. Sun, M. Hu, and Z. Feng, "High-Sensitive Fiber-Optic Refractometer Based on a Core-Diameter-Mismatch," **12**, 2501–2505 (2012).

- [76] Q. Wang, L. Kong, Y. Dang, F. Xia, Y. Zhang, Y. Zhao, H. Hu, and J. Li, "High sensitivity refractive index sensor based on splicing points tapered SMF-PCF-SMF structure Mach-Zehnder mode interferometer," *Sensors and Actuators B: Chemical* **225**, 213–220(2016).
- [77] T. A. Birks and Y. W. Li, "The shape of fiber tapers," *Journal of Lightwave Technology* **10**, 432–438 (1992).
- [78] C. R. Liao, Y. Wang, D. N. Wang, and M. W. Yang, "Fiber in-line Mach-Zehnder interferometer embedded in FBG for simultaneous refractive index and temperature measurement," *IEEE Photonics Technology Letters* **22**, 1686–1688 (2010).
- [79] E. Huerta-Mascotte, J. M. Sierra-Hernandez, R. I. Mata-Chavez, D. Jauregui-Vazquez, A. Castillo-Guzman, J. M. Estudillo-Ayala, A.D. Guzman-Chavez, and R. Rojas-Laguna, "A core-offset Mach Zehnder interferometer based on a non-zero dispersion-shifted fiber and its torsion sensing application," *Sensors* **16**, 856 (2016).
- [80] X. Zhang and W. Peng, "Bent-fiber intermodal interference based dual-channel fiber optic refractometer," *Optics express* **23**, 7602–7610 (2015).
- [81] H. Luo, X. Li, W. Zou, W. Jiang, and J. Chen, "Modal interferometer based on a C-shaped ultrathin fiber taper for highsensitivity refractive index measurement," *Applied Physics Express* **5**, 12502 (2011).
- [82] Y.-L. Fang, C.-T. Wang, and C.-C. Chiang, "A small U-shaped bending-induced interference optical fiber sensor for the measurement of glucose solutions," *Sensors* **16**, 1460 (2016).
- [83] R. Yang, Y.-S. Yu, Y. Xue, C. Chen, Q.-D. Chen, and H.-B. Sun, "Single S-tapered fiber Mach-Zehnder interferometers," *Optics letters* **36**, 4482–4484 (2011).
- [84] K. Tian, G. Farrell, W. Yang, X. Wang, E. Lewis, and P. Wang, "Simultaneous Measurement of Displacement and Temperature Based on a

Balloon-Shaped Bent SMF Structure Incorporating an LPG," *Journal of Lightwave Technology* **36**, 4960–4966 (2018).

[85] Y. Zheng, L. H. Chen, X. Dong, J. Yang, H. Y. Long, P. L. So, and C. C. Chan, "Miniature pH optical fiber sensor based on Fabry– Perot interferometer," *IEEE Journal of Selected Topics In Quantum Electronics* **22**, 331–335 (2015).

[86] Q. Wang and W.-M. Zhao, "A comprehensive review of lossy mode resonance-based fiber optic sensors," *Optics and Lasers in Engineering* **100**, 47–60 (2018).

[87] M. Hernaez, C. R. Zamarreno, I. Del Villar, I. R. Matias, and F. J. Arregui, "Lossy mode resonances supported by TiO<sub>2</sub>-coated optical fibers," *Procedia Engineering* **5**, 1099–1102 (2010).

[88] C. R. Zamarreno, M. Hernaez, I. Del Villar, I. R. Matias, and F. J. Arregui, "Optical fiber pH sensor based on lossy-mode resonances by means of thin polymeric coatings," *Sensors and Actuators B:Chemical* **155**, 290–297 (2011).

[89] Q. Liu, Z. Ma, Q. Wu, and W. Wang, "The biochemical sensor based on liquid-core photonic crystal fiber filled with gold, silver and aluminum," *Optics & Laser Technology* **130**, 106363 (2020).

[90] M. Śmietana, M. Dudek, M. Koba, and B. Michalak, "Influence of diamond-like carbon overlay properties on refractive index sensitivity of nano-coated optical fibres," *physica status solidi (a)* **210**, 2100–2105 (2013).

[91] A. Priyadarshi, L. Shimin, S. G. Mhaisalkar, R. Rajoo, E. H. Wong, V. Kripesh, and E. B. Namdas, "Characterization of optical properties of acrylate based adhesives exposed to different temperature conditions," *Journal of Applied Polymer Science* **98**, 950–956 (2005).

[92] A. P. Drin', V. V Efanova, and N. I. Shut, "Thermal conductivity and kinetics of polymerization of an acrylate polymer coating," *Journal of Engineering Physics and Thermophysics* **66**, 164–171 (1994).

- [93] A. R. Mickelson, N. R. Basavanahally, and Y.-C. Lee, *Optoelectronic Packaging* (Wiley, 1997).
- [94] J.-M. Cariou, J. Dugas, L. Martin, and P. Michel, "Refractive-index variations with temperature of PMMA and polycarbonate," *Applied optics* **25**, 334–336 (1986).
- [95] M. Rashad, "Tuning optical properties of polyvinyl alcohol doped with different metal oxide nanoparticles," *Optical Materials* **105**, 109857 (2020).
- [96] M. Abdel-Ati, O. Hemedat, M. Mosaad, and D. Hemedat, "Thermal properties of pure and doped (polyvinyl-alcohol) PVA," *Journal of Thermal Analysis and Calorimetry* **42**, 1113–1122 (1994).
- [97] Y. Wu, K. Ye, Z. Liu, M. Wang, K. W. A. Chee, C.-T. Lin, N. Jiang, and J. Yu, "Effective thermal transport highway construction within dielectric polymer composites via a vacuum-assisted infiltration method," *Journal of Materials Chemistry C* **6**, 6494–6501 (2018).
- [98] S. Tripathi, G. K. Mehrotra, and P. K. Dutta, "Physicochemical and bioactivity of cross-linked chitosan–PVA film for food packaging applications," *International journal of biological macromolecules* **45**, 372–376 (2009).
- [99] C. Jianrong, M. Yuqing, H. Nongyue, W. Xiaohua, and L. Sijiao, "Nanotechnology and biosensors," *Biotechnology advances* **22**, 505–518 (2004).
- [100] J. Shi, Y. Zhu, X. Zhang, W. R. G. Baeyens, and A. M. García- Campana, "Recent developments in nanomaterial optical sensors," *TrAC Trends in Analytical Chemistry* **23**, 351–360 (2004).
- [101] A. Rothschild and Y. Komem, "The effect of grain size on the sensitivity of nanocrystalline metal-oxide gas sensors," *Journal of Applied Physics* **95**, 6374–6380 (2004).
- [102] S. K. Al-Hayali and A. H. Al-Janabi, "Effect of grapheme nanoparticle coating on the detection performance of cladding etched no-core fiber

interferometer sensor for relative humidity measurement," *Optical Fiber Technology* **55**, 102154 (2020).

[103] C. Elosua, F. J. Arregui, I. Del Villar, C. Ruiz-Zamarreno, J. M. Corres, C. Bariain, J. Goicoechea, M. Hernaez, P. J. Rivero, and A. B. Socorro, "Micro and nanostructured materials for the development of optical fibre sensors," *Sensors* **17**, 2312 (2017).

[104] M. E. Martinez-Hernandez, J. Goicoechea, and F. J. Arregui, "Hg<sup>2+</sup> Optical Fiber Sensor Based on LSPR Generated by Gold Nanoparticles Embedded in LBL Nano-Assembled Coatings," *Sensors* **19**, 4906 (2019).

[105] C. B. Collins, R. S. McCoy, B. J. Ackerson, G. J. Collins, and C. J. Ackerson, "Radiofrequency heating pathways for gold nanoparticles," *Nanoscale* **6**, 8459–8472 (2014).

[106] Z. Kang, X. Guo, Z. Jia, Y. Xu, L. Liu, D. Zhao, G. Qin, and W. Qin, "Gold nanorods as saturable absorbers for all-fiber passively Q-switched erbium-doped fiber laser," *Optical Materials Express* **3**, 1986–1991 (2013).

[107] N. Shalkevich, W. Escher, T. Burgi, B. Michel, L. Si-Ahmed, and D. Poulidakos, "On the Thermal Conductivity of Gold Nanoparticle Colloids," *Langmuir* **26**, 663–670 (2010).

[108] H. Jeon and K. Lee, "Effect of gold nanoparticle morphology on thermal properties of polyimide nanocomposite films," *Colloids and Surfaces A: Physicochemical and Engineering Aspects* **579**, 123651 (2019).

[109] D. Lopez-Torres, C. Elosua, J. Villatoro, J. Zubia, M. Rothhardt, K. Schuster, and F. J. Arregui, "Enhancing sensitivity of photonic crystal fiber interferometric humidity sensor by the thickness of SnO<sub>2</sub> thin films," *Sensors and Actuators B: Chemical* **251**, 1059–1067 (2017).

- [110] J. Mathew, Y. Semenova, and G. Farrell, "Effect of coating thickness on the sensitivity of a humidity sensor based on an Agarose coated photonic crystal fiber interferometer," *Optics express* **21**, 6313–6320 (2013).
- [111] Y. Zhang, H. Peng, X. Qian, Y. Zhang, G. An, and Y. Zhao, "Recent advancements in optical fiber hydrogen sensors," *Sensors and Actuators B: Chemical* **244**, 393–416 (2017).
- [112] N. A. M. Yahya, M. R. Y. Hamid, S. A. Ibrahim, B. H. Ong, N. A. Rahman, A. R. M. Zain, M. A. Mahdi, and M. H. Yaacob, "H<sub>2</sub> sensor based on tapered optical fiber coated with MnO<sub>2</sub> nanostructures," *Sensors and Actuators B: Chemical* **246**, 421–427(2017).
- [113] H. A. Al-Rubaiyee, S. K. Al-Hayali, and A. H. Al-Janabi, "Nanostructured coating of graphene nanoparticles deposited onto a cladding etched no-core optical fiber for temperature measurement," *Applied Optics* **59**, 4663–4671 (2020).
- [114] G. M. Veith, A. R. Lupini, S. Rashkeev, S. J. Pennycook, D. R. Mullins, V. Schwartz, C. A. Bridges, and N. J. Dudney, "Thermal stability and catalytic activity of gold nanoparticles supported on silica," *Journal of Catalysis* **262**, 92–101 (2009).
- [115] A. Zumla, D. S. Hui, E. I. Azhar, Z. A. Memish, and M. Maeurer, "Reducing mortality from 2019-nCoV: host-directed therapies should be an option," *The Lancet* **395**, e35–e36 (2020).
- [116] J. T. Wu, K. Leung, and G. M. Leung, "Nowcasting and forecasting the potential domestic and international spread of the 2019-nCoV outbreak originating in Wuhan, China: a modelling study," *The Lancet* **395**, 689–697 (2020).
- [117] W. Wang, J. Tang, and F. Wei, "Updated understanding of the outbreak of 2019 novel coronavirus (2019-nCoV) in Wuhan, China," *Journal of medical virology* (2020).

- [118] D. Wang, B. Hu, C. Hu, F. Zhu, X. Liu, J. Zhang, B. Wang, H. Xiang, Z. Cheng, and Y. Xiong, "Clinical characteristics of 138 hospitalized patients with 2019 novel coronavirus–infected pneumonia in Wuhan, China," *Jama* (2020).
- [119] I. Devrim, A. Kara, M. Ceyhan, H. Tezer, A. K. Uludag, A. B. Cengiz, I. Yigitkanl, and G. Secmeer, "Measurement accuracy of fever by tympanic and axillary thermometry," *Pediatric emergency care* **23**, 16–19 (2007).
- [120] C. B. Mogensen, L. Wittenhoff, G. Fruerhoj, and S. Hansen, "Forehead or ear temperature measurement cannot replace rectal measurements, except for screening purposes," *BMC pediatrics* **18**, 15 (2018).
- [121] G. Chen, J. Xie, G. Dai, P. Zheng, X. Hu, H. Lu, L. Xu, X. Chen, and X. Chen, "Validity of Wrist and Forehead Temperature in Temperature Screening in the General Population During the Outbreak of 2019 Novel Coronavirus: a prospective real-world study," *medRxiv* (2020).
- [122] M. Ahmed, C. L. Brace, F. T. Lee Jr, and S. N. Goldberg, "Principles of and advances in percutaneous ablation," *Radiology* **258**, 351–369 (2011).
- [123] K. Onsen, N. P. Johns, T. Khuayjarearnpanishk, S. Subongkot, A. Priprem, C. Hurst, and J. Johns, "Beneficial effects of adjuvant melatonin in minimizing oral mucositis complications in head and neck cancer patients receiving concurrent chemoradiation," *The Journal of Alternative and Complementary Medicine* **23**, 957–963 (2017).
- [124] J. S. Young and J. W. Simmons, "Chemotherapeutic Medications and Their Emergent Complications," *Emergency Medicine Clinics of North America* **32**, 563–578 (2014).
- [125] Y. Tang, R. C. C. Flesch, and T. Jin, "Numerical investigation of temperature field in magnetic hyperthermia considering mass transfer and diffusion in interstitial tissue," *Journal of Physics D: Applied Physics* **51**, 35401 (2017).

- [126] M. Lepetit-Coiffe, H. Laumonier, O. Seror, B. Quesson, M.-B. Sesay, C. T. W. Moonen, N. Grenier, and H. Trillaud, "Real-time monitoring of radiofrequency ablation of liver tumors using thermal-dose calculation by MR temperature imaging: initial results in nine patients, including follow-up," *European radiology* **20**, 193–201 (2010).
- [127] N. Grenier and H. Trillaud, "Real-time monitoring of radiofrequency ablation of liver tumors using thermal-dose calculation by MR temperature imaging: initial results in nine patients, including follow-up," (2009).
- [128] Y. Zhao, M. Chen, F. Xia, and R. Lv, "Small in-fiber Fabry-Perot low-frequency acoustic pressure sensor with PDMS diaphragm embedded in hollow-core fiber," *Sensors and Actuators A: Physical* **270**, 162–169 (2018).
- [129] Y. YU, D. LI, and L. ZHANG, "Experimental study on the characteristics of fiber Bragg grating temperature sensor packaged with metal tube [J]," *Journal of Natural Science of Heilongjiang University* **5**, (2011).
- [130] Y. Wu, F. Meng, H. Li, G. Yan, and L. Zhu, "Simultaneous measurement of micro-displacement and temperature based on balloon-like interferometer and fiber Bragg grating," *Optik* **183**, 875–880 (2019).
- [131] H. Rumiana, S. Maimanah, K. E. Kurniansyah, I. Yulianti, and N. M. D. Putra, "Fabrication and characterization of Polymer Optical Fiber (POF) based on Mach-Zehnder interferometer for temperature sensor," in *Journal of Physics: Conference Series* (IOP Publishing, 2019), Vol. 1321, p. 22005.
- [132] Q. Wu, Y. Semenova, A. M. Hatta, P. Wang, and G. Farrell, "Bent SMS fibre structure for temperature measurement," *Electronics letters* **46**, 1129–1130 (2010).
- [133] Y. Chen, Q. Han, T. Liu, F. Liu, and Y. Yao, "Simultaneous measurement of refractive index and temperature using a cascaded FBG/droplet-like fiber structure," *IEEE Sensors Journal* **15**, 6432–6436 (2015).

# *Appendices*

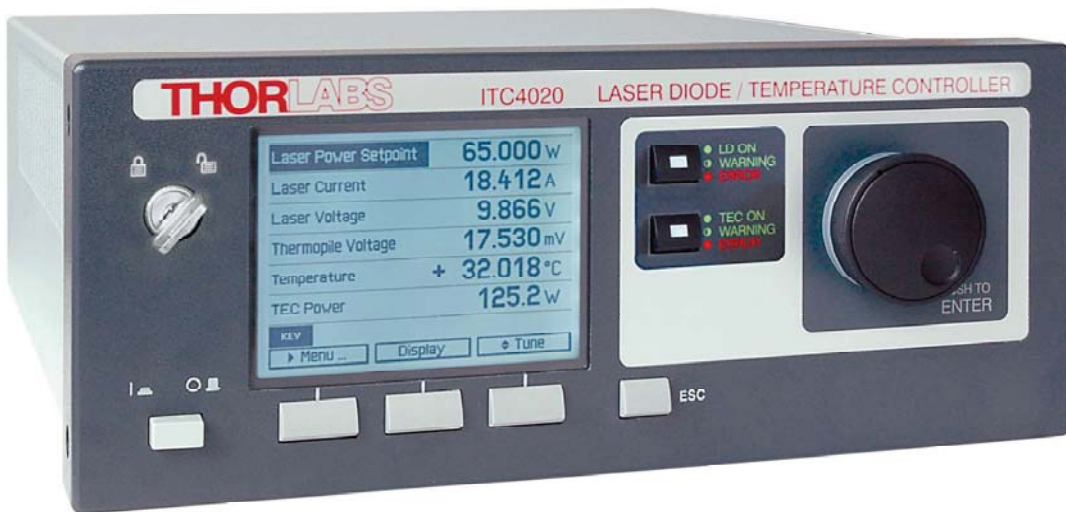
# Appendix

(A)



## Laser Diode Current and Temperature Controller

# ITC4000 Series Operation Manual



2018

---

# 1 General Information

The ITC4000 Series is a high power precision laser diode and temperature controller series with a USB 2.0 interface for driving laser diodes up to 20A laser current.

Special highlights of the ITC4000 Series Laser Diode and Temperature Controllers are:

- Operate with anode- or cathode-grounded lasers and photodiodes
- Current (photodiode) and voltage (thermopile) feedback inputs
- The laser diodes can be operated in constant current as well as in constant power mode
- CW mode with modulation up to 100kHz
- Internal DDS generator for sine, square, triangle waveforms
- External modulation input
- QCW mode with pulse width down to 100 $\mu$ s
- QCW trigger input and trigger output
- Interlock for automatic switch off by an external emergency switch or by a cable interruption
- Laser Diode Enable input
- High power TEC with excellent temperature stability and PID Auto-Tune function
- Temperature loop monitoring for laser protection
- A wide variety of protection features safeguard the laser diode and the TEC element from damage.
- USB interface for remote operation supporting the USBTMC protocol
- SCPI compliant command set
- VXI/np Instrument Drivers for various programming environments including NI-LabVIEW™, NI-LabWindows™/CVI and MS-Visual Studio
- Power efficient by active power management

This part of the operation manual contains specific information on how to operate the ITC4000 Series Laser Diode and Temperature Controller. A general description is followed by an explanation of how to operate the unit manually. The instrument provides a USB 2.0 Full Speed interface according to the USB 2.0 specification, the USBTMC specification and the USBTMC USB488 specification.

Related documents:

- LDC4000 Series Operation Manual available at [www.thorlabs.com](http://www.thorlabs.com)
- TED4000 Series Operation Manual available at [www.thorlabs.com](http://www.thorlabs.com)
- Series 4000 Programmers Reference Manual at [www.thorlabs.com](http://www.thorlabs.com)

# **Appendix**

**(B)**



# LM14S2 Butterfly Laser Diode Mount

## User Guide



For current pricing, please see our website.

▼ CHAPTERS

- Coherent Sources
- Incoherent Sources
- Quantum Electronics

Drivers/Mounts

Accessories

▼ SECTIONS

- Laser Diode Controllers
- Temperature/TEC Controllers
- LD/TEC Controllers
- LD/TEC Platforms

LD Mounts

- LED Drivers
- LED Mounts

## Universal Butterfly Mount



LM14S2

The LM14S2 Butterfly Mount is designed to operate all lasers and two-port electro-optic devices in a 14-pin butterfly package. The top surface includes heat sink fins and a recessed region to mount the laser diode, resulting in a very low-profile package. The LM14S2 includes a laser diode TEC lockout feature, which disables the laser when the TEC controller is not active.† This mount is designed to allow up to 5 A of laser current and 5 A of TEC current. It also provides a

Zero Insertion Force (ZIF) Socket, a remote interlock connection, and an LED to indicate when the laser diode is enabled.

This package comes with two adapter cards, each plugging into the connector at the bottom of the mount (see section below for details). A Bias-T Adapter is also included with the product, allowing for RF modulation of butterfly lasers specifically designed with this capability. The LM14S2 is pin-for-pin compatible with all Thorlabs' Benchtop Laser Diode Controllers (see pages 1436 - 1439), eliminating the need for custom-made interface cables.

† TEC lockout, which is easily bypassed if not required, only functions with Thorlabs' lasers and TEC controllers (see pages 1436 - 1480). The TEC controller requires that the laser package has an integrated TEC and thermal sensor.

PARAMETER	VALUE
Maximum Laser Current	5 A
Polarity of Laser Diode	AG
Polarity of Monitor Diode	Floating
Maximum TEC Current	5 A
Temperature Sensor	Thermistor
Temperature Range*	0 to 70 °C
Temperature Coefficient of Heat Sink	3 °C/W
Dimensions	3.5" x 3.5" x 1.25" 88.7 mm x 88.9 mm x 31.8 mm

\*At 25 °C with 2 A TEC current, integrated into laser package. Laser Diode dependent.



LM14S2  
Shown with a Two Port  
Electro-Optic Device

### Adapter Cards for Custom PIN Configuration

The LM14S2 eliminates the restriction of fixed pin configurations by using swappable configuration cards that plug into a connector located on the bottom of the mount. Two cards are included with the LM14S2. One card is pre-configured for both Type 1 and Type 2 lasers. The second card is a user-configurable card (LM14S2-UA) designed to allow custom wiring of the mount.

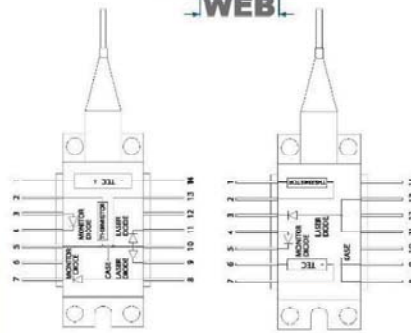


LM14S2  
Universal  
Adapter  
Card

### Features

- Compatible with all Commercially Available Laser Modules and Two-Port Electro-Optic Devices in 14-Pin Butterfly Packages
- Zero Insertion Force (ZIF) Sockets
- Compatible with Thorlabs' Laser Diode and TEC Controllers (See Pages 1436 - 1480)
- Compact, Low-Profile Design
- TEC Lockout Protection Circuit

Mechanical  
Drawings Available on the  
WEB



Type 1  
Pump Laser Diode\*

Type 2  
Telecom Laser Diode\*

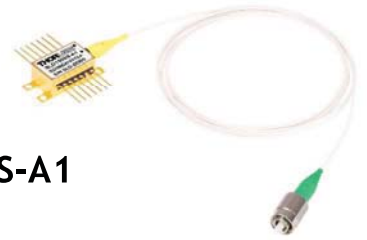
\*View shows alternate locations for monitor and laser diodes

PIN #	CONNECTOR (TYPE 1)	CONNECTOR (TYPE 2)
1	TEC Anode	Thermistor Ground
2	Thermistor	Thermistor
3	PD Anode	LD Cathode (DC)
4	PD Cathode	PD Anode
5	Thermistor Ground	PD Cathode
6	N.C.	TEC Anode
7	PD Cathode	TEC Cathode
8	PD Anode	LD Anode, Ground
9	LD Cathode	LD Anode, Ground
10	LD Anode, Ground	N.C.
11	LD Cathode	LD Anode, Ground
12	N.C.	LD Cathode (RF)
13	LD Anode, Ground	LD Anode, Ground
14	TEC Cathode	N.C.

ITEM #	\$	£	€	RMB	DESCRIPTION
LM14S2	\$ 324.00	£ 233.28	€ 281.88	¥ 2,582.28	Universal 14-Pin Butterfly Laser Diode Mount
LM14S2-UA	\$ 29.00	£ 20.88	€ 25.23	¥ 231.13	LM14S2 Universal Adapter Card for Custom Pin Configuration

# Appendix

(C)



### SLD1550S-A1

### Description

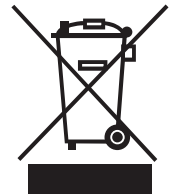
The SLD1550S-A1 is a 1550 nm, low-power, broadband Superluminescent Diode (SLD) with a near-Gaussian spectral profile and low ripple. This SLD is housed in a standard 14-pin butterfly package with FC/APC-connectorized, nonpolarization-maintaining fiber. An integrated thermistor allows for temperature control, thus stabilizing the power and spectrum.

### Specifications

CW;  $T_{CHIP} = 25^{\circ}C$ ,  $T_{CASE} = 0$  to  $65^{\circ}C$

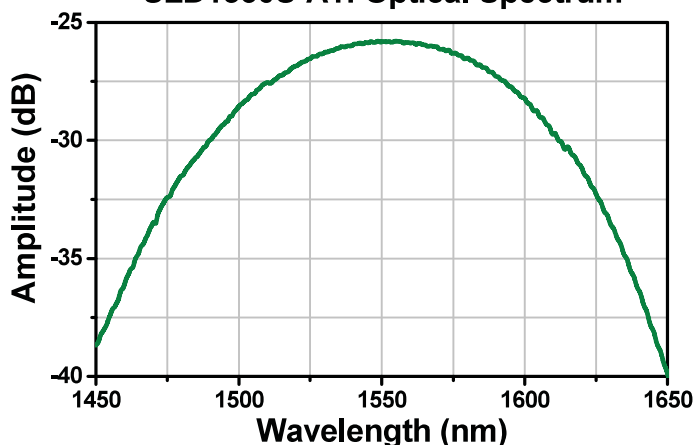
SLD1550S-A1				
	Symbol	Min	Typical	Max
Center Wavelength	$\lambda_C$	1520 nm	1550 nm	1580 nm
Operating Current	$I_{OP}$	-	450 mA	500 mA
ASE Power*	$P_{ASE}$	0.75 mW	1.0 mW	-
Optical 3 dB Bandwidth*	BW	100 nm	110 nm	-
RMS Gain Ripple *	$\delta G$	-	-	0.1 dB
Forward Voltage*	$V_F$	-	1.6 V	2.0 V
TEC Operation (Typical / Max @ $T_{CASE} = 25^{\circ}C / 65^{\circ}C$ )				
- TEC Current	$I_{TEC}$	-	0.35 A	1.5 A
- TEC Voltage	$V_{TEC}$	-	0.5 V	3.5 V
- Thermistor Resistance	$R_{TH}$	-	10 k $\Omega$	-

\*@ $I_{OP}$

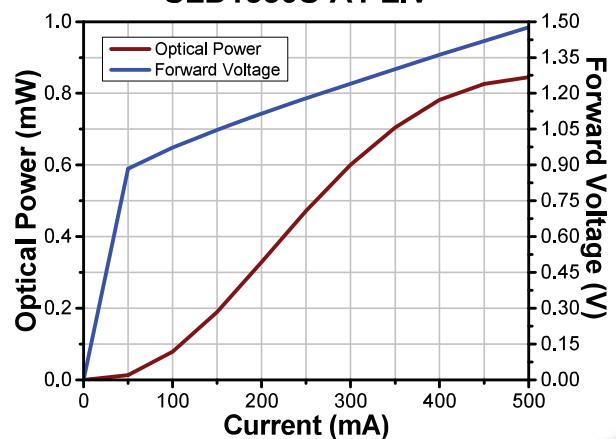


### Performance Plots

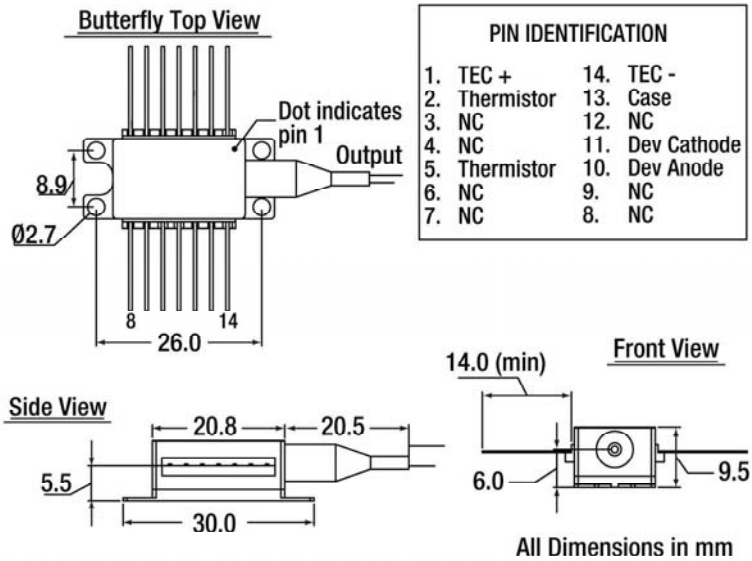
SLD1550S-A1: Optical Spectrum



SLD1550S-A1 LIV



## Drawings



**Note:** Output isolator and monitor photodiode are available options for butterfly-packaged diodes. Please contact Technical Support for more information.

# Appendix

**(D)**

# Corning® SMF-28® Ultra Optical Fiber

## Product Information



Corning® SMF-28® Ultra optical fiber is an ITU-T Recommendation G.652.D compliant optical fiber with Corning's enhanced low-loss and bend fiber technologies. This full-spectrum fiber has bend performance that exceeds the ITU-T Recommendation G.657.A1 standard and still splices the same as the installed base of standard single-mode fibers such as SMF-28e+ fiber. SMF-28 Ultra fiber offers industry-leading specifications for attenuation, macrobend loss, and polarization mode dispersion values, which provide a solid foundation for new network deployments as well as upgrades to existing networks. Since Corning brought the first fiber to market more than 40 years ago, Corning's leadership in single-mode fiber innovation has been unparalleled.

### Optical Specifications

#### Maximum Attenuation

Wavelength (nm)	Maximum Value* (dB/km)
1310	≤ 0.32
1383**	≤ 0.32
1490	≤ 0.21
1550	≤ 0.18
1625	≤ 0.20

\* Alternate attenuation offerings available upon request.

\*\* Attenuation values at this wavelength represent post-hydrogen aging performance.

#### Attenuation vs. Wavelength

Range (nm)	Ref. λ (nm)	Max. α Difference (dB/km)
1285 – 1330	1310	0.03
1525 – 1575	1550	0.02

The attenuation in a given wavelength range does not exceed the attenuation of the reference wavelength (λ) by more than the value α.

#### Macrobend Loss

Mandrel Radius (mm)	Number of Turns	Wavelength (nm)	Induced Attenuation* (dB)
10	1	1550	≤ 0.50
10	1	1625	≤ 1.5
15	10	1550	≤ 0.05
15	10	1625	≤ 0.30
25	100	1310, 1550, 1625	≤ 0.01

\*The induced attenuation due to fiber wrapped around a mandrel of a specified radius.

#### Point Discontinuity

Wavelength (nm)	Point Discontinuity (dB)
1310	≤ 0.05
1550	≤ 0.05

#### Cable Cutoff Wavelength (λ<sub>cc</sub>)

λ<sub>cc</sub> ≤ 1260 nm

#### Mode-Field Diameter

Wavelength (nm)	MFD (μm)
1310	9.2 ± 0.4
1550	10.4 ± 0.5

#### Dispersion

Wavelength (nm)	Dispersion Value [ps/(nm·km)]
1550	≤ 18.0
1625	≤ 22.0

Zero Dispersion Wavelength (λ<sub>0</sub>): 1304 nm < λ<sub>0</sub> < 1324 nm

Zero Dispersion Slope (S<sub>0</sub>): S<sub>0</sub> < 0.092 ps/(nm<sup>2</sup>·km)

#### Polarization Mode Dispersion (PMD)

	Value (ps/√km)
PMD Link Design Value	≤ 0.04*
Maximum Individual Fiber PMD	≤ 0.1

\*Complies with IEC 60794-3: 2001, Section 5.5, Method 1, (m = 20, Q = 0.01%), September 2001.

The PMD link design value is a term used to describe the PMD of concatenated lengths of fiber (also known as PMD<sub>0</sub>). This value represents a statistical upper limit for total link PMD. Individual PMD values may change when fiber is cabled.

#### How to Order

Contact your sales representative, or call the Optical Fiber Customer Service Department:  
 Ph: 1-607-248-2000 (U.S. and Canada)  
 +44-1244-525-320 (Europe)  
 Email: cofic@corning.com  
 Please specify the fiber type, attenuation, and quantity when ordering.



## Dimensional Specifications

Glass Geometry		Coating Geometry	
Fiber Curl	$\geq 4.0$ m radius of curvature	Coating Diameter	$242 \pm 5$ $\mu\text{m}$
Cladding Diameter	$125.0 \pm 0.7$ $\mu\text{m}$	Coating-Cladding Concentricity	$< 12$ $\mu\text{m}$
Core-Clad Concentricity	$\leq 0.5$ $\mu\text{m}$		
Cladding Non-Circularity	$\leq 0.7\%$		

## Environmental Specifications

Environmental Test	Test Condition	Induced Attenuation 1310 nm, 1550 nm, and 1625 nm (dB/km)
Temperature Dependence	$-60^{\circ}\text{C}$ to $+85^{\circ}\text{C}^*$	$\leq 0.05$
Temperature Humidity Cycling	$-10^{\circ}\text{C}$ to $+85^{\circ}\text{C}$ up to 98% RH	$\leq 0.05$
Water Immersion	$23^{\circ}\text{C} \pm 2^{\circ}\text{C}$	$\leq 0.05$
Heat Aging	$85^{\circ}\text{C} \pm 2^{\circ}\text{C}$	$\leq 0.05$
Damp Heat	$85^{\circ}\text{C}$ at 85% RH	$\leq 0.05$

\*Reference temperature =  $+23^{\circ}\text{C}$   
Operating Temperature Range:  $-60^{\circ}\text{C}$  to  $+85^{\circ}\text{C}$

## Mechanical Specifications

### Proof Test

The entire fiber length is subjected to a tensile stress  $\geq 100$  kpsi (0.69 GPa).\*

\*Higher proof test levels available.

### Length

Fiber lengths available up to 63.0 km/spool.

## Performance Characterizations

Characterized parameters are typical values.

Core Diameter	8.2 $\mu\text{m}$
Numerical Aperture	0.14 NA is measured at the one percent power level of a one-dimensional far-field scan at 1310 nm.
Effective Group Index of Refraction ( $N_{\text{eff}}$ )	1310 nm: 1.4676 1550 nm: 1.4682
Fatigue Resistance Parameter ( $N_d$ )	20
Coating Strip Force	Dry: 0.6 lbs. (3N) Wet, 14-day room temperature: 0.6 lbs. (3N)
Rayleigh Backscatter Coefficient (for 1 ns Pulse Width)	1310 nm: -77 dB 1550 nm: -82 dB



وزارة التعليم العالي والبحث العلمي

جامعة بغداد

معهد الليزر للدراسات العليا

# متحسس حراري يشبه البالون عالي الحساسية يعتمد على الألياف الأحادية

رسالة مقدمة الى

معهد الليزر للدراسات العليا / جامعة بغداد / لاستكمال متطلبات نيل شهادة ماجستير  
علوم في الليزر / الهندسة الالكترونية والاتصالات

من قبل

دنيا ابراهيم عبدالجبار الجنابي

بكالوريوس هندسة الليزر والالكترونيات البصرية - 2016

بإشراف

الأستاذ الدكتور عبد الهادي مطشر الجنابي

م 2020

هـ 1442

## الخلاصة

لقد أثبتت مستشعرات الألياف الضوئية (FOS) أنها طريقة رائعة ممتازة لمراقبة درجة الحرارة نظرًا لفوائدها العديدة ، مثل المناعة من التداخل الكهرومغناطيسي ، وخفة الوزن ، و صغر الحجم ، والمتانة ، وعرض النطاق الترددي العالي مما يسمح لعدد كبير من أجهزة الاستشعار بالعمل في نفس النظام . في هذا العمل ، تم اقتراح مستشعر درجة حرارة جديد قائم على مقياس التداخل Mach-Zehnder وعرضه تجريبيًا. يتكون هيكل الاستشعار عن طريق ثني ألياف أحادية النمط (SMF) في تكوين يشبه البالون. وتم فحص أداء المستشعر لدرجة الحرارة على ستة أقسام مختلفة من الألياف: الألياف مع طلاء بوليمر واقٍ أصلي ، وألياف مع طلاء بوليمر واقٍ منزوع ، وألياف مع طلاء كحول بولي فينيل (PVA) ، وألياف تعتمد على طلاء أغشية نانوية ذهبية (GNP) بسماكات مختلفة ( ~ 10، 20 ، و 30 نانومتر). و أظهر المستشعر المقترح المطلي بسلك طبقة 20 نانومتر من GNP أفضل أداء مع حساسية ممتازة ووقت صعود سريع ودقة ممتازة -2.56 نانومتر / درجة مئوية ، 1.73 مللي ثانية ، و  $1.82 \times 10^{-4}$  درجة مئوية ، على التوالي. بالاستفادة من مزاياها الممتازة المتمثلة في التكوين البسيط والتصنيع السهل والخصائص الحرارية الضوئية الجيدة والقوة الميكانيكية العالية ، يمكن أن يكون مستشعر درجة الحرارة عالي الحساسية هذا مرشحًا تنافسيًا لعمليات مراقبة درجات الحرارة المختلفة مثل جسم الإنسان والصناعات الغذائية والتحليل الكيميائي واكتشافات التحليل الجزيئي والطب الحيوي الخالي من الملصقات. على حد علمنا ، هذه هي المرة الأولى التي يتم فيها فحص تأثير ترسب GNP باستخدام تقنية (Sputtering) على SMF في تصنيع مستشعر درجة حرارة يعتمد على مقياس التداخل الكلي.